Alma Mater Studiorum · University of Bologna

DOTTORATO DI RICERCA IN FISICA
Ciclo XXXVI

Settore concorsuale: 02/A1 - Fisica sperimentale delle interazioni fondamentali
Settore scientifico disciplinare: FIS/01 - Fisica sperimentale

Nuclear Fragmentation Reaction Cross Sections for Hadrontherapy and Radioprotection: the FOOT Experiment

Presentata da: Roberto Zarrella

Coordinatore dottorato:
Prof. Alessandro Gabrielli

Supervisore:
Prof. Mauro Villa

Co-supervisori:
Dr. Matteo Franchini
Dr. Roberto Spighi

Esame finale anno 2024

"Ma 'n te rendi conto de quanto è bello?
Che non porti er peso der mondo su 'e spalle,
che sei soltanto un filo d'erba in un prato.
Nun te senti più leggero?"

Strappare lungo i bordi

Abstract

The characterization of nuclear fragmentation reactions of light nuclei ($A < 20$) in the energy range between 100 and 800 MeV/u is of great interest in current applied physics research. As a matter of fact, a complete understanding of such interactions would lead to an improvement in both Particle Therapy treatment planning and in risk-assessment for radiation exposure in long-term human Space missions. However, as of today, nuclear reaction databases lack the experimental measurements needed to accurately model the nuclear fragmentation. A phenomenological description of such processes is inherently subject to significant uncertainties, which could become too large for an acceptable evaluation of risks related to radiation exposure.
The aim of the FOOT experiment is to improve and expand the knowledge on nuclear fragmentation processes by performing a set of high accuracy cross section measurements. The experiment foresees an extensive program of data acquisition campaigns with light ion beams (^{4}He, ^{12}C and ^{16}O) at 200-800 MeV/u impinging on different targets with chemical composition representative of human tissues (mainly H, C and O). The final goal of FOOT is the measurement of double differential cross sections in kinetic energy and emission angle with a maximum uncertainty of 5% for projectile fragmentation and of 10% for target fragmentation reactions. To reach this objective, FOOT will employ two complementary setups capable of measuring the kinematic characteristics of both primary ions and secondary fragments: one made of an Emulsion Cloud Chamber and focused on light fragments ($Z \leq 3$) and one composed of electronic sub-detectors, optimized for heavier ions ($3 \leq Z \leq 8$).
In this Ph.D. thesis, the development and first implementation of particle tracking and full event reconstruction in the FOOT electronic setup is shown. Extensive studies on Monte Carlo simulated experimental setups have been carried out to accurately characterize the tracking performance of the setup in terms of efficiency and resolution for momentum and angular measurements. Moreover, the first full test of the reconstruction and analysis chain implemented in FOOT is described, showing the capabilities of the experiment for cross section evaluation.

Contents

List of Figures

Introduction

Particle Therapy is an external beam radiation therapy which employs beams of light ions (atomic number $Z \leq 8$) for the treatment of deep-seated solid tumors. The main advantage of this technique is given by the energy deposition of charged particles as they travel inside the human body. As a matter of fact, contrary to conventional photon beams, which undergo an exponential attenuation as they travel through matter, light charged nuclei show a low energy deposition in the entrance channel followed by a high energy release at a certain depth dependent on the beam energy, the Bragg Peak. This behavior makes them very suitable for delivering high dose to the tumor while sparing the surrounding healthy tissues, allowing also for the treatment of cancerous volumes near radiosensitive organs at risk. Moreover, light ions also show an enhanced biological effectiveness with respect to other radiological treatments and can thus be used for treating radioresistant tumors.

Nevertheless, a drawback of this method is that nuclear fragments created inside the patient by the beam give a contribution to the biological dose. As a matter of fact, target and projectile fragments increase the energy deposition outside the tumor, leading to a higher probability of radiation induced damage to healthy tissues. Furthermore, nuclear fragments affect the relative biological effectiveness along the beam path inside the patient, particularly in protontherapy, where target fragmentation reactions produce short path range nuclei. This means that during the definition of treatment plans for particle therapy, the production of nuclear fragments has to be carefully considered when evaluating the biological dose deposition and collateral radiation risk. However, the lack of cross section data for the related reactions in the literature makes it challenging to accurately estimate the contribution of fragmentation products at this time.

The characterization of nuclear fragmentation reactions is of strong interest also for Radiation Protection in Space. Astronauts are constantly exposed to a dose rate of radiation that is far higher than on Earth surface since they have no natural protection from cosmic radiation. Planning for long-term human space missions, such as a trip to Mars, requires careful consideration of this rise in environmental radiation. The main sources of space radiation are high energy protons and ^{4}He ions produced in Solar Particle Events and Galactic Cosmic Rays mainly ejected from supernovae. These particles have a broad energy spectrum, ranging redfrom MeV to over 10^{20} eV, with a peak between hundreds of MeV/u and GeV/u (kinetic energy per nucleon). The interactions of these particles have the potential to harm the crew and equipment either directly or through secondary fragments created inside the spaceship. In the last year, space agencies like NASA and ESA have been attempting to optimize the composition of spaceship hulls in order to block as much radiation from the environment as feasible. However, the reliability of Monte Carlo simulations as benchmarks for the development of novel shielding materials is strongly dependent on the availability of experimental cross section data for the fragmentation reactions involved, which are currently very scarce in literature.

To accurately characterize these fragmentation reactions, the FOOT (FragmentatiOn Of Target) experiment was proposed. The final goal of FOOT is to measure the double differential cross section of nuclear fragmentation reactions with respect to their emission angle and kinetic energy with a maximum 5% uncertainty in both direct and inverse kinematics. The physics program of the experiment foresees an extensive set of measurement campaigns using light ion beams, such as He, C and O, in the energy range of 100-800 MeV/u impinging on tissue-like and shielding material targets, like C, C_2H_4 or PMMA. To reach this goal, FOOT has been designed as a fixed target experiment with the ability to detect, track and identify both the primary beam and the nuclear fragments produced in beam-target interactions, while also measuring their kinematic properties. Since the needed ion beams will be available in different facilities, the experiment comprehends two portable and complementary setups: one based on nuclear emulsion films and mainly focused on light fragments ($Z \leq 3$), one made of several electronic detectors and optimized for heavier fragments ($3 \leq Z \leq 8$).

The aim of this work is to develop a solid and well-characterized analysis chain for the FOOT electronic setup. In particular, this Ph.D. project is focused on many aspect of event reconstruction, form online monitoring of real data to particle charge identification. The main focus is however on the development of the Global Reconstruction, which combines the information from several detectors of the setup with the aim to identify all particle trajectories in the FOOT magnetic spectrometer and evaluate their angle of emission and momentum. The Global Reconstruction is based on the GENFIT toolkit, which uses a Kalman Filter for track fitting, and implements a series of track finding algorithms with different pattern recognition approaches. The development, testing and accurate performance characterization of the Global Reconstruction is a fundamental step for the measurement of fragmentation cross sections.

To perform such task, the developed particle tracking algorithms have been tested on two Monte Carlo simulations reproducing the FOOT setup in different experimental conditions. In one of them, a partial setup without the magnetic field has been simulated, compatibly with data acquisitions performed before the completion of the setup. In the other one, the full FOOT setup has been simulated, with the aim of evaluating the Global Reconstruction performance for the next experimental campaigns. For both cases, many aspects of the Global Reconstruction have been explored, from track selection efficiency to the evaluation of angular and momentum resolution. Then, the developed tools have been used to perform a final closure test with the aim of reconstructing the simulated cross sections without using the Monte Carlo truth information.

In Chapter 1, an overview of the scientific motivations and underlying physics of nuclear fragmentations is presented, together with the impact of such reactions in Particle Therapy and Radiation protection in Space. In Chapter 2, the FOOT experiment is presented, with a detailed focus on the physics program and on the detector setup. Chapter 3 reports an overview of the FOOT reconstruction and analysis chain, with particular attention on the charge identification and Global Reconstruction steps. Chapter 4 is focused on the obtained track reconstruction performance and on the definition of a set of event selection cuts devoted to the improvement of such performance. Finally, in Chapter 5 the result of the final closure test focused on the reconstruction of Monte Carlo cross sections is shown, together with an overview on short and long-term perspectives and improvements. Further activities concerning the development of neutron detectors for the experiment are addressed in the appendix.

Chapter 1

Scientific motivations

The study of nuclear interactions of light nuclei in the intermediate energy range (100-800 MeV/u) has become increasingly more important in the last decades. This is the consequence of a shared interest in a better understanding of such interactions that comes from different research fields. Among these, two of the most important are *Particle Therapy (PT)* and *Radiation protection in Space (RS)*, where a complete knowledge of the underlying physics is fundamental to reduce as much as possible the radiation damage to people and equipment.

In this chapter, an overview of the physics of light nuclei in the energy range of interest is given. Then, the application of such physical principles to PT and RS is described, with a particular focus on the impact of nuclear interactions.

1.1 Charged particle interaction with matter

In the energy range of interest for PT and RS, the behavior of light ions traveling through matter can be accurately described by three main processes:

- Inelastic collisions with atomic electrons, which are the main source of energy loss and define the energy deposition profile and range of ions.
- Elastic coulomb scattering on material nuclei, which determines the lateral spread of primaries.
- Nuclear interactions with the nuclei of the medium, both elastic and inelastic.

The first two processes are determined by electromagnetic forces, while the rest is mediated by the strong nuclear interaction.

1.1.1 Electromagnetic energy loss

The main interactions leading to energy loss of hadrons in a medium are inelastic collisions with electrons. In these interactions, electrons usually receive enough energy to escape their orbitals, thus ionizing their atoms. These collisions occur very often along the path of the hadron, which continuously slows down inside the material. However, since the energy transfer and number of interactions are intrinsically stochastic, only an average value for the *stopping power* dE/dx can be defined. The mean energy lost through

electromagnetic collisions by a particle with charge Z inside an homogeneous material of density ρ_t is given by the Bethe-Bloch formula [1]

$$\left\langle \frac{\mathrm{d}E}{\mathrm{d}x} \right\rangle_{coll} = -K \frac{\rho_t Z_t}{A_t} \frac{Z^2}{\beta^2} \left[\frac{1}{2} \ln \left(\frac{2m_e c^2 \beta^2 \gamma^2 W_{max}}{I_t^2} \right) - \beta^2 - \frac{\delta}{2} - \frac{C}{Z} \right] \tag{1.1}$$

where

- m_e and c are the electron mass and the speed of light.
- β and γ are the Lorentz factors for the incident particle.
- K is a constant defined as $K = 4\pi r_e^2 N_A m_e c^2 = 0.307075$ MeV cm^2/g, where N_A and r_e are respectively Avogadro's number and the electron classical radius (2.8 fm) [2].
- Z_t, A_t and I_t are the atomic number, the mass number and the mean excitation potential of the absorber (target).
- W_{max} is the maximum energy that the primary con transfer to an electron of the material in a single collision, given by

$$W_{max} = \frac{2m_e c^2 \beta^2 \gamma^2}{1 + 2\gamma m_e / M + (m_e/M)^2} \tag{1.2}$$

  where M is the mass of the incident particle. If the energy of the incident particle is low, i.e. if $2\gamma m_e \ll M$, the expression becomes simply $W_{max} = 2m_e c^2 \beta^2 \gamma^2$. In the energy range of interest for our purposes, this condition is always verified.

- δ represents the density correction, which only becomes significant for very high energies of the incident particle.
- C represents the shell correction, relevant when the velocity of the incident particle is low enough to be comparable with the one of orbital electrons.

To limit the dependency on material properties, energy loss is usually also expressed in terms of *mass stopping power*, i.e. $\frac{\mathrm{d}E}{\mathrm{d}\chi} = \frac{1}{\rho}\frac{\mathrm{d}E}{\mathrm{d}x}$. The description of energy loss given in Equation 1.1 is accurate at the level of a few percent for ions with β much higher than that of atomic electrons, in particular in the energy range where $0.1 \leq \beta\gamma \leq 1000$. Some examples of Bethe-Bloch curves are shown in Figure 1.1. It can be noticed that all the curves show a minimum at a value of $\beta\gamma \simeq 3$ and grow at the sides. In the high energy range, the behavior is mainly dictated by the logarithmic term, which creates the so-called relativistic rise (up to a density effect plateau). At low incident particle energies, the energy loss becomes approximately proportional to $1/\beta^2$ up to the point where the shell correction becomes relevant, effectively lowering the value of the stopping power [2].

It is important to notice that Equation 1.1 provides an expression for the mean energy loss per unit length. Given the stochastic nature of the interactions, the energy lost by particles in a layer of material is not constant and the actual distribution depends on the thickness of the crossed medium. This latter parameter can be estimated through the quantity

$$\kappa = \frac{\bar{\Delta}}{W_{max}} \tag{1.3}$$

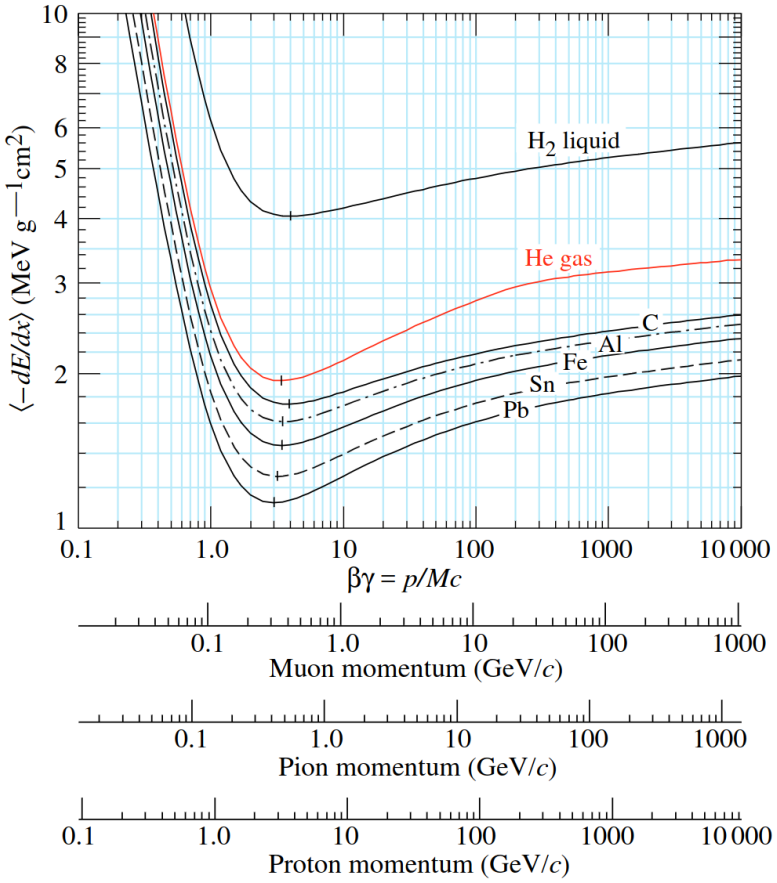

Figure 1.1: Mass stopping power ($\frac{dE}{d\chi}$) described by Bethe-Bloch curves for different particles (from top to bottom: μ, π and p) and media (from [2]).

where $\bar{\Delta}$ is the mean energy deposited in the absorber and W_{max} is given by Equation 1.2. The material is considered as thick if $\kappa \gg 1$ (or $\beta \ll 1$). In this case, the total energy loss is the outcome of many independent small releases and the resulting distribution can be modeled with a Gaussian. In all other cases, the total energy loss is determined by very few interactions and the shape of the distribution develops a long tail at higher values caused by hard collisions. The actual shape has been accurately modeled in the works of Landau [3] and Vavilov [4] in different energy ranges defined through the parameter κ. When $\kappa \leq 0.01$ (very thin absorber or $\beta \simeq 1$), the energy loss fluctuations can be approximated by a Landau distribution, while the asymmetric Vavilov curve is more accurate at intermediate values of κ [5, 6]. An example of the different energy loss distributions for some values of κ is given in Figure 1.2.

The fact that the energy loss of ions can be described with Equation 1.1, also leads to an important characteristic of such particles. While photons show an exponential attenuation along their path, charged particles can only travel a certain distance inside a medium, meaning that it is possible to define a value for the range R of an ion beam. The most common definition of this quantity is obtained using the *Continuous-Slowing-Down Approximation* (CSDA). The value of R_{CSDA} is defined as the range of a particle whose energy loss is equal to the stopping power given by the Bethe-Bloch equation, i.e.

$$R_{CSDA} = \int_0^L dx = \int_E^0 \left(\frac{\mathrm{d}E}{\mathrm{d}x}\right)^{-1} \mathrm{d}E \tag{1.4}$$

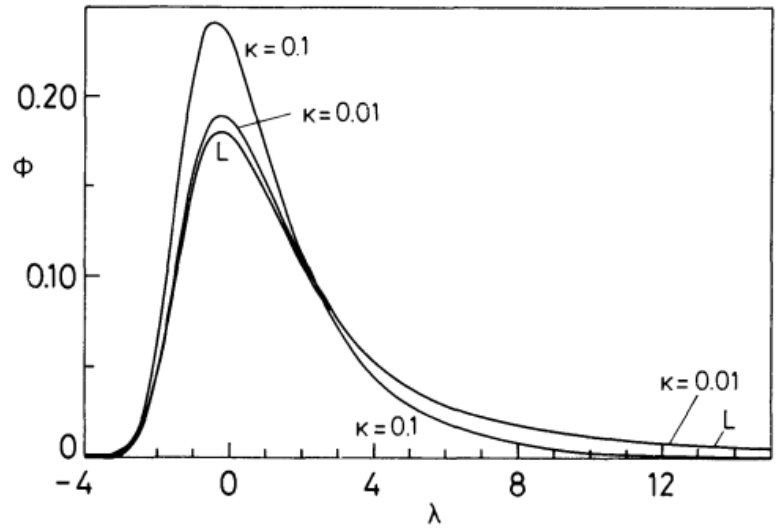

Figure 1.2: Landau-Vavilov distributions for energy loss at different values of the parameter κ (from [5]). The peaks of all distributions are fixed at 0 to better compare them. The quantities ϕ and λ are proportional to the probability density function and the energy loss, respectively.

where L is the maximum range of the particles and E their initial kinetic energy. The integration of Equation 1.4 leads to

$$R_{CSDA}(v) = \frac{M}{Z^2} F(v) \tag{1.5}$$

where $F(v)$ is a function of the initial speed v of the particle. [7]

The definition of Equation 1.4 also provides a series of useful scaling laws to extrapolate particle range in different conditions. For example, the ranges of a particle crossing two materials (with density ρ_1 and ρ_2) with the same speed are linked by the equation:

$$\frac{R_1}{R_2} = \frac{\rho_2}{\rho_1}\sqrt{\frac{A_1}{A_2}} = \frac{\rho_2}{\rho_1}\sqrt{\frac{M_1}{M_2}} \tag{1.6}$$

which shows how denser materials are more effective in stopping charged particles. At the same time, the ranges of two particles A and B entering into the same material with the same initial velocity will follow the formula:

$$\frac{R_A}{R_B} = \frac{A_A}{A_B}\frac{Z_B^2}{Z_A^2} = \frac{M_A}{M_B}\frac{Z_B^2}{Z_A^2} \tag{1.7}$$

This equation shows how different ions behave in a medium. For example, a proton beam has a range inside a material that is 3 times higher than that of a ^{12}C ion beam with the same kinetic energy per nucleon (i.e. the same β). [6]

1.1.2 Multiple Coulomb Scattering

While moving inside a medium, charged particles are also subject to elastic Coulomb interactions with the nuclei of the material. This electromagnetic collisions are the main responsible for the transverse spread of impinging particle beams. The resulting widening

of the beam is due to a cumulative effect of a series of deflections at small angles, usually referred to as Multiple Coulomb Scattering (MCS). The description of MCS has been reported in Molière's theory (1948), which describes the statistical distribution $F(\theta, x)$ of the scattering angle θ as a function of the penetration depth x of the particles inside the material. In the first order approximation, the function can be modeled as a Gaussian [8]

$$F(\theta, x) = \frac{1}{\pi\sigma_\theta} e^{-\left(\frac{\theta^2}{2\sigma_\theta^2}\right)} \tag{1.8}$$

where the standard deviation of the distribution, first obtained by Highland [9], can be extracted as

$$\sigma_\theta = \frac{13.6\text{MeV}}{pv} Z\sqrt{\frac{x}{X_0}}\left[1 + 0.0038\ln\left(\frac{x}{X_0}\right)\right] \tag{1.9}$$

where p, v and Z are the momentum, velocity and atomic number of the particle, respectively, while X_0 is the radiation length of the material

$$X_0 = \frac{A}{4\alpha N_a Z^2 r_e^2 \ln\left(183 Z^{-1/3}\right)} \tag{1.10}$$

where Z and A refer to the medium and α is the fine-structure constant.

An example of the lateral widening caused by MCS of some ion beams is shown in Figure 1.3. As it is clearly noticeable, the transverse spread of a beam with fixed velocity is considerably lower for heavier particles, in accordance with the description of Equation 1.9.

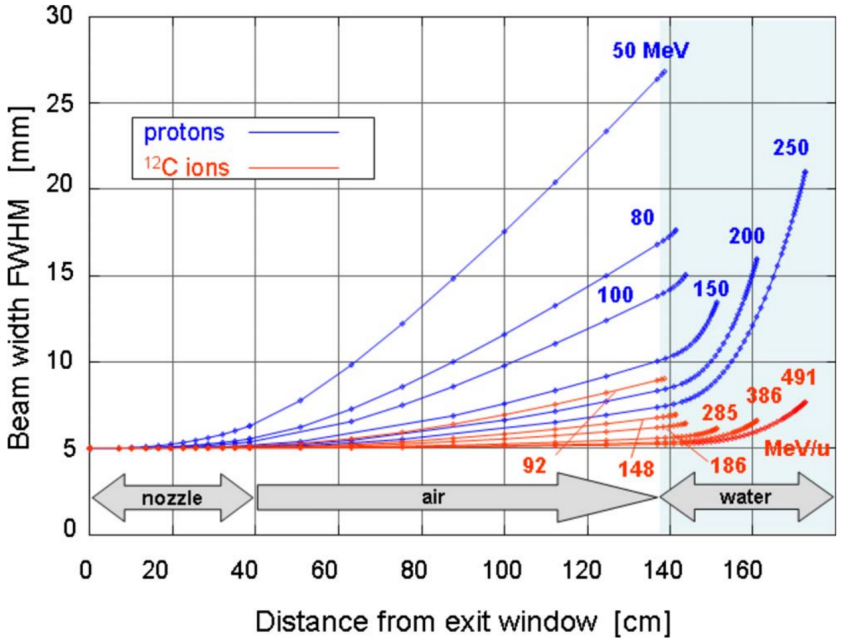

Figure 1.3: Lateral spread due to MCS for beams (protons and ^{12}C ions) at several energies in the GSI facility. Here, the different regions crossed by the beam are highlighted (from [10]).

It can be noticed that, since MCS is given by the interactions with the material nuclei, it is much less probable than the collisions with atomic electrons described in Section 1.1.1.

As a matter of fact, the interaction cross section is approximately proportional to the area of the target, i.e.

$$\frac{\sigma_{nucleus}}{\sigma_{atom}} \propto \frac{r^2_{nucleus}}{r^2_{atom}} \propto \frac{(10^{-14}\text{m})^2}{(10^{-10}\text{m})^2} \sim 10^{-8}$$

1.1.3 Nuclear interactions

While moving inside the medium, ions can also undergo nuclear interactions with the material nuclei. These collisions play a less significant role with respect to electromagnetic ionization in terms of energy loss of the incident particle, but they still need to be considered in beam transport calculations. Nuclear interactions can be both elastic or inelastic. On the one hand, elastic collisions do not lead to energy deposition in the material and only contribute to the total deflection of particle trajectory. These interactions lead to a further increase in the lateral spread of ion beams, with an higher number of particles contributing to the beam tails. [11]

On the other hand, inelastic collisions between projectile and medium nuclei are more violent and can lead to:

- Nuclear fragmentation, resulting in the emission of lighter particles as a consequence of the break-up of either or both projectile and target nuclei.
- Nuclear excitation, with the consequent emission of prompt γ rays ($\sim$0-10 MeV) during the relaxation of the nuclei.

The study of nuclear inelastic collisions has been the main subject of many theoretical and experimental works. [12, 13, 14] These interactions can be modeled as a multiple stage process. The first stage is usually referred to as the *dynamic stage* and has a time scale of about $10^{-23} - 10^{-22}$ s. This step includes all the interactions between projectile and target nucleons occurring inside the nuclear matter of the latter (Intra-Nuclear Cascade), with possible emission of nucleons or light fragments. The nuclear fragments emitted during this first step of the interaction have high energy and are mainly emitted in the direction of the incident particle. After the collision, both nuclei are left in a state of non-equilibrium and they go through a *pre-equilibrium stage*. In this phase, the nucleons interact with each other to re-distribute the excitation energy, with the possibility of ejecting additional particles. The following step of the process is the *slow stage*, with a characteristic time scale longer than 10^{-18} s, and it comprehends the de-excitation of all the residual products. Depending on their mass and energy, the final state nuclei can either emit low energy fragments through nuclear evaporation or fission. During the slow stage, nuclear fragments are emitted in an almost isotropic way and have lower energy than those emitted in earlier phases. The last step of the interaction is the return of residual nuclei to their fundamental state, mostly through the emission of γ rays (10^{-16} s). Figure 1.4 shows a simplified sketch of a nuclear interaction for both a proton or nucleus projectile. The main difference between the two situations is that in the first case only the target nuclei can fragment, while in the latter projectile fragmentation is also possible. [11]

An accurate modeling of the whole process is very complex, since it consists in multi-bodies interactions in both the electromagnetic and nuclear potential. For energies exceeding few tens of MeV/u, nuclear reactions are expected to be dominated by nucleon-nucleon collisions. One of the most successful microscopic descriptions of Nucleus-Nucleus collisions in these terms is given by the *Glauber model* [15], which expresses nuclear inelastic

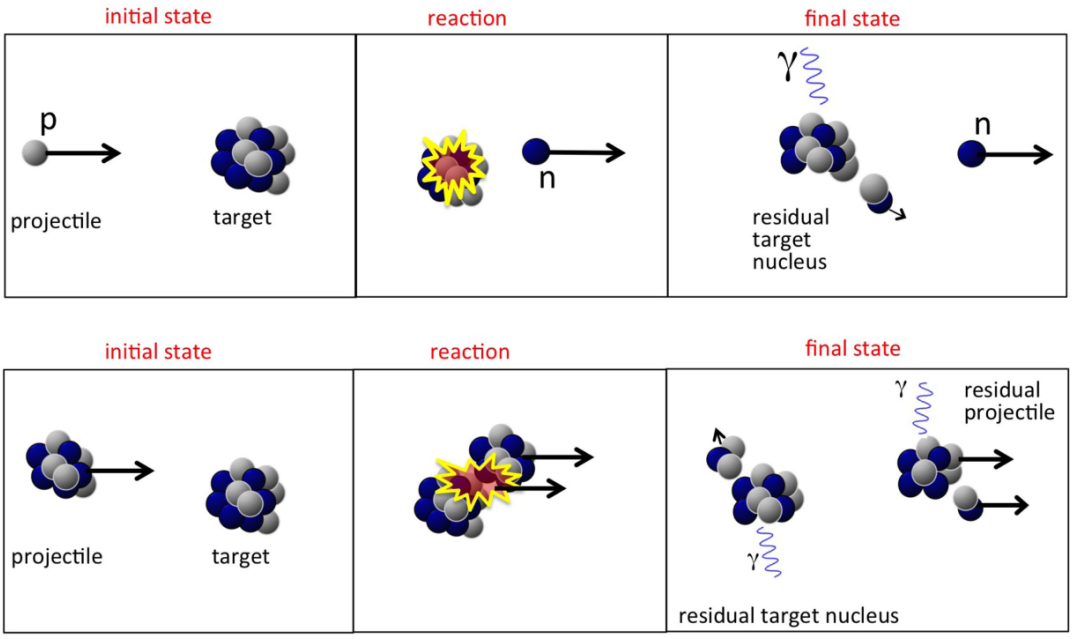

Figure 1.4: Sketch of a nuclear interaction for the case of a proton (top) or ion (bottom) projectile (from [11]).

reactions as the consequence of a series of individual nucleon-nucleon (N-N) collisions. In this framework, the nucleon-nucleon total cross section behavior as a function of projectile energy strongly determines the shape of the nucleus-nucleus (A-A) cross section. The description given by Glauber was first studied and validated for high energy collisions, for which the trajectory of the projectile can be considered straight. However, it has been shown that the model works well also at intermediate kinetic energies ($\sim$ 10-1000 MeV/u) with some necessary corrections that take into account the bending of the projectile path in the electromagnetic and nuclear potential. For example, in the implementation of the Glauber model at intermediate energies given in [16], the local mean free path $\Lambda(r)$ for a nucleon inside a nucleus is defined as

$$\Lambda(r) = \left[\rho(r)\sigma_T^{\overline{NN}} \right]^{-1} \tag{1.11}$$

where $\rho(r)$ is the nuclear matter density and $\sigma_T^{\overline{NN}}$ is the total N-N scattering cross section averaged over isospin (i.e. protons and neutrons). In the case of nucleus-nucleus collisions, Equation 1.11 can be extended by averaging the mean free path over all the nucleons in the projectile. Considering a nuclear matter density of $\rho_p(r)$ and $\rho_t(r)$ for projectile and nucleus, respectively, one can define the mean free path as

$$\Lambda(r) = \left[\sigma_T^{\overline{NN}} \int \mathrm{d}\Omega \int_V \rho_p(\vec{s})\rho_t(\vec{r}-\vec{s})\mathrm{d}\vec{s} \right]^{-1} \tag{1.12}$$

where V is the volume of nuclear overlap at a distance r, $\vec{s}$ is the position variable for integration over V and $\mathrm{d}\Omega$ is the angular component of $\vec{r}$.

Then, the mean free path can be used to calculate the transparency function $T(b)$, which represents the probability of not having a n-n interaction at a given impact parameter b

$$T(b) = \exp\left[\int_{-\infty}^{+\infty} -\frac{\mathrm{d}z}{\Lambda(r)} \right] \tag{1.13}$$

Here, z represents the distance between projectile and target along the beam axis, such that $r = \sqrt{b^2 + z^2}$. It can be noticed that the shape of the transparency function is only determined by the behavior of $\sigma_T^{\overline{NN}}$ as a function of energy and by the distribution of nuclear matter, i.e. the shape and size of the involved nuclei. An example of the behavior of the transparency function is given in Figure 1.5 for the ^{12}C + ^{12}C reaction. As it can be noticed, between 30 and 300 MeV/nucleon, the change in transparency is confined to a few fm band in the impact parameter on the surface of the reaction volume. This means that the total cross section is mainly determined by the behavior of peripheral collisions.

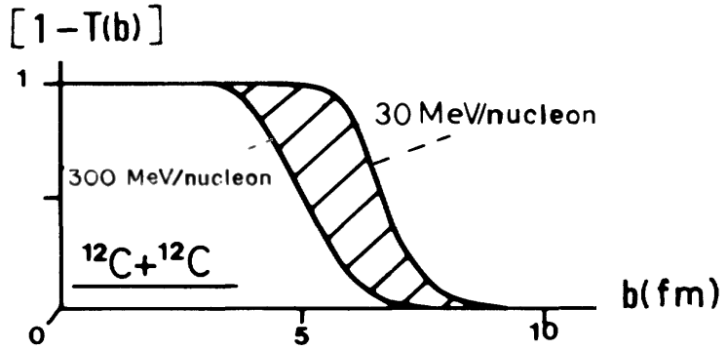

Figure 1.5: Behavior of the transparency function of the ^{12}C + ^{12}C reaction for two different energies of the projectile nucleus. The graph reports the complementary of $T(b)$, which represents the probability of having at least one nuclear interaction between projectile and target (from [16]).

The total reaction cross section can be then extracted from the transparency by integrating its complement to 1, i.e. the *absorption probability*, over the impact parameter

$$\sigma_R = \int_0^\infty 2\pi b \, [\, 1 - T(b) \,] \, \mathrm{d}b \tag{1.14}$$

The main assumption here is that any given n-n scattering leads to a nuclear reaction between the two colliding nuclei. For intermediate energies, Equation 1.14 needs to be corrected using an "effective" impact parameter, usually defined as the distance of closest approach of the projectile in the Coulomb and nuclear potential of the target. [17]

An example of the correlation between Nucleus-Nucleus total cross sections and nucleon-nucleon interactions is reported in Figure 1.6, which refers to the ^{12}C + ^{12}C reaction. It can be noticed that the dip in the interaction cross section in the 200-400 MeV/u region is strongly connected to the one observed for single nucleon-nucleon interactions. [16]

The energy released in the nucleon-nucleon collisions is transferred to the whole nucleus, eventually giving rise to break-up and fragmentation. The simple interpretation of complex nuclear processes as a series of nucleon-nucleon interactions has been proven to reproduce the experimental measurements with good accuracy. For this reason, Glauber-like models are employed in most of particle transport routines currently used in Monte Carlo (MC) simulation codes. These models usually also include further corrections that take into account quantum effects, such as Pauli exclusion principle and Fermi motion of nucleons inside target nuclei [19].

Many semi-empirical descriptions of nuclear reaction cross sections have been proposed. One of the most used is the Bradt-Peters formula [14]

$$\sigma_R = \pi r_0^2 \left(A_p^{1/3} + A_T^{1/3} - b \right)^2 \tag{1.15}$$

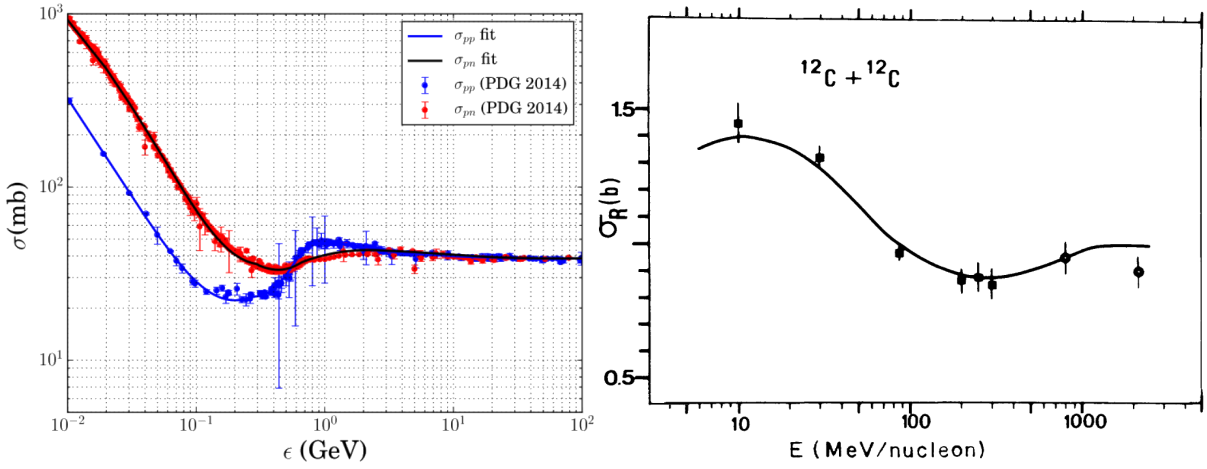

(a) (b)

Figure 1.6: (a) Nucleon-nucleon total reaction cross sections as a function of the kinetic energy of the projectile (from [18]). (b) Total nuclear reaction cross section of the ^{12}C + ^{12}C process as a function of the projectile kinetic energy. Here, the black dots represent experimental results while the continuous curve is the reaction cross section obtained from theoretical calculations of the Glauber model considering the electromagnetic and nuclear potential corrections (from [16]).

where $r_0 \simeq 1.2$ fm is the nucleon radius, b is an overlapping factor and A_p and A_T are the mass numbers of projectile and target nuclei. This expression has been shown to be accurate only for kinetic energies of the projectile above 1.5 GeV/u. Below such range, the reaction cross section starts depending on projectile energy. One of the parameterizations used to model nucleus-nucleus inelastic interactions (expressed in terms of total pp and pn cross sections) in the energy range from 30 MeV/u to 1 GeV/u is

$$\sigma_R = \pi C(E) \left(\sqrt{\sigma_{pp}^{tot} Z_1^{2/3} + \sigma_{pn}^{tot} N_1^{2/3}} + \sqrt{\sigma_{pp}^{tot} Z_2^{2/3} + \sigma_{pn}^{tot} N_2^{2/3}} \right)^2 \tag{1.16}$$

where N and Z are the neutron and proton number of the projectile and target of the interaction, respectively, and $C(E)$ is an energy-dependent coefficient which has to be determined from experimental data. An example of the results obtained with this model is shown in Figure 1.7, where Equation 1.16 is used to reproduce the nuclear reaction cross sections of proton and ^{12}C nuclei impinging on a carbon target [20].

While the reliability of such models has been established for what concerns total reaction cross sections (see Figure 1.6b), they do not give any information regarding differential cross sections in terms of angle of emission and kinetic energy of the fragments. As of today, no rigorous model for such calculations has been found and the description of fragment emission is based on phenomenological microscopic models. However, as shown in several studies like [21], [22] and [23], experimental values for differential cross sections are unfortunately poorly known. The most relevant differential cross section measurements for nuclear fragmentation have been performed at GANIL for ^{12}C beams of 50 MeV/u [24] and 95 MeV/u [25], i.e. for only one ion and two projectile energies. The scarcity of experimental values is especially marked for light nuclei ($A < 20$) in the energy range from 100 to 800 MeV/u [26]. This means that any phenomenological or semi-empirical description of the process can not be validated and is unavoidably affected by

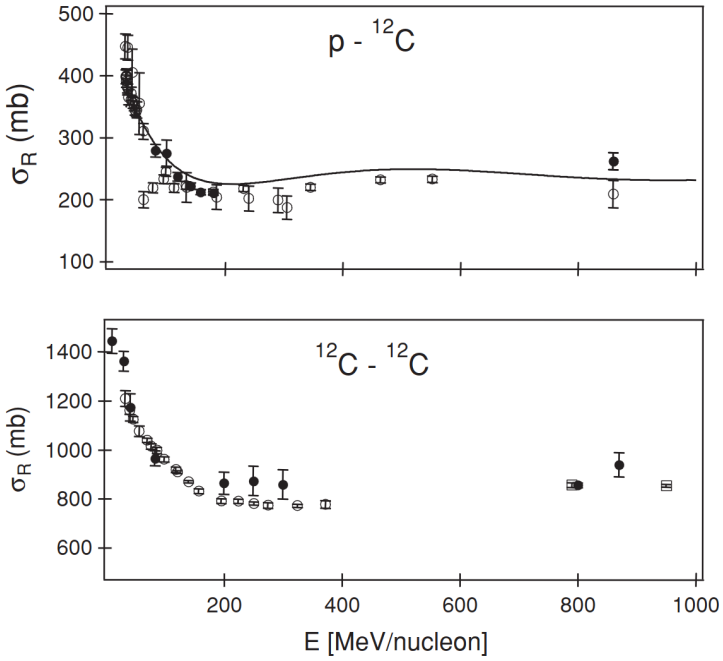

Figure 1.7: Comparison between experimental data and the semi-empirical model of Equation 1.16 for total nuclear reaction cross section of p and ^{12}C ions impinging on a carbon target as a function of the projectile kinetic energy (from [20]).

significant uncertainties. This lack of data in cross section databases becomes a relevant issue whenever an accurate modeling of the behavior of nuclear fragments is needed. In some research fields, such as Particle Therapy and Radiation Protection in Space, these uncertainties might become too large to produce acceptable results. In the next sections, the role of nuclear interactions in these two research fields is discussed, with a focus on the contribution of nuclear fragmentation reactions to radiation-induced health risks.

1.2 Particle Therapy

Cancer is a general term used to indicate a large group of diseases that consist in an uncontrolled proliferation of cells inside a tissue due to an unexplained genetic mutation. The abnormal growth of these dysfunctional cells may also lead to the death of the patient. According to the World Cancer Research Fund, in 2020 more than 18 million new cancer cases were diagnosed and almost 10 million deaths by tumor were registered in the same year. With these numbers increasing every year, the search for innovative and more precise treatments is one of the primary interests in clinical practice. [27]

One of the main treatment options in oncology is *Radiation therapy* or *Radiotherapy*, which uses ionizing radiation to damage cancerous tissues. This technique is usually performed in combination with either surgical or pharmacological treatments. The final goal of radiotherapy is to induce irreparable damage to the DNA strands inside tumor cells in order to remove their clonogenic capability, i.e. their ability to reproduce.

One of the main applications of light ion beams is *Particle Therapy (PT)*, a special form of radiation treatment that employs hadron beams (usually p and ^{12}C ions). The advantage of using hadrons instead of conventional X-rays comes from their finite range (see Section 1.2.1) and enhanced biological effectiveness (see Section 1.2.2), which makes

it possible to optimize the damage to cancerous cells while sparing healthy and functional tissues.

The type and energy of beams to be used in PT treatments is calculated via Treatment Planning Systems (TPS). These tools are required to be fast and efficient and are therefore largely based on analytical calculations, validated by comparison with Monte Carlo (MC) simulations and real measurements. The body of the patient is modeled through medical images obtained from Computed Tomography (CT) scans, allowing for an accurate identification of the cancer region and surrounding tissues. Then, TPS use these information to calculate the energy, direction, fluence and number of beams to employ in order to optimize the damage to the disease. [6]

PT is a consolidated technique in clinical practice and its effectiveness has been well-established since decades. There are currently more than 100 facilities in operation in the whole world, with many more under construction or expansion. The total number of patients treated by the end of 2021 was around 325000, mainly using protons (86%) and carbon ions (13%) [28].

1.2.1 Physical principles of Particle Therapy

The main advantage of PT with respect to conventional radiotherapy stems from the specific shape of the energy loss profile of ion beams. As shown in Figure 1.8, ion beams at typical therapeutic energies (200-400 MeV/u) show a peculiar behavior along their path. Their energy deposition is almost constant at the entrance channel and grow suddenly at a precise penetration depth, called the *Bragg peak*, where the particles stop. This sharp rise is a consequence of the $1/\beta^2$ factor in the Bethe-Bloch formula (Equation 1.1), which implies that the particle loses more energy as it slows down, until it reaches a complete stop.The depth of the Bragg peak is directly linked to particle range and thus to the beam energy (see Equations 1.4 and 1.5), as reported in Figure 1.8b. Figure 1.8a also shows the difference in the energy loss shape between a single particle and a beam. In the latter case, the Bragg peak is wider and lower (with respect to the entrance channel) because of the *energy straggling* coming from stochastic fluctuations in single particle interactions with the medium (as described in Equation 1.3). As a matter of fact, this variability leads to a widening of the energy distribution of particle beams along their path, even in the case of monochromatic ions. [1]

The physical advantage of cancer treatment with ion beams with respect to conventional X-rays can be better understood in terms of *absorbed dose D*, which is defined as the energy released in a material dE per unit of mass dm

$$D = \frac{\mathrm{d}E}{\mathrm{d}m} \tag{1.17}$$

Absorbed dose is measured in Gray, where 1 Gy = 1 J/1 kg. Dose is a fundamental quantity in radiotherapy because it can be linked to the amount of cells damaged by radiation exposure in each of the tissues hit by the treatment.

A comparison of the depth-dose profiles of different therapeutic particle beams in water is shown in Figure 1.9a. It can be easily noticed that the depth-dose profile for photons is completely different, with a sharp rise in the entrance channel and a long exponential fall-off at higher penetration depths. This curve is determined by the specific energy release of photons inside the patient, which is actually given by secondary electrons produced by the interactions of the beam with the patient tissues. The starting rising edge of the

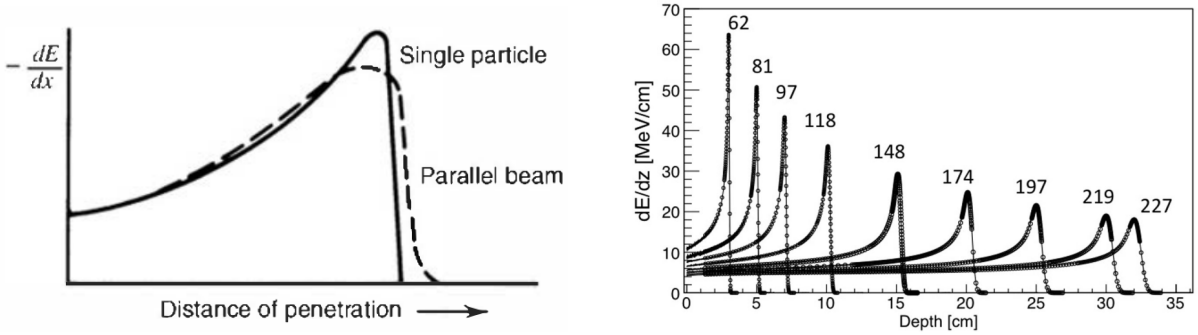

(a) (b)

Figure 1.8: (a) Example of the typical shape of energy loss of an ion beam as a function of the penetration depth inside matter. Both curves are normalized to the energy loss in the entrance channel. The example here shows the difference in the shape of the Bragg peak for a single ion and a beam (from [1]). (b) Bragg peak for proton beams of different initial kinetic energies (in MeV, from [29])

curve is caused by the build-up of secondaries, while the fall-off shape is determined by the exponential attenuation of the primary photons.

In both PT and radiotherapy, it is usually impossible to cover the whole volume of the disease with a single beam. In clinical practice, a uniform dose distribution on the tumor is required. With X-rays, this is achievable only using several primary beams at different energies and impinging on the patient from many angles. On the contrary, in PT it is possible to create a flat dose distribution, the so-called *Spread-Out Bragg Peak (SOBP)*, by tuning the energy and intensity of the beam. An example of this procedure is shown in Figure 1.9b. This feature usually allows for a more conformal dose coverage of the tumor with beams impinging from a lower number of angles, even a single one in some particular cases.

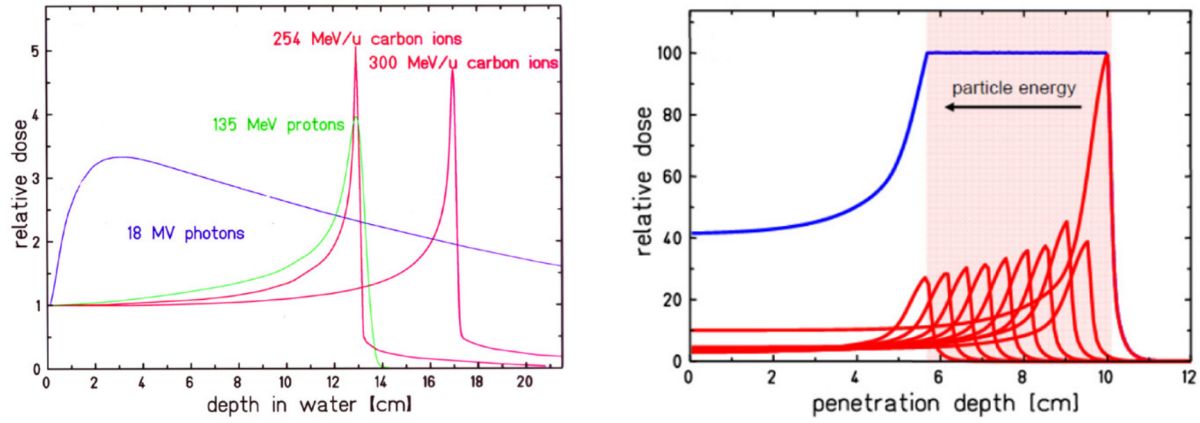

(a) (b)

Figure 1.9: (a) Comparison of depth-dose profile for photons and light ion beams at therapeutic energies in water. (b) Example of Spread-Out Bragg Peak for a proton beam. The read area marks the region to treat. (from [6]).

Considering the resulting dose deposition profiles, the advantage of using hadron beams is evident when treating deep-seated tumors. As a matter of fact, the Bragg

curve is optimal to deliver the highest amount of dose at a certain depth in the patient while keeping a limited damage in all the surrounding healthy tissues. Moreover, the range of hadron beam is well defined, meaning that dose after the Bragg peak is either zero (for protons) or strongly reduced (for heavier ions). This means that hadrons make it possible create much more conformal dose distributions, i.e. with a precise coverage of the disease, and effectively treat tumors that are located near *Organs At Risk (OAR)*. A comparison between treatment plans using protons or photon beams for a case of lung cancer is reported in Figure 1.10. From this picture, it is clear how the dose absorbed by healthy tissues and OAR is much lower and more localized with hadronic beams. Moreover, it can also be noticed that the protontherapy treatment has been obtained delivering the beam from a single angle, while the conventional X-ray treatment needs multiple.

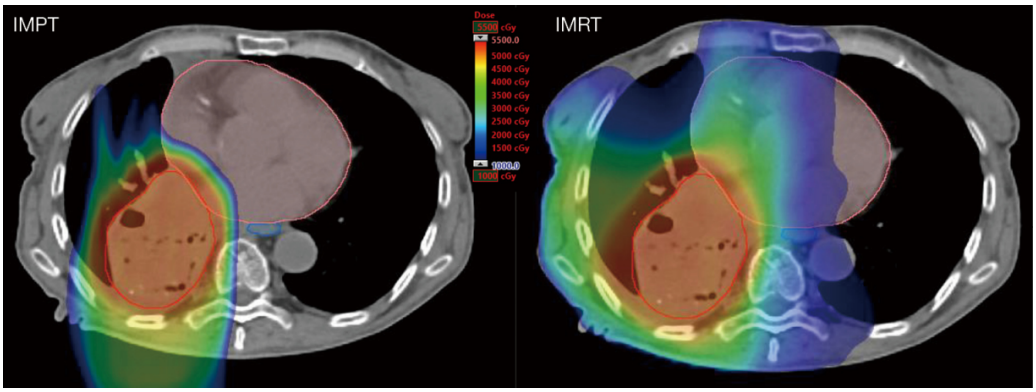

Figure 1.10: Comparison of dose profiles for the treatment of a lung cancer in Protontherapy (left) and Intensity Modulated Radiotherapy (right). The heart and esophagus of the patients have been considered as OAR in the treatment plan. They are highlighted in the pictures in pink and blue, respectively. (from [30]).

Another feature that can be noticed from Figure 1.9a is that ^{12}C ions have a significantly higher and narrower Bragg peak with respect to protons. This means that, in principle, heavier nuclei are more precise in hitting the tumor and further optimize the ratio between dose in diseased and healthy tissues. However, the usage of heavier primaries is usually more complicated with respect to protons, mainly because of the machine needed to create such beams. As a matter of fact, protons can be accelerated up to therapeutic energies using cyclotrons, while a synchrotron is needed for heavier ions. These machines require more space and are much more expensive, which is the main reason why not many facilities in the world are able to treat with ions heavier than protons.

The second drawback of using nuclei heavier than protons for treatment is the noticeable dose tail that appears after the Bragg peak, visible in Figure 1.9a. This issue will be better addressed in Section 1.2.3.

1.2.2 Relative Biological Effectiveness

The second main advantage of hadron beams is their enhanced biological effectiveness with respect to X-rays. The severity of the damage to DNA induced by therapeutic beams is not only linked to the absorbed dose, but it depends on a series of biological (tissue radiosensitivity, cell cycle, etc.) and physical (type and energy of the radiation, etc.) factors. Among these latter, one of the most important is the density of ionizations

caused by the beam inside the patient and it can be measured through a quantity called *Linear Energy Transfer (LET)*.

LET is similar to the stopping power defined in Equation 1.1, but it does not include all the energy released in the medium via radiative losses and δ-rays. It is usually defined as

$$LET = \left(\frac{\mathrm{d}E}{\mathrm{d}x}\right)_{\Delta} \tag{1.18}$$

where Δ represents a cut-off value excluding any higher energy loss. With such definition, LET gives a meaurement of the energy released per unit length along the track of the primaries, i.e. the actual energy deposition in the patient tissues. For indirectly ionizing radiation beams (like photons or neutrons), LET is calculated through the stopping power of secondary particles [31].

In clinical practice, different types of radiation are characterized through their LET and categorized as sparsely ionizing (low-LET, ~ 1 keV/μm) and densely ionizing (high-LET, $\sim 10 - 100$ keV/μm). In particular

- X-rays are referred to as low-LET particles, since they deposit dose in the patient through low-LET secondary electrons. Photons can interact inside the patient via photoelectric effect, Compton scattering or pair production. Since all of these processes have low cross section, photons rarely interact more than once inside the body. This means that the total number of ionizations produced inside a cell per incident photon is very small.

- Hadron beams are considered high-LET radiation, since they ionize a high number of atomic electrons along their track. This is a consequence of the very short mean free path of hadrons inside a medium, which is of the order of 1-10 nm for PT energies. This means that hadrons produce a much higher ionization density and have better chances of interacting multiple times with the same DNA molecule.

As a consequence, high-LET radiation has an higher chance to produce a damage on DNA strands that cells can not repair, meaning that it is more efficient in killing them. This also implies that hadrons need to deposit a lower quantity of dose, with respect to photons, to produce the same amount of tissue damage. This particular feature is usually quantified through *Relative Biological Effectiveness (RBE)*, which is defined as the ratio between the dose D_X of a reference radiation and the dose D of another type of radiation needed to achieve a certain biological effect

$$RBE = \left.\frac{D_X}{D}\right|_{\text{same effect}} \tag{1.19}$$

D_X is evaluated using photon beams (γ-rays from ^{60}Co decay), so RBE is defined unitary for X-rays and higher for hadron beams. In Equation 1.19, the "same biological effect" usually refers to a certain cell survival rate r, i.e. D and D_X are evaluated when only a fraction r of the cell population survives after the irradiation. In this cases, the the RBE is indicated as RBE_r (e.g. RBE_{10} for a 10% cell survival rate).

RBE depends on many different quantities, such as LET, dose, fractionation of treatment, tissue type and it can change along particle tracks. The typical behavior of RBE as a function of LET for some densely ionizing beams is reported in Figure 1.11. Experimental data show that RBE continuously grows as LET becomes higher, up to a peak value for LET $\sim$ 100-200 keV/μm. After this peak, the RBE value starts decreasing because of

overkilling effects, i.e. cells are damaged more than what is needed to cause their death and tissues receive some unnecessary dose. The actual position of the peak depends on the primary and it shifts to higher LETs for heavier ions.

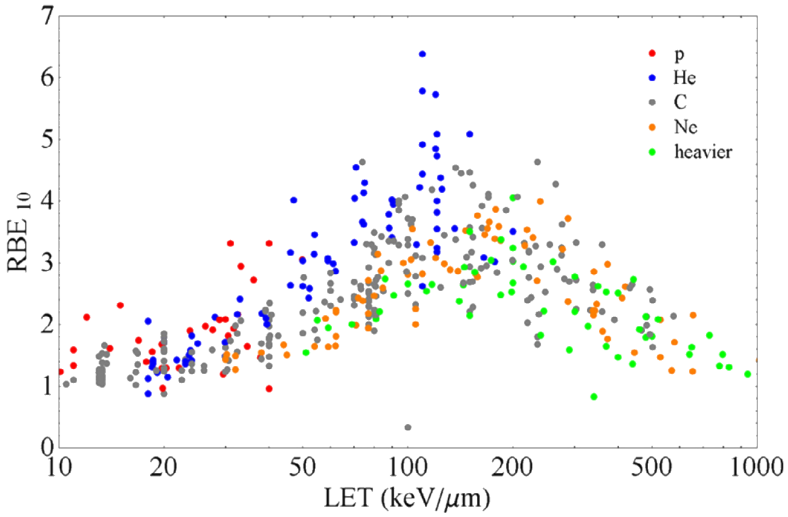

Figure 1.11: RBE_{10} as a function of LET for different ions. The data shown here, published in the PIDE database [32], refer to the values obtained in in-vitro studies of cell survival (from [33]).

RBE is a crucial quantity in radiotherapy since it introduces the concept of RBE-weighted dose or biological dose, a key parameter in TPS. This quantity is measured in Gy-RBE and is obtained multiplying the absorbed dose D by the RBE of the used radiation. It expresses the X-ray dose needed to obtain the same biological effect as the radiation of interest. Thus, RBE-weighted dose gives a more accurate estimate of the biological damage caused to each region hit by the beam. An example of the difference between absorbed and RBE-weighted dose is given in Figure 1.12. In most of modern TPS, PT treatments are based on this quantity, which is considered to be more reliable than absorbed dose. TPS usually include theoretical models that somewhat account for RBE variability of ion beams along their path, mainly caused by high LET changes. As a matter of fact, the LET of PT beams is significantly higher at the Bragg Peak than at the entrance channel. This implies that hadrons have an higher RBE at the end of their path, which makes them even more suitable in the treatment of deep-seated radio-resistant tumors.

1.2.3 Impact of nuclear fragmentation

One of the fundamental differences between conventional radiotherapy and PT is the impact of nuclear interactions. In the first case, collisions between X-rays and the nuclei of the medium play a completely negligible role, both in terms of energy deposition and beam attenuation. In conventional radiotherapy the only relevant beam-nucleus interaction is electromagnetic, with possible production of $e^- - e^+$ pairs. Instead, nuclear collisions in PT involving fragmentation of the target and projectile nuclei can both modify the depth-dose profile and the RBE of the beam.

The first effect caused by inelastic nuclear interactions is a decrease of the fluence of primaries along the beam path inside the patient. As shown in Figure 1.13, the number of primaries arriving at the level of the Bragg Peak can be significantly reduced by nuclear

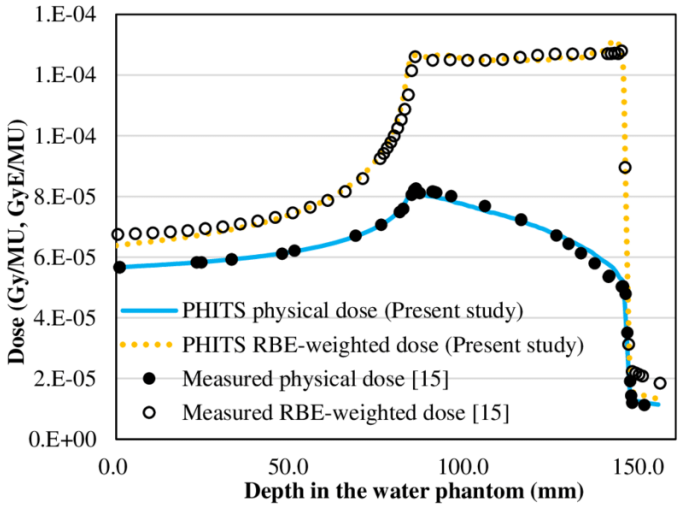

Figure 1.12: Comparison of absorbed (physical) and RBE-weighted dose for a ^{12}C ion beam at 290 MeV/u in water. The graph shows both measurements and Monte Carlo results generated with the code PHITS (from [34]).

interactions. This means that such processes play an important role in PT and thus have to be properly taken into account during treatment planning. As already mentioned in Section 1.1.3, particles emitted in target and projectile fragmentation have very different properties, which can be used to understand their impact in PT.

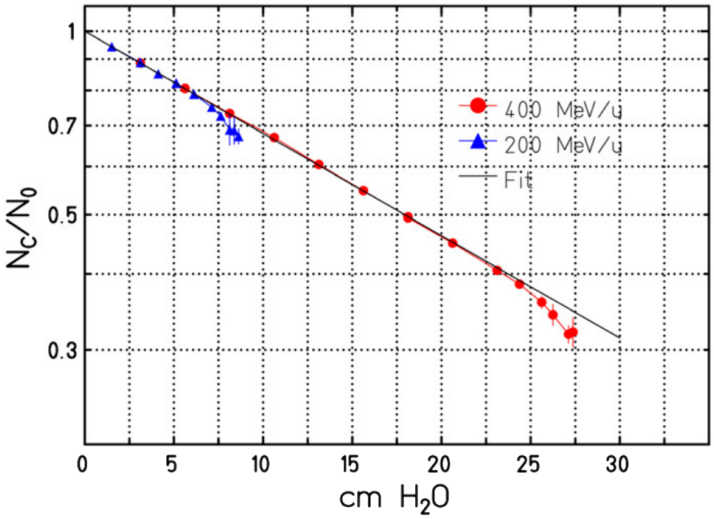

Figure 1.13: Measured attenuation of a ^{12}C beam at 200 and 400 MeV/n in water. For these two cases, the number of primaries reaching the Bragg Peak region is around 70% and 30% respectively (from [35]).

In proton therapy only target fragmentation is possible since the projectile is made of a single nucleon. Fragments produced in such interactions are mainly short-ranged, high-LET particles that release their whole energy very close to the point of interaction. This alters the shape of the depth-dose profile, with a relevant impact on the total dose deposited before the Bragg Peak and enhancing the risk for radiation damage in healthy tissue. Figure 1.14b shows the contribution of primaries and secondary particles to the Bragg curve of a proton beam. As it is noticeable here, the amount of dose deposited

by target fragments is quite relevant in the entrance channel. Figure 1.14b shows the biological implications of this process. The ratio of cell killed by fragmentation reactions and ionization is expected to be $\sim 1/40$ at the Bragg Peak, while it is much higher in the entrance channel, around 1/10. [36, 37]

Target fragmentation could also explain the observed variability of proton RBE. Since their LET does not change too significantly along the beam path, in clinical practice the RBE of proton beams is conventionally set to a constant value of 1.1. However, many radiobiological studies have highlighted a non negligible RBE increase both in the entrance channel and in the SOBP, with values reaching up to 1.6. [38] Even though RBE dependency is less important in protontherapy, the choice of using a constant value could lead to an underestimation of the biological effect, with a consequent higher risk of complications at the edges of the treated region.

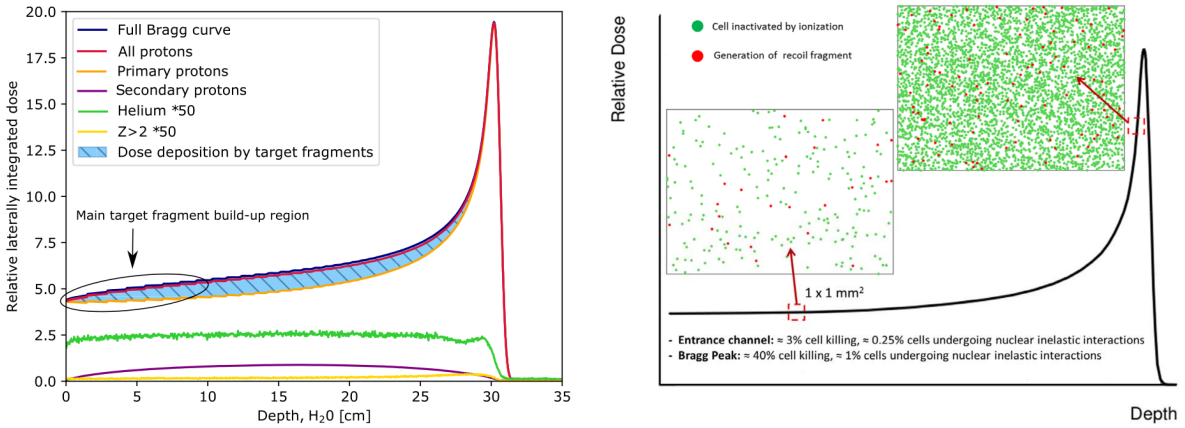

(a) (b)

Figure 1.14: (a) Contribution to dose deposition of a 220 MeV proton beam from primaries and fragments generated along the beam path. (from [39]). (b) Percentage of cell killing from ionization and fragmentation reactions along the path of a proton beam. (from [37]).

Instead, in ion therapy treatments, both target and projectile fragmentation are possible. As shown in Figure 1.13, in a typical carbon treatment a relevant fraction of primaries undergoes inelastic nuclear collisions producing a significant number of secondary particles. Target fragments contribute to dose profiles in the same way described above for protons. Instead, projectile fragments are fast particles emitted mainly in the forward direction. Since they retain almost the same speed of the primary but are lighter (higher M/Z^2), these fragments have a longer range and deposit their energy also beyond the Bragg Peak. Figure 1.15 shows the contribution of projectile fragments to energy deposition for a ^{12}C therapy beam in PMMA, highlighting the dose tail created after the Bragg Peak region. This contribution to the dose profile is one of the main drawbacks of ion beam therapy and has to be carefully taken into account in treatment plans to avoid secondary irradiation of OAR. [6]

Nuclear fragmentation is also the main limiting factor in using higher Z beams in particle therapy. As a matter of fact, nuclei with higher Z have a narrower Bragg Peak (see Figure 1.9), which implies a better accuracy in the dose coverage of the tumor. However, as the mass number of the primary ion increases, the contribution of nuclear fragmentation becomes more and more relevant, up to the point where the dose deposition in the entrance channel matches that of the Bragg Peak (see Figure 1.16). This is the

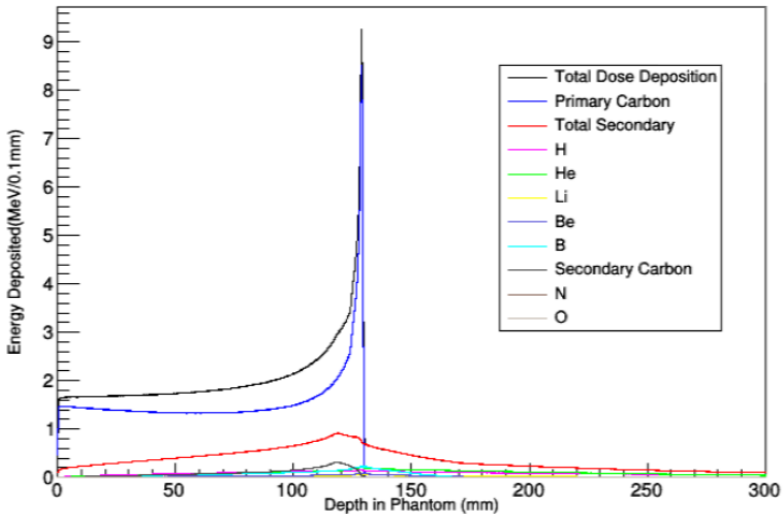

Figure 1.15: Contribution of projectile fragments to the energy loss profile of a 330 MeV/u ^{12}C beam on a PMMA (PolyMethyl MethAcrylate) from a GEANT4 MC simulation(from [40]).

main reason ions heavier than ^{16}O are not suitable for Particle Therapy treatments. [33]

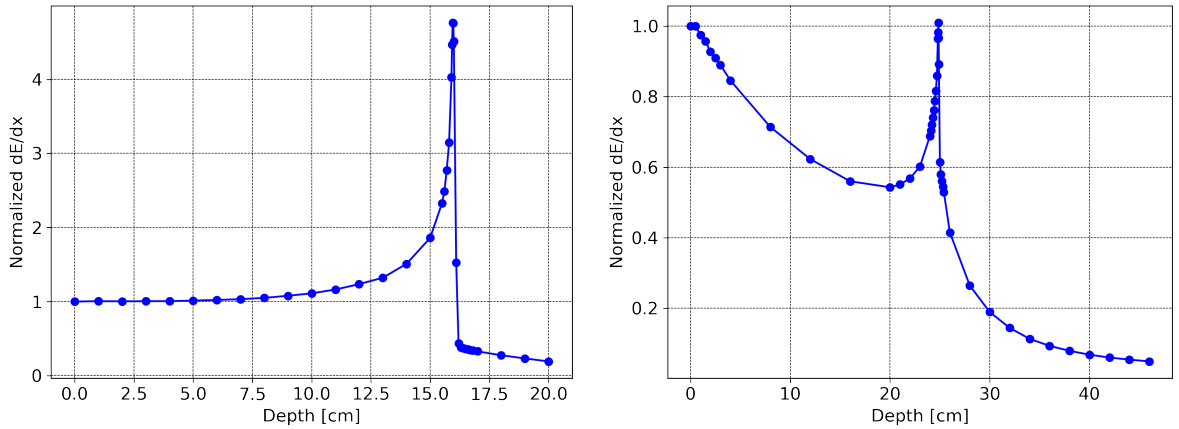

(a) ^{12}C at 293 MeV/u on PE (b) ^{56}Fe at 963 MeV/u on PE

Figure 1.16: Energy deposition (normalized to the entrance channel) of different ions in high density Polyethylene (ρ = 0.97 g/cm^3) showing the different shape of their Bragg Peak: (a) ^{12}C at 293 MeV/u and (b) ^{56}Fe at 963 MeV/u. (reproduced from [41]).

A correct evaluation of the impact of target and projectile fragmentation in PT strongly depends on the knowledge of cross sections for the relevant reactions. In particular, total cross sections are needed to calculate the variations in beam fluence along the track, while double differential cross sections would provide the characteristics of all the produced nuclear fragments (charge, mass, direction and velocity). However, the already mentioned lack of experimental measurements for such reactions makes it currently impossible to evaluate the role of fragmentation with sufficient accuracy. As a matter of fact, the modern TPS used to perform dose profile calculation and radiation risk assessment are tuned using complex MC simulations of beam-patient interactions. However, the results of such simulations are, in turn, tuned to reproduce experimental cross sec-

tions as closely as possible. In this context, double differential cross sections constitute the perfect benchmark for nuclear reaction models used in MC codes. This means that such measurements are crucial to obtain a further optimization of modern TPS. [38]

1.3 Radiation protection in Space

In the last decades, space agencies have shown an increasingly strong interest in performing more human missions. The main objectives in this context are further exploration of the Moon and the first ever travels to Mars. To reach such goals, NASA and ESA have already started a careful assessment of health risks for astronauts in long-term missions. In addition to physiological alterations and psychological distress, one of the main issues addressed is the evaluation of radiation exposure during the whole duration of the mission. As a matter of fact, the magnetic fields and the atmosphere surrounding the surface of the Earth provide natural shielding from most of the radiation coming from outer space. Instead, in the interplanetary space there is no such protection and the rate of natural radiation exposure increases significantly, even more than a factor 100 with respect to the Earth surface. The increased dose absorption could potentially cause relevant issues to both the astronauts and spacecraft components, which could make it impossible to perform long term missions.

The final goal of RS studies is to make it possible for humans to perform such missions with an acceptable level of risk. The success of exploration programs strongly depends on the ability to find proper ways to deal with the space radiation environment. This means that an accurate knowledge of the type and energy spectrum of the involved particles and their interactions with the materials and crew of the spacecraft is mandatory both for risk assessment calculations and for the development of effective countermeasures. While the cosmic radiation field is well characterized, its impact on the health of astronauts is still very difficult to evaluate [42]. Risk assessment evaluation is usually performed using particle transport codes, which accuracy depends on the knowledge of radiation interaction with the spacecraft materials.

Since space radiation also includes particles at high energy, the main issue in this sense is the contribution of nuclear interactions, which leads to the production of secondary fragments. The correct modeling of fragment yield and kinematics strictly depends on experimental measurements of fragmentation cross sections, which are currently very scarce in literature. As a consequence, current estimates of health hazards for astronauts in long term missions are still affected by large uncertainties for what concerns both acute and late effects (see Figure 1.17). This means that exposure limits for materials and crew can vary significantly, creating further difficulties in international space mission agreements [33].

1.3.1 Space radiation environment

The space radiation environment is very different from that of the surface of the Earth. In this latter, natural radiation is mainly caused by the decay of radioactive isotopes in the ground and air. Instead, cosmic radiation is composed of many different particles, mainly protons and heavy ions, over a wide energy range. The main sources of radiation in space which could lead to significant exposure in long term missions are *Galactic Cosmic Rays (GCRs)* and *Solar Particle Events (SPEs)*.

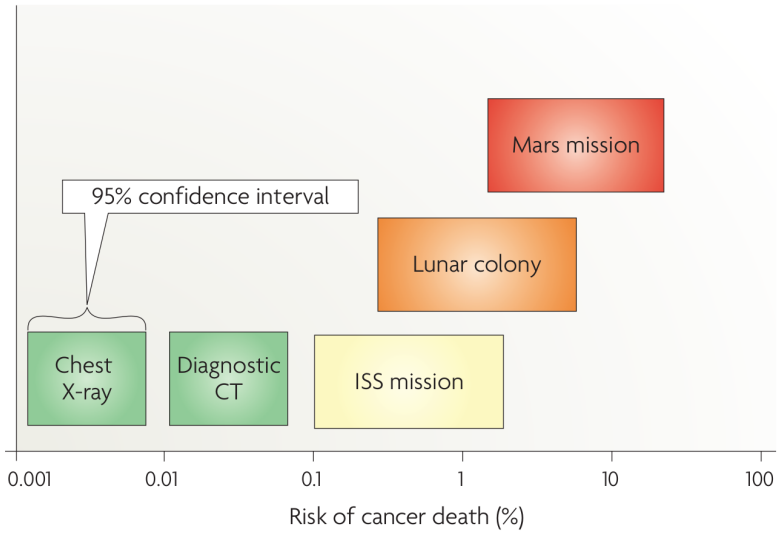

Figure 1.17: Estimation of the risk of cancer death for radiation exposure in different scenarios. The width of each entry represents the 95% confidence interval for all calculations (from [43]).

Galactic Cosmic Rays (GCRs) consist of particles generated outside of the Solar System which impinge isotropically on the Earth. GCR consist of baryons (98%) and electrons (2%) that originate from high energy phenomena in neutron stars, pulsars and supernova explosions. The baryonic component is made of protons (85%), helium (14%) and heavier nuclei (1%) in a very wide energy spectrum, up to 10^{20} eV, which peaks between 100 MeV/u and 1 GeV/u for all particles. The energy spectrum of some GCR ions is reported in Figure 1.18a. The graph shows the impact of solar activity on GCRs, with the spectra moving to higher energies and lower fluence when the Sun is more active. It can also be noticed that the influence of our star becomes negligible at higher GCR energies, above 10-100 GeV/u [44, 45].

Figure 1.18b shows the relative fluence, dose and equivalent dose contribution of different GCR ions as a function of their charge. Nuclei heavier than He are usually referred to as HZE (high charge Z and high energy E). Since dose scales with the square of charge, HZE contribute significantly to total dose absorption even if their fluence is lower, as shown in Figure 1.18b. In a typical travel to Mars, HZE contribute to about $30-40\%$ of the total absorbed dose. Moreover, HZE are high-LET radiation, have high penetrating power and enhanced biological effectiveness. [33, 43].

The second main source of radiation in the interplanetary space is the Sun. Apart from the electromagnetic radiation, the Sun also continuously ejects particles, mainly protons and electrons, through the so-called solar wind. The energy of such particles is usually very low (from 100 eV to 3.5 keV for protons), meaning that they have a very short range and will be stopped in the first few nm of skin. These particles pose no concern in terms of radiation protection because they can be easily shielded. [44]

However, the Sun occasionally releases large energy bursts in the form of radio waves and X-rays which can strongly accelerate particles in the solar matter. The result of these Solar Particle Events (SPEs) is the emission of ions with several GeV of energy from the solar corona. The energy spectra of some intense SPEs is shown in Figure 1.19. The particles emitted are mainly protons and a small fraction of heavier nuclei. SPEs are occasional phenomena which happen around 5-10 times per year when the Sun is not at

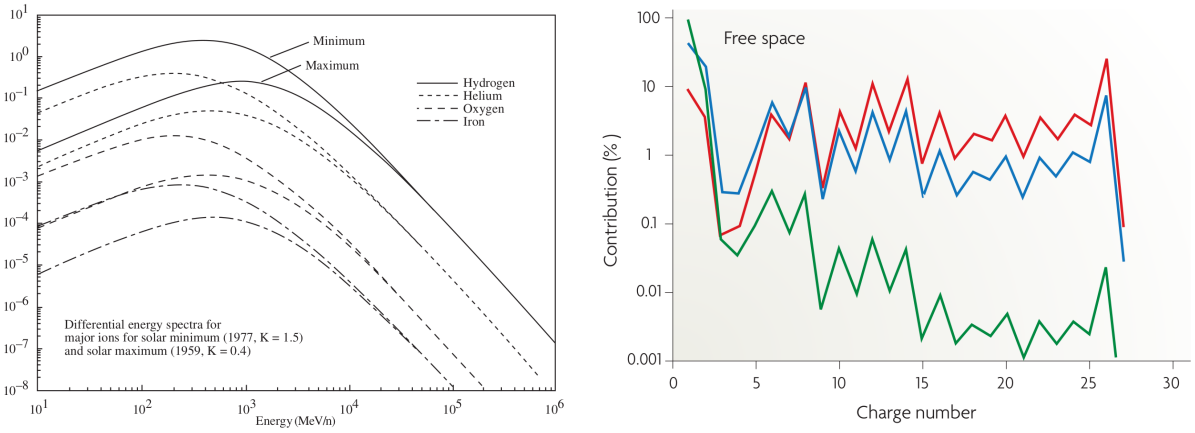

(a) (b)

Figure 1.18: (a) Energy spectrum of GCRs at solar minimum and maximum for some relevant charged ions (from [44]). (b) Relative contribution to total GCR fluence (green), dose (blue) and equivalent dose (red) as a function of charge (from [43]).

its minimum activity.

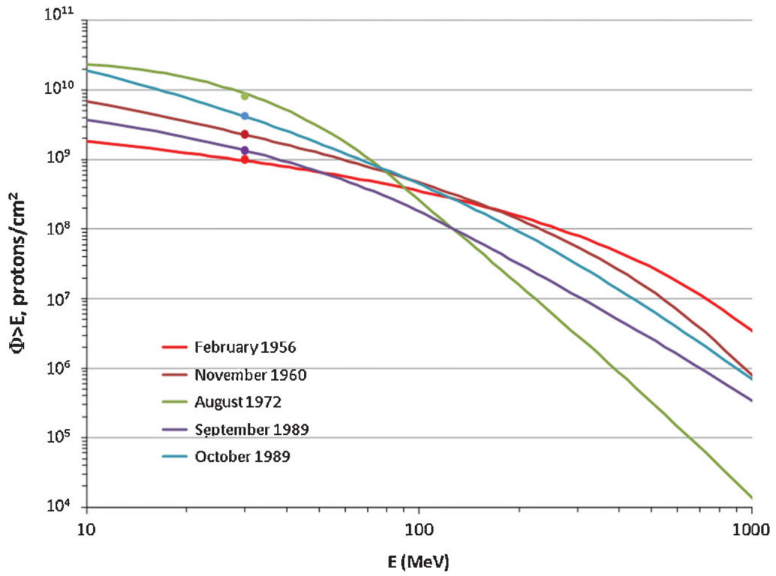

Figure 1.19: Integral flux of some intense SPEs as a function of particle energy (from [44]).

As said above, the Sun acts as a modulator of GCR fluence, which significantly decreases when the star is more active. However, an higher activity of the Sun also implies an increased probability of SPEs occurring. Even if the energy of emitted particles is lower than that of GCRs, SPEs show a significant variability in particle fluence and the most intense ones could potentially lead to acute effects or even life threatening dose absorption. This means that the prediction of SPEs is very important to avoid health and operational issues to astronauts [44].

1.3.2 Radiation shielding in space

The minimization of exposure is a fundamental topic in any field involving radiation protection. In general, there are three main methods to reduce radiation exposure:

- Increase the distance from the radiation source.
- Minimize as much as possible the time of exposure.
- Shield the people and materials exposed through passive materials that can absorb the radiation.

In a space environment, the first two methods can not be exploited. On the one hand, the cosmic radiation field is isotropic, which means that changing the distance from the radiation source is not possible. On the other hand, space agencies are interested in increasing as much as possible the duration of their explorations (and future colonization), which goes in the opposite direction of exposure time minimization. The only possibility in this sense is to reduce the time of travel in the interplanetary space, i.e. when radiation exposure is at its maximum. Some studies, like the one reported in [46], have shown that this would significantly reduce the total absorbed dose by the astronauts, but this constitutes only a partial solution to the problem.

The main technique used to decrease radiation exposure in a space environment is shielding. The very complex and varied nature of space radiation is the main difficulty in spacecraft shielding design. Moreover, the composition and energy of the radiation field change while traversing the structure of the vehicle, both from ionization energy loss and from nuclear fragmentation. In general, from the radiation protection point of view, the goal is to find an optimal compromise between electromagnetic and nuclear interactions in the spacecraft materials to lower as much as possible the dose to the crew.

On the one hand, electromagnetic interactions have to be taken into account since they can be exploited to stop low energy ions with modest quantities of material. At the same time, the LET of ions decreases with the inverse square of the velocity. This means that, for a given thickness of material, all ions with enough energy to emerge from the shielding will have an higher LET and thus will be more harmful than what they would have been for thinner absorbers. On the other hand, HZE particles traversing the shielding undergo nuclear interactions that lead to fragmentation, with the consequent production of lighter charged nuclei and neutrons. While it is true that projectile fragments have longer range than that of the primary ion (see Equation 1.7), secondary particles are usually less biologically hazardous. Thus, fragmentation reactions might be also used as a means to decrease the risks linked to radiation exposure in space [47].

The influence of both electromagnetic and nuclear interactions is usually evaluated considering the characteristics of shielding materials. Regarding electromagnetic interactions, the quantities used to compare different materials are the mass stopping power $\mathrm{d}E/\mathrm{d}\chi$, already defined in Section 1.1.1, and the *mass thickness* or *aerial density*, which is the product of density and thickness of the medium. From Equation 1.1 we get, as a first approximation, $\mathrm{d}E/\mathrm{d}\chi \propto Z_t/A_t$, i.e. the number of electrons per nucleon in the material. This means that lighter materials have a much higher mass stopping power than heavier nuclei for the same mass thickness, as already noticeable from Figure 1.1. Figure 1.20 shows an example of mass stopping power measurement as a function of mass thickness for different shielding materials.

For what concerns nuclear interactions, simplified phenomenological descriptions show that the reaction cross section is approximately proportional to $A_t^{2/3}$ [14]. Considering

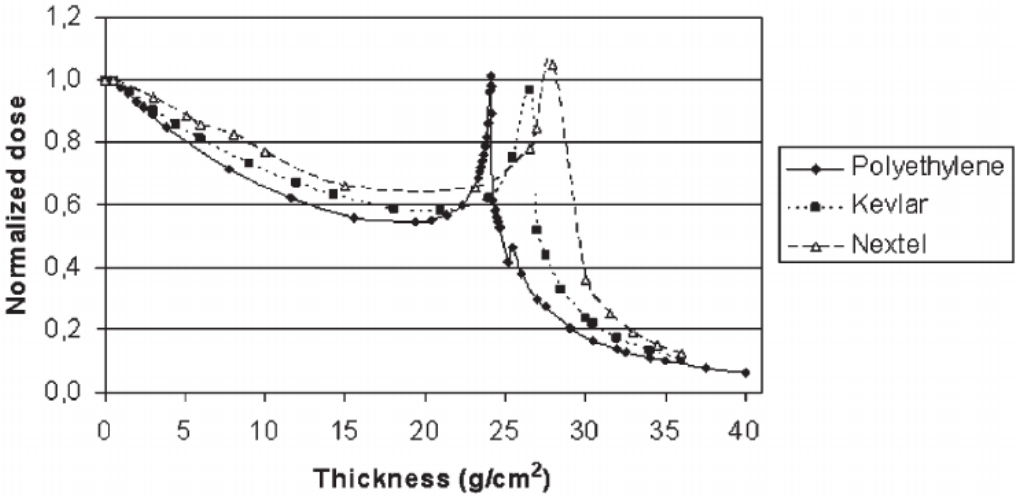

Figure 1.20: Bragg curves for 1 GeV/u ^{56}Fe ions on different materials (from [48]).

that the number of target nuclei per unit mass is equal to N_A/A_t, the total reaction cross section per unit mass of material is proportional to $A_t^{-1/3}$. This means that, for an equal mass, shielding materials with lower A_t maximize the number of nuclear interactions.

Figure 1.21 shows measurements of dose reduction per unit of mass thickness of different shielding materials. As expected, lighter materials show the best performance in terms of radiation shielding. At the same time, the use of light materials has the further advantage of keeping the overall weight of the shielding, and thus of the whole spacecraft, limited. This means that, in principle, liquid hydrogen is the best possible choice to both maximize dose reduction and minimize the weight of the shielding. However, it is not a viable solution since it needs to be kept at very low temperature and its highly reactive nature. For the moment, hydrogen-rich materials seem to constitute a reasonable solution.

It can be noticed that Figure 1.21 also contains an entry named "Mars bar", which is representative of Mars regolith. This material is currently being studied as a possible choice for shelter construction on the planet in view of future colonization missions [47].

In spacecraft shielding design it is normal to consider a combination of different materials. The assessment of their performance in terms of dose reduction is usually performed through particle transport codes, either deterministic or Monte Carlo based. The same tools are used to study possible novel materials that could be employed in radiation shielding and, in general, to model the response of materials that have not been yet characterized through dosimetric measurements. The accuracy of this approach is strongly dependent on the availability of experimental measurements, which serve as a fundamental tool for the validation of the models used in transport codes. However, as stated above for PT treatment plans, inelastic nuclear reaction cross section data are very scarce in literature, especially in the energy range near the peak of space particle radiation. Early estimates of cancer death risk show an uncertainty going up to 400% of the mean projected value for future Moon and Mars missions [49]. One of the main sources of uncertainty is given by the lack of double differential cross sections in terms of fragment kinetic energy and emission angle. An in-depth knowledge of such data, in combination with further radiobiological studies, could lead to a significant improvement in the accuracy of risk assessment calculation for both acute and late effects in space radiation environment.

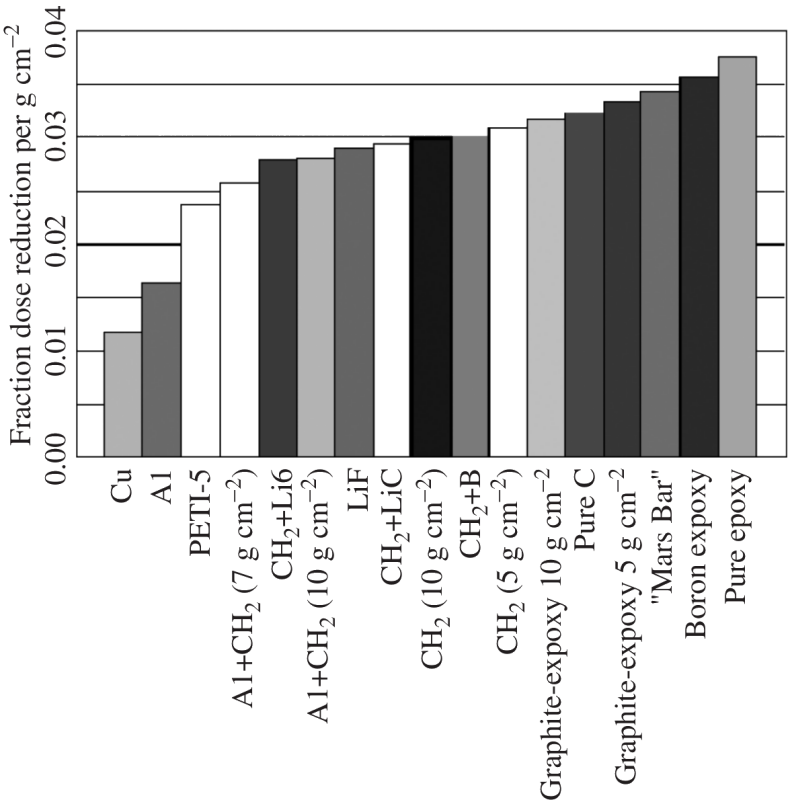

Figure 1.21: Dose reduction per unit of mass thickness for different materials. The measurements have been performed using ^{56}Fe ions at 1 GeV/nucleon (from [47]).

Chapter 2

The FOOT experiment

The lack of experimental data for nuclear fragmentation reactions in the energy range of interest for Particle Therapy and Radiation Protection in Space created a new interest in the characterization of such processes.

The FOOT (FragmentatiOn Of Target) experiment aims at filling the gaps in nuclear databases by performing a set of double differential cross section measurements for nuclear fragmentation reactions of light nuclei ($Z \leq 8$) in the energy range between 200 and 800 MeV/u. The final goal is to obtain such measurements with a resolution at the level of 5% for double differential cross sections of projectile fragmentation reactions and at the level of 10% for target fragmentation measurements. [50]

One of the main challenges of the experiment is that the beams needed to accurately characterize target and projectile fragmentation are available in different facilities. The experimental program foresees measurements at CNAO (Centro Nazionale di Adroterapia Oncologica) in Pavia (Italy), GSI in Darmstadt (Germany) and Heidelberg Ion Therapy center (HIT, Germany). This implies the need to create a portable setup that can be moved and installed in the different facilities, while maintaining the required precision on cross section measurements.

In order to guide the design of the experiment, extensive Monte Carlo (MC) studies have been performed using the FLUKA code. [51, 52] Figure 2.1 shows an example of the expected kinetic energy and emission angle of the nuclear fragments produced by a ^{16}O beam at 200 MeV/u impinging on a C_2H_4 target. As it can be seen, heavier fragments are expected to be mainly emitted in the forward direction and with a kinetic energy per nucleon close to that of the primaries, while lighter fragments show much wider distributions.

Taking this into consideration, FOOT foresees to employ two complementary setups to carry out its physics program:

- The *Electronic setup*, focused on the characterization of heavier nuclear fragments ($3 \leq Z \leq 8$) and with an angular acceptance of up to 10° from the beam axis.

- An *Emulsion spectrometer* based on nuclear emulsion films, optimized for studies on lighter fragments ($Z \leq 3$) and with an angular acceptance close to 70°.

The main reason for this choice is the difficulty to create an effective tracking system of limited size while keeping a good angular acceptance for all the fragments involved.

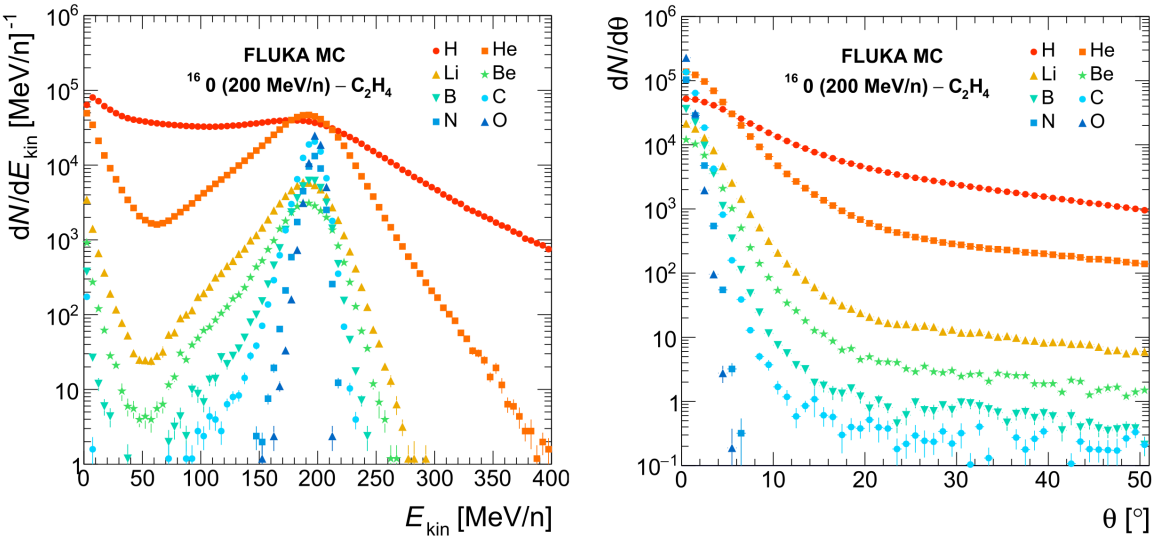

(a) (b)

Figure 2.1: (a) Kinetic energy and (b) angle of emission of nuclear fragments produced in the interaction of a 200 MeV/u ^{16}O beam on a C_2H_4 target. The plots shown have been obtained from a MC simulation with FLUKA (from [50]).

2.1 Cross section measurement and inverse kinematic approach

Both setups of FOOT have been conceived as fixed target experiments with the capability to study the kinematic characteristics of nuclear fragments and their production yields. The experimental program of FOOT comprehends a set of measurements with ^{4}He, ^{12}C and ^{16}O beams of 200-800 MeV/u impinging on different targets with chemical composition representative of human tissues (mainly H, C and O). A summary of the physics program of the experiment is reported in Table 2.1.

Fragmentation	Research Field	Beam	Energy [MeV/u]	Target	Kinematics
Projectile	Therapy	^{4}He	250	C, C_2H_4, PMMA	direct
Projectile	Therapy	^{12}C	400	C, C_2H_4, PMMA	direct
Projectile	Therapy	^{16}O	500	C, C_2H_4, PMMA	direct
Projectile	Space	^{4}He	800	C, C_2H_4, PMMA	direct
Projectile	Space	^{12}C	800	C, C_2H_4, PMMA	direct
Projectile	Space	^{16}O	800	C, C_2H_4, PMMA	direct
Target	Therapy	^{12}C	200	C, C_2H_4	inverse
Target	Therapy	^{16}O	200	C, C_2H_4	inverse

Table 2.1: Summary of the experimental program of the FOOT collaboration.

As it can be noticed, the measurements relative to target fragmentation reactions will be performed using an *inverse kinematic approach*. This choice was dictated by the different characteristics of the particles produced in such processes. Contrary to projectile fragments, which are usually emitted with the same speed of the primary, target fragments

have much lower energy and, thus, a very short range. As already stated in Section 1.2.3, the path length expected for target fragments produced by a typical beam for proton therapy inside a patient is of the order of 10-100 μm. This means that even a target of only a few mm thickness would stop all the fragments, making it impossible to detect them. On the other hand, employing an even thinner target would introduce further issues, both in terms of mechanical stability of the system and of strongly reduced reaction rates (i.e. very long data acquisitions).

FOOT aims at overcoming such issues using an inverse kinematic approach. This consists in reversing the roles of target and projectile ions: instead of using a proton beam on a tissue-like target, FOOT will employ carbon and oxygen beams impinging on hydrogen-enriched targets. If the primaries have the same velocity (i.e. the same kinetic energy per nucleon), these two scenarios are linked only by a change of reference frame, i.e. a Lorentz transformation. The fundamental difference is that, in the latter case, the fragments generated in nuclear fragmentations are much more energetic and can easily escape the target and be detected.

Considering an ion beam moving along the positive z axis at constant velocity β towards a proton, two reference frames can be defined: the laboratory frame S, where the ion is moving and the proton target is at rest, and the patient frame S', where the situation is reversed, i.e. the ion is at rest and the proton is moving with speed β in the negative z direction. The 4-momenta of the ion in S and of the proton in S' are given by $\mathbf{P} = (E/c, \vec{p})$ and $\mathbf{P'} = (E'/c, \vec{p}')$ respectively, where E and E' are the total energies of the two particles in the respective frames. The components of the proton 4-momentum in S' can be written as

$$\begin{aligned} \frac{E'}{c} &= \gamma\left(\frac{E}{c} - \beta p_z\right) \\ p'_x &= p_x \\ p'_y &= p_y \\ p'_z &= \gamma\left(-\beta\frac{E}{c} + p_z\right) \end{aligned} \tag{2.1}$$

which can also be expressed as

$$\mathbf{P'} = \mathbf{\Lambda}(\beta)\mathbf{P} \tag{2.2}$$

where $\mathbf{\Lambda}(\beta)$ is a 4x4 matrix describing the Lorentz transformation between S and S'

$$\mathbf{\Lambda}(\beta) = \begin{pmatrix} \gamma & 0 & 0 & -\beta\gamma \\ 0 & 1 & 0 & 0 \\ 0 & 0 & 1 & 0 \\ -\beta\gamma & 0 & 0 & \gamma \end{pmatrix} \tag{2.3}$$

The inverse transformation is

$$\mathbf{P} = \mathbf{\Lambda^{-1}}(\beta)\mathbf{P'} \tag{2.4}$$

with the inverse matrix $\mathbf{\Lambda^{-1}}(\beta)$ being

$$\mathbf{\Lambda^{-1}}(\beta) = \begin{pmatrix} \gamma & 0 & 0 & \beta\gamma \\ 0 & 1 & 0 & 0 \\ 0 & 0 & 1 & 0 \\ \beta\gamma & 0 & 0 & \gamma \end{pmatrix} \tag{2.5}$$

which means that, knowing the velocity of the velocity β of the primary ion, the two transformations are simply linked by a change of sign

$$\mathbf{\Lambda^{-1}}(\beta) = \mathbf{\Lambda}(-\beta) \tag{2.6}$$

From the description given above, it is clear that the possibility to use inverse kinematics to perform cross section measurements relies on a very good accuracy in the reconstruction of the trajectories of primaries before the interaction and of the produced fragments. As stated in [53], the correct application of the Lorentz transformation is only possible if the emission angles of fragments can be measured with a maximum uncertainty at the level of 1 mrad. This requirement also provides a constraint on target thickness, mandatory to reduce the contribution of Multiple Coulomb Scattering and secondary fragmentation reactions. In the final configuration, FOOT targets will need to be $\sim$ 2-5 mm thick and have a maximum mass thickness of about 1 g/cm^2, limiting the fraction of impinging primary ions expected to produce a fragmentation reaction to a few percent of the total [53, 50].

Another challenge for FOOT measurements is the impossibility to employ gaseous targets. Since the final configuration of the experiment has been conceived to acquire data at relatively low beam rates ($\sim$ 5-10 kHz), a gaseous target would imply very low reaction rates and, consequently, lead to excessively long acquisition time. Moreover, the particle beams needed by FOOT are usually available in clinical facilities and it would not be trivial to employ an hazardous material target in such structures. The same considerations apply to the use of liquid hydrogen and oxygen targets, which would also require a cryogenic system. This represents an important issue for measurements on H and O targets in both direct and inverse kinematics.

The solution proposed by the FOOT collaboration is to employ both mono-atomic (e.g. graphite) and composite targets, like PolyEthylene (C_2H_4) or PolyMethyl MethAcrylate (PMMA, $C_5O_2H_8$), and then extract single cross sections through difference. For example, the hydrogen cross section will be extracted from the results obtained with a graphite and a polyethylene target using the formula

$$\sigma(\mathrm{H}) = \frac{1}{4}\left[\sigma(\mathrm{C_2H_4}) - 2\sigma(\mathrm{C})\right] \tag{2.7}$$

which is also valid for differential and double differential cross section measurements. This technique has already being validated and applied in previous measurements, like the ones performed at GANIL and reported in [25]. The only real drawback of this technique is that the uncertainties on indirect cross sections can easily become quite relevant since they are obtained from a quadratic sum of those of single target measurements. However, the FOOT detectors have been designed to reach a precision on direct measurements that should allow for indirect cross section extraction with the desired resolution.

2.2 Electronic setup

The Electronic Setup of FOOT is the one dedicated to nuclear fragments heavier than ^{4}He. The whole setup is about 2-3 m long and has an acceptance of about 10° from the beam axis, compatible with the maximum emission angle expected for $Z \geq 3$ fragments. A sketch of the full Electronic Setup is reported in Figure 2.2.

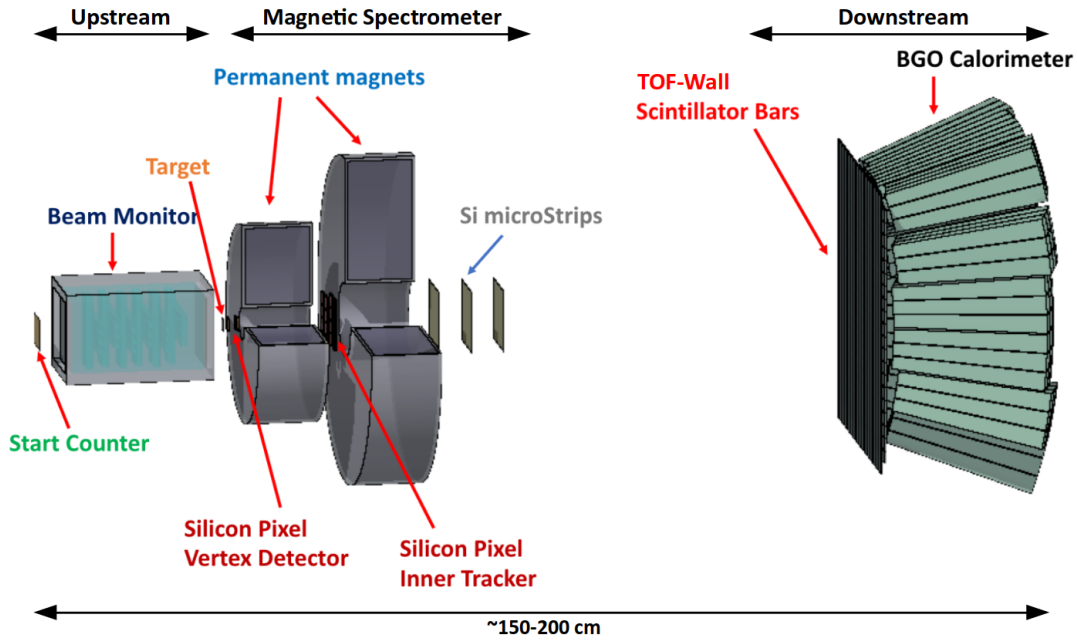

Figure 2.2: Schematic view of the FOOT electronic setup

To guarantee the accuracy requested for cross section measurements, the setup is conceived to accurately measure all the kinematic characteristics of the produced fragments. In particular, preliminary feasibility studies performed with Monte Carlo simulations showed that, for heavy fragments, the setup needs to achieve

- Relative momentum resolution $\sigma(p)/p$ of about 5%.
- Time-Of-Flight resolution σ(TOF) better than 100 ps.
- Relative kinetic energy resolution $\sigma(E_k)/E_k$ at the level of 2%.
- Relative energy loss resolution $\sigma(\Delta E)/\Delta E$ of the order of 4%.

These results need also to be achieved in a system as compact as possible, in order to place it in the experimental rooms available in the different facilities. The correct application of the inverse kinematic approach described in Section 2.1 relies on accurate angular measurements of the direction of both primaries and fragments and on solid particle identification capabilities. Considering the limited dimensions of the system, this request can be fulfilled through redundancy: the charge and mass of the fragments are determined in different ways to keep the systematic errors in the calculations as low as possible. In particular

- The mass number A of the particles is determined with three different approaches based on the concurrent measurements of momentum p, Time-Of-Flight TOF and kinetic energy E_k. These quantities can be combined two-by-two to obtain three

measurements of the particle mass number

$$A_1 = \frac{E_k}{Uc^2(\gamma - 1)} \tag{2.8}$$

$$A_2 = \frac{p^2c^2 - E_k^2}{2 \cdot U \cdot c^2 E_k} \tag{2.9}$$

$$A_3 = \frac{p}{U \cdot c\beta\gamma} \tag{2.10}$$

where $U = 931.5$ MeV is the Unified Atomic Mass and the Lorentz factors $\beta = v/c$ and $\gamma = 1/\sqrt{1-\beta^2}$ are evaluated from TOF measurements. The three values obtained for A with such method are correlated since each couple shares the information from one of the sub-detectors. The final A will be calculated through a fitting procedure, like χ^2 minimization or an Augmented Lagrangian Method [54]. The expected resolution for mass measurement with this approach ranges from about 3% to 6% [53].

- Charge identification is performed through the measurements of TOF and energy loss ΔE in a thin slab of plastic scintillator material. The atomic number Z of the particle is then calculated from the Bethe-Bloch formula (see Equation 1.1). For what concerns charge identification, redundancy is achieved by also measuring the energy loss in other detectors, in this case silicon trackers. The final resolution expected on Z should range from 6% for ^{1}H to about 2% for ^{16}O nuclei.

As shown in Figure 2.2, the final setup is divided in three main sections:

- the *upstream region*, which is dedicated to the measurement of primary beam characteristics and the start time of the event.
- a *magnetic spectrometer*, which tracks the trajectories of particles produced in the target and performs the momentum determination.
- the *downstream region*, which measures the energy loss, kinetic energy and stop time of the fragments.

2.2.1 Upstream region

The upstream or pre-target region of FOOT is made of two detectors with the aim of characterizing the incoming primary particles. The first detector seen by the beam is the Start Counter (SC), a 5x5 cm^2 EJ-200 (manufactured by Eljen Technology, Sweetwater, Texas) plastic scintillator foil with a thickness of 250μm and placed at about 20-30 cm before the target. The scintillation light produced by the passage of a primary in the SC is collected at each side by 12 Hamamatsu 3x3 mm^2 Multi-Pixel Photon Counter (MPPC) SiPMs with a microcell pitch of 25μm. [55] The SC has been developed by a collaboration of the University "La Sapienza", Centro Fermi and INFN section of Rome.

The main purpose of the SC is to provide the start time of each Time-Of-Flight measurement and generate the Minimum Bias trigger signal (see Section 2.2.4). The fast response of the detector coupled with the high sampling rate of the acquisition system (3 GSamples/s) makes it possible to achieve a time resolution of the order of 40-50 ps with this device. [56] The thickness of the scintillating material has been chosen in order to

minimize the impact on the primaries ($\ll 1\%$ of interaction probability) while maintaining its good time resolution. The SC is also used to monitor the rate of primaries impinging on the setup with an observed efficiency close to 1 up to 10 kHz [57], which is perfectly compliant with the needs of the experiment. Figure 2.3 shows a picture of the detector with its aluminum frame. The outer black casing is used to shield the detector and the SiPMs from environmental background light.

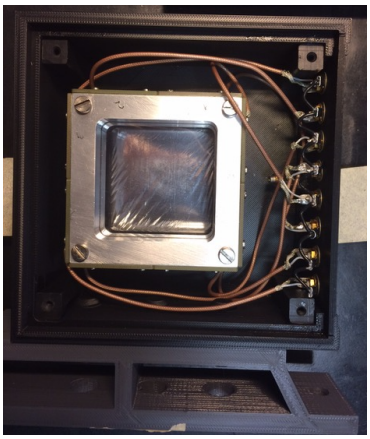

Figure 2.3: Picture of the Start Counter detector in its mechanical frame and outer casing.

The second detector of the upstream region is the Beam Monitor (BM), an Ar/CO_2 (80/20%) drift chamber. The BM has been inherited from the FIRST experiment at GSI. [58] The choice of this kind of detector was driven by the need to lower as much as possible the amount of material before the target. The chamber has a transverse active area of 5.6x5.6 cm^2 and contains 12 layers of alternating horizontal and vertical wires. Each plane is divided in three 16x11 mm^2 rectangular drift cells with the long side perpendicular to the beam direction. The detector total length along the beam line is 21 cm with an active region of 13 cm. The beam entrance and exit windows are made of 100 μm thick mylar foils. The system is shown in Figure 2.4.

This sub-detector has the purpose of tracking the primaries before their interaction with the target. As a matter of fact, an accurate knowledge of the position and direction of primaries is fundamental to properly apply the Lorentz boost needed for inverse kinematics measurements. Moreover, this information can be used to enhance the accuracy in the reconstruction of beam interaction points inside the target and to reject pre-target fragmentation events. The final goal is to achieve a resolution of 140 μm for position measurements and $\sim$ 1 mrad for angular data. [53]

The BM has been accurately characterized during a dedicated data taking in 2020 at the Trento Proton Therapy center [59]. In this occasion, proton beams of energy ranging from 80 to 220 MeV were used with the aim of evaluating the spatial and angular resolution of the detector. The data acquired show that the BM has a hit detection efficiency close to 93%. The spatial resolution of the drift chamber in the central part of the cell ranges from 150 to 300 μm, which corresponds to an angular resolution of 1.6 to 2.1 mrad for the highest and lowest beam energies, respectively. The detailed description of the analysis performed to extract the BM performance is given in [60]. Since these results have been obtained using proton beams, the BM is expected to work at least at the same level of accuracy with FOOT primaries, which are typically ^{12}C and ^{16}O.

Both the SC and BM detectors have been already employed in several data takings and are now in their final configuration.

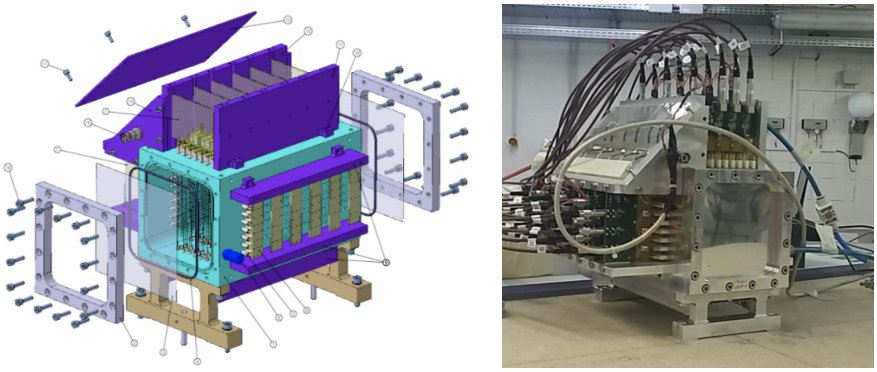

(a) (b)

Figure 2.4: (a) Schematic view of the BM detector (from [53]) and (b) picture of the system during a data acquisition campaign.

2.2.2 Magnetic spectrometer

The magnetic spectrometer of FOOT is the section dedicated to the tracking and momentum determination of the produced nuclear fragments. The spectrometer is placed after the target and consists in three measuring stations made of silicon detectors alternated with two permanent magnets. A picture of the whole mounted section is shown in Figure 2.5. The purpose of this section is to extract the momentum of fragments traveling through the setup by studying how their trajectories bend inside the magnetic field.

The design of the spectrometer has been conceived to match the momentum resolution requested by the experiment while keeping the apparatus as compact as possible. The resolution of p measurements improves as the variation of transverse momentum Δp_T increases. Considering a particle of charge q traveling through a magnetic field B that acts on a region of length L, Δp_T can be calculated as

$$\Delta p_T = q \int_0^L B \mathrm{d}l \tag{2.11}$$

Preliminary feasibility studies using MC simulations led to the configuration shown in Figure 2.6a, where the Z axis represents the beam line. Each of the magnets consists of smaller components of a Nd-Fe-Co alloy placed in an Halbach configuration. This geometry has the advantage of keeping the field outside the spectrometer region as low as possible, while ensuring a nearly uniform magnetic field along transverse x-y planes. [53] As a matter of fact, the field has been measured to be uniform at the percent level up to a distance of 3 cm from the centers of the magnets.

The magnets cover a longitudinal distance of about 30 cm and the modules are $\sim$ 10 cm thick with an internal radius of $\sim$ 3 and 5 cm, respectively. The two magnets are placed at a distance of 5 cm, enough to host the Inner Tracker detector in between, and reach a maximum magnetic field at the center of 1.4 and 0.9 T, respectively. As shown in Figure 2.6b, the magnetic field is directed upwards, i.e. along the positive Y direction. In their final configuration, the FOOT magnets weigh 200-300 kg in total. A robust mechanical support, shown in Figure 2.6c and 2.6d, has also been developed for the whole spectrometer in order to fully exploit the best possible resolution achievable ($\sim$ 10 μm) with the trackers. The magnets and their mechanics have been completed in late 2023 and have been successfully tested and employed in a data taking campaign at the CNAO facility.

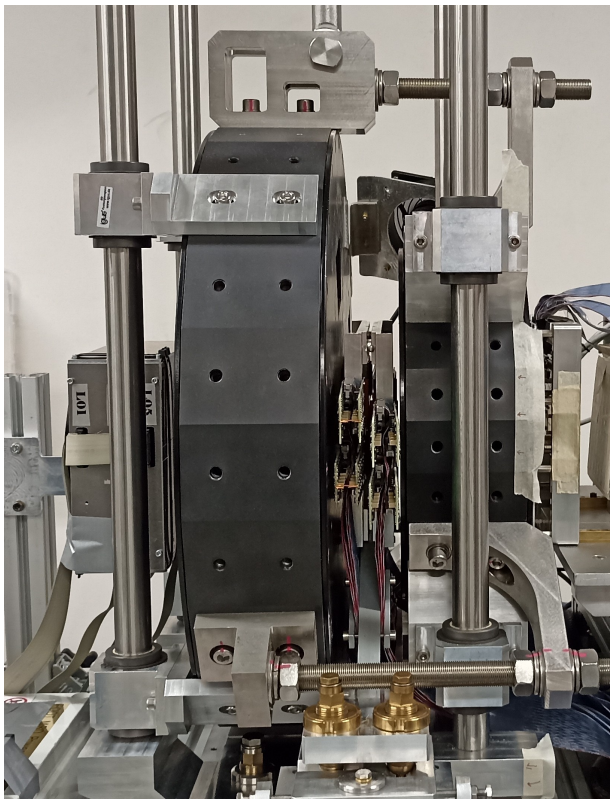

Figure 2.5: Magnetic spectrometer of FOOT during a data acquisition campaign at the CNAO facility. The two permanent magnets are alternated with the three silicon measuring stations: the Vertex (right), the Inner Tracker (center) and the Microstrip Silicon Detector (left).

Vertex and Inner Tracker

The first measuring station of the tracking system is the Vertex (VT) detector. It consists in 4 layers of MIMOSA28 (M28) chips developed by the Strasbourg CNRS PICSEL group. [61] The M28 chips are CMOS Monolithic Active Pixel Sensors (MAPS), which are already being employed in X-ray imaging and charged particle detection. Each of the VT silicon sensors is 50μm thick and is divided in 928(rows) x 960(columns) pixels of 20.7 μm pitch, corresponding to a total active area of 20.22 x 22.71 mm^2. The VT is placed at $\sim$ 0.5 cm from the target and it is organized in two substations at a distance of 10 mm from each other. Each substation is made of two M28 chips at a 2 mm distance. With this setup, the geometrical acceptance of the VT at the farthest sensor from the target is about 40° from the beam axis. [53] The detector is shown in Figure 2.7.

The aim of the VT is to track the particles ejected from the nuclear fragmentation reactions and identify the interaction points of primaries inside the target. Particles passing through the sensors produce a signal inside different pixels and their hit positions on the planes can be reconstructed with a resolution at the level of 5 μm. [62, 63] This guarantees a precision on angular measurements compatible with the needs of the experiment. The VT has already been completed and employed in several data takings.

The second station of the spectrometer is the Inner Tracker (IT), which is placed in the region between the two magnets, at $\sim$ 15-20 cm from the target. The detector is made of a total of 32 M28 chips (the same of the VT) equally distributed in 4 ladders similar to those used in the PLUME project. [64] These components consist of a Kapton

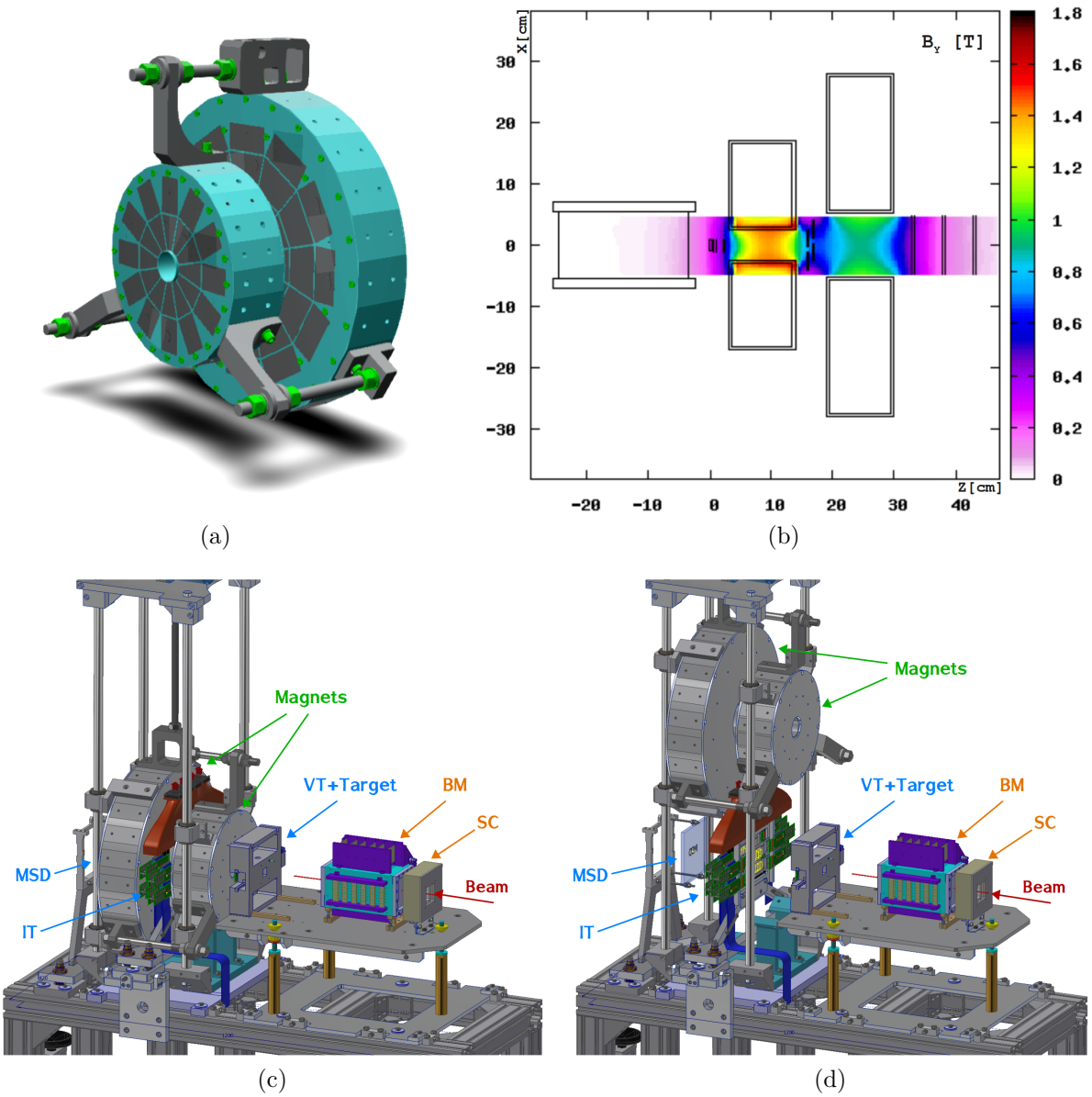

Figure 2.6: (a) Schematic view of the FOOT permanent magnets showing their internal structure and (b) map of the resulting magnetic field in the spectrometer. (c) shows the final design of the mechanical structure holding the upstream region and magnetic spectrometer of FOOT. (d) The support of the magnets has been studied with the possibility to move them out of the beam line for alignment studies.

FPC (Flexible Printed Cable), where the chips are glued, resulting in a total thickness of $\sim$ 100 μm. The maximum transverse distance between two chips is of the order of 30 μm. Moreover, to avoid the superposition of dead areas, the two planes belonging to each ladder are designed to be laterally staggered. As said above, the M28 chips have an active area of 2x2 cm^2, so the IT covers a total transverse area of 8x8 cm^2. [53] The four ladders are hosted in an aluminum frame, as shown in Figure 2.8, which ensures the needed mechanical stability to the detector.

The purpose of the IT is to provide further information on the direction and transverse position of particle tracks along the beam line. The addition of this measuring station in

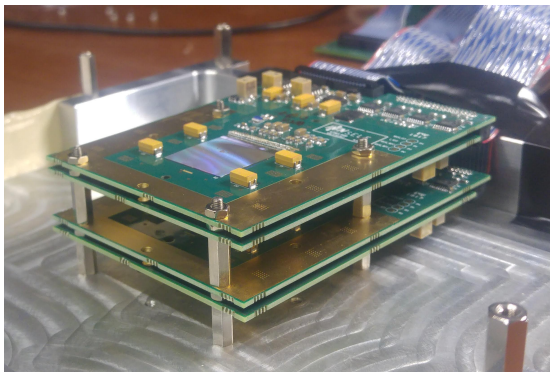

Figure 2.7: Picture of the detecting planes of the Vertex showing the M28 chips.

between the magnets has the purpose to further improve the possible accuracy achievable by the FOOT particle tracking. The detector has been completed and has been tested for the first time at the Beam Test Facility in Frascati, using e^- beams, and at the CNAO facility in late 2023, with protons and ^{12}C ions. The full characterization of the device is currently ongoing.

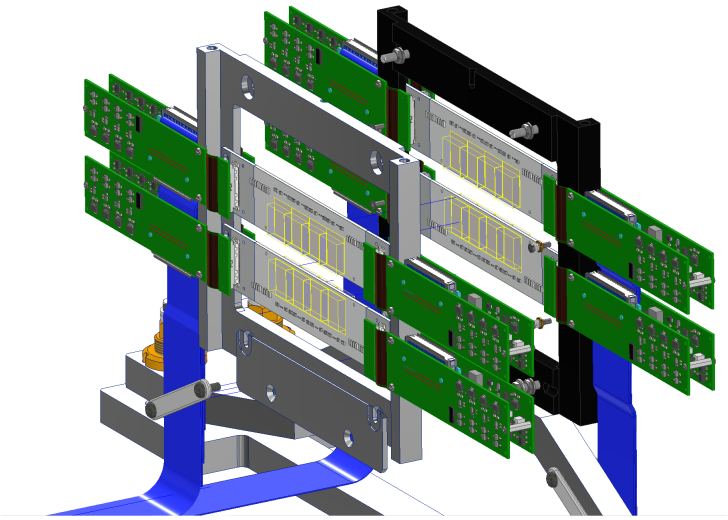

Figure 2.8: Technical drawing of the Inner Tracker in its mechanical structure.

At the moment, the VT and IT are employed in FOOT only for particle tracking. However, the study reported in [65] shows that the M28 chips exhibit a precise correlation between the energy deposited in the active layer and the number of pixels fired. This means that, in principle, these sensors might provide useful information for particle charge identification. In FOOT, Z identification of fragments is performed using other, more precise detectors, but this feature could be exploited as an additional tool to partially recognize *out of target* fragmentation events.

Microstrip Silicon Detector

The third and last station of the FOOT magnetic spectrometer is the Microstrip Silicon Detector (MSD), which is placed at about 30 cm from the target. This component is made of 6 single-sided stripped silicon detectors grouped in 3 stations of alternatively orthogonal layers. The stations are placed at a distance of 4-5 cm from each other, so the total length

of the detector along the beam line is 8-10 cm. Each layer has an active area of 9.6x9.6 cm^2 and is divided in 1920 strips with a width of 50 μm. The MSD analog readout has been conceived with a *floating strip* approach, meaning that only one strip every three is connected to readout electronics, i.e. a channel every 150 μm. This configuration allows for a significant reduction of costs and data stream while maintaining a digital spatial resolution ($\sim$ 43 μm) compatible with the needs of the experiment. In order to reduce the amount of material on the beam line, the total thickness of each silicon layer is limited 150 μm, for a total of 900 μm of silicon on the beam line. [66] Figure 2.9 shows a picture of the system.

The MSD provides the last information on fragment trajectories, fundamental to calculate the momentum of particles and match the tracks with hits in the downstream region of FOOT. Moreover, the detector provides a measurement of the energy released in the silicon sensors, granting a redundant measure of the charge of impinging particles together with that given by the downstream detectors. The MSD detector has been completed and employed in several data takings. The first results obtained in beam tests with proton, ^{12}C and ^{16}O beams have shown that the current configuration of the detector allows for a spatial resolution that ranges from 10 to 35 μm, which is better than the expected performances. [67]

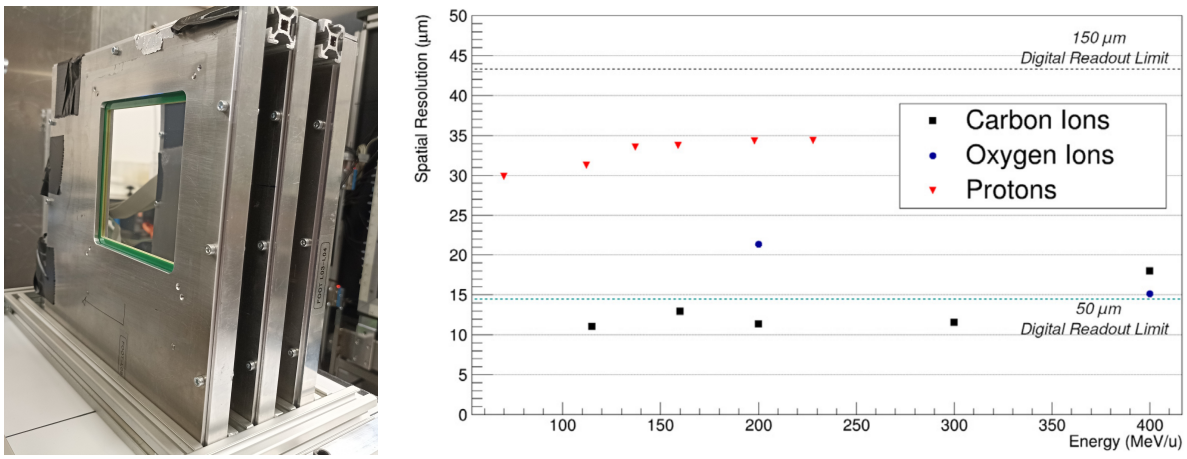

(a) (b)

Figure 2.9: (a) Picture of the MSD detector during a data taking at the HIT facility (Heidelberg, Germany) in 2022 and (b) measured spatial resolution of the detector using ion beams (p, ^{12}C and ^{16}O) at different energies. The plot shows how the *floating strip* analog readout approach chosen provides a spatial resolution compatible with that of a full digital readout of the silicon strips (from [67]).

2.2.3 Downstream region

The downstream region of FOOT is placed at about 1-2 m from the target (depending on the energy of the beam) and is mainly dedicated to the measurement of particle kinematics for charge and mass identification. It is made of two detectors: the TOF-Wall (TW) and a BGO Calorimeter (CALO).

The TW is made of two orthogonal layers of 20 EJ-200 plastic scintillator bars with a transverse section of 44x2 cm^2 and a thickness of 3 mm. The bars are placed horizontally in the front layer (i.e. the first hit by primaries) and vertically in the rear layer, with a total

overlap area of 40x40 cm^2 ($\sim 10^\circ$ angular coverage at 1 m from the target). The resulting 2x2 cm^2 granularity matches that of the downstream BGO crystals in the Calorimeter and keeps the occurrence of multiple fragments hitting the same bar below 1%. Each of the TW bars is wrapped with reflective aluminum tape and the whole detector is covered using black darkening tape to shield it from background light during data acquisition. The collection of scintillation light is performed through 4 3x3 mm^2 MPPC SiPMs with 25 μm microcell pitch placed at each far side of the bars. SiPM signals are acquired at a sampling frequency of 3 GSamples/s. The TW is in its final configuration and it has been already employed in all acquisition campaigns. A picture of the detector is reported in Figure 2.10.

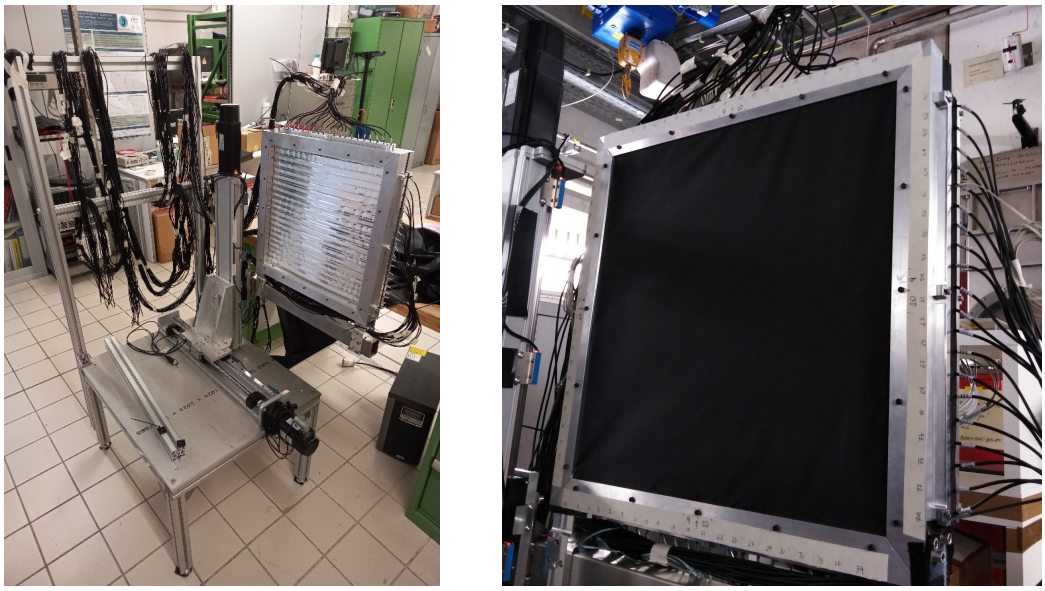

(a) (b)

Figure 2.10: (a) Picture of the TOF-Wall with its mechanical support and (b) detector on the beam line with its shielding from background light.

The TW has the main purpose of performing the charge identification of impinging particles through ΔE and Time-Of-Flight measurements (in combination with the SC). To meet the requirements of the experiment, the TW has been designed to achieve a 4% accuracy for ΔE measurements and 70 ps time resolution for heavy nuclei (C,O) at 200 MeV/u. The bar thickness of 3 mm has been chosen as an optimal trade-off between the requested detector performance and the need to lower as much as possible the probability of secondary fragmentations inside the TW. In previous studies, such as [56] and [68], it has been shown that the TW is already capable to satisfy the requirements of the experiment, even reaching TOF resolution of the order of 50 ps for the heavier ions.

TW data are also important for the global reconstruction of particle tracks. The maximum uncertainty on the hit position is simply given by the granularity of the detector "pixel" (2 x 2 cm^2). However, it has already been shown that the time information given by the signals collected at each side of the bars can be exploited to improve the accuracy on the particle hit position [69].

Since the bending of the trajectory depends on the charge of the fragments (see Equation 2.11), the information obtained from TW is used as a seed for track extrapolation and fitting in the global reconstruction algorithm. Moreover, as it will discussed in detail

in Section 3.3, the reconstruction of particle trajectories in the FOOT setup ultimately provides a measurement of their rigidity p/Z, meaning that the charge measurement is actually crucial to provide a correct evaluation of the momentum p.

The last component of the FOOT setup is a Calorimeter (CALO), which is made of about 320 BGO (Bismuth Germanate) crystals arranged in a geometry pointing to the target. The BGO crystals are organized in 3x3 modules encased in 3D-printed plastic supports, designed to hold the crystals from the back and leave only air and BGO in the first 12 cm of the detector. Each of the BGO crystals is shaped as a truncated pyramid with ∼2x2 cm^2 and ∼3x3 cm^2 surfaces and a total length of 24 cm. The light produced in the BGO is collected at the downstream side of each crystal by a 5x5 matrix of SiPMs with 15 μm microcell pitch. The signals generated in CALO crystals are acquired at 1 GSamples/s. The CALO is placed right after the TW and has the same angular acceptance.

The purpose of the CALO is to stop all the impinging particles and measure their kinetic energy, which is used for mass identification. To match the resolution needed by FOOT, the CALO should achieve a resolution of the order of 1-2% on energy measurements. The choice of BGO for the Calorimeter was dictated by its high density and light yield. Since FOOT is built to work at relatively low beam rates (< 10-20 kHz), the slow time response and recovery of the BGO (∼ 300 ns decay time) should not affect the quality of the collected data. One of the possible drawbacks of this kind of detector is the non negligible probability of nuclear interaction between the fragments and the crystal with significant production of secondary neutrons, which can then escape the CALO. The high neutron interaction cross section of BGO partially contains such effect, but a possible underestimation of the measured kinetic energy has to be taken into account during mass evaluation. Even if neutrons produced in the CALO can reach other detectors, such particles do not generate a significant background since they can be removed during charge identification in the TW (see Section 3.2) or particle track reconstruction (see Section 3.3).

The CALO is currently close to completion, with the final design expected to be ready and fully functional for the 2024 data acquisition campaigns. Preliminary beam tests have shown that the detector is capable of reaching the wanted performance, with energy resolutions lower than 1% for ^{16}O ions at 200-400 MeV/u. [70]

2.2.4 Trigger and Data AcQuisition (TDAQ)

The data acquired by each detector of the Electronic Setup is handled by the FOOT Trigger and Data AcQuisition (TDAQ) system. The FOOT TDAQ is based on the one used in the ATLAS experiment at LHC (Large Hadron Collider, CERN) [71] and it is maintained and developed by the University and INFN section of Bologna.

The TDAQ architecture is summarized in Figure 2.12. It is a flexible, hierarchical and distributed system based on Linux PCs, detector readout systems, VME crates and boards connected via standard communication links like USB, Ethernet and optical fibers. The Storage PC, which is kept in the experimental room during data takings, manages the whole acquisition. It is equipped with two network interfaces, one for internal communication with the other components of the TDAQ and one going to the outside network. The different parts of the internal network are linked to each other via an Ethernet switch with 1 GbE and 10 GbE ports. The two fastest ports are reserved for the Storage PC and the NAS (Network Attached Storage). The switch collects all the data coming from

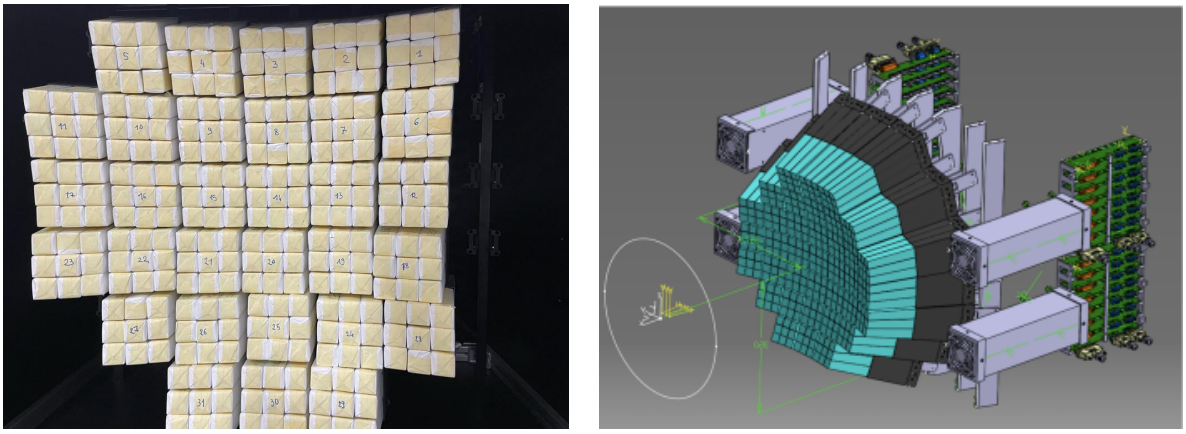

(a) (b)

Figure 2.11: (a) Picture of the FOOT calorimeter assembly during a data taking at CNAO in 2023, showing the completed 3x3 modules, and (b) sketch of the final geometry.

detector readouts: 20 DE10nano or DE10 Terasic boards for the tracking system and the WaveDAQ [72] for the SC, TW and CALO detectors. Moreover, an optical fiber link connects the Storage PC to a VME crate hosting the V2495 trigger board and all the readout electronics of the BM.

The main Ethernet switch is also connected to two additional PCs located in the control room during data takings. The Control PC is used to connect to the Storage PC and manage the acquisition while the Monitor PC is reserved to data monitoring with online and quasi-online software processing tools. A detailed description of the TDAQ system can be found in [73].

Since only a fraction of the events acquired by FOOT undergo fragmentation reactions, the TDAQ has been equipped with a specific trigger logic to enhance the data sets. FOOT data takings are carried out using several trigger algorithms, all handled by the WaveDAQ (see Section 3.1) and distributed to all the detectors via the V2495 board:

- The *Minimum Bias (MB) trigger*, which is issued whenever a primary particle crosses the SC. To limit as much as possible the number of spurious triggers from electronic noise, the MB trigger implements a majority logic, meaning that it checks that at least a minimum number of SC channels give a signal over a pre-defined amplitude threshold. The normal MB logic of FOOT asks for a majority of 5 or 6 SC channels, depending on the impinging beam ion and energy. An additional feature of the MB trigger is the implementation of a *clipping* logic, which accepts a trigger as valid only if no other trigger signal was issued in a certain preceding time window. In the case of FOOT, two consecutive MB triggers need to be separated by at least 10 μs.

- The *Fragmentation trigger*, which asks for both the MB condition and the absence of a VETO signal in the TW. The VETO is generated whenever two of the central bars of the TW (one per layer) register a pulse height compatible with the passage of a primary through the setup. In such way, it is possible to remove the events that do not contain a fragmentation reaction. Considering that only a few % of primaries are expected to undergo a nuclear interaction in the target, the usage of this trigger logic can significantly enhance the number of fragmentation events observed. A

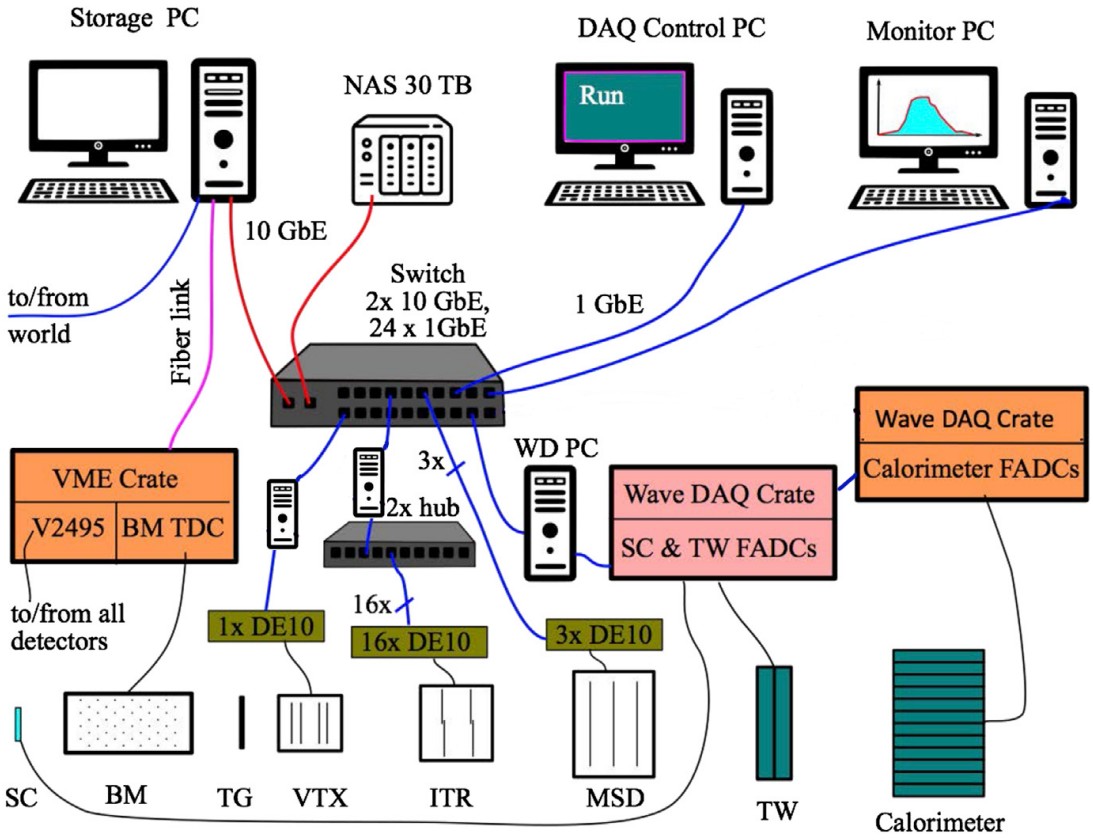

Figure 2.12: FOOT TDAQ infrastructure

scheme of the fragmentation trigger logic is reported in Figure 2.13. [74] The area where the fragmentation trigger logic looks for a possible VETO signal in the TW considers the three central bars of each layer, i.e. 9 possible crossings in a 6x6 cm^2 surface.
The main advantage of this type of trigger is that, contrary to a simple topological fragmentation trigger, it allows to also measure fragments impinging at the center of the TW. This enables the possibility to accurately extract particle yields also at low emission angles, which is a crucial characteristic since projectile fragments are expected to be emitted mainly in the forward direction. At the same time, the chosen VETO logic is solely based on the energy loss in the central portion of the TW. This has two important implications: on the one side, the thresholds for the rejection of primaries have to be set each time the beam is changed. However, this does not pose a problem since they can be calculated during the acquisition with the MB trigger. On the other hand, as shown in Figure 2.1a, the detectable fragments are expected to have a velocity very close to that of the primary particle, especially in the case of heavier fragments. In this situation the fragmentation trigger can not distinguish between primaries (e.g. ^{16}O) and fragments (e.g. ^{15}O) with the same charge, leading to a loss of selection efficiency for these specific particles.

- The *TWalone* and *CALOalone* triggers, which are used mainly during data acquisition runs dedicated to the calibration of TW and CALO, respectively. The first one consists in a logic OR of all the 40 TW bars, meaning that a trigger signal is created each time a bar is hit by a particle. This condition is satisfied when both of the corresponding channels register a pulse higher than the Zero-Suppression threshold.

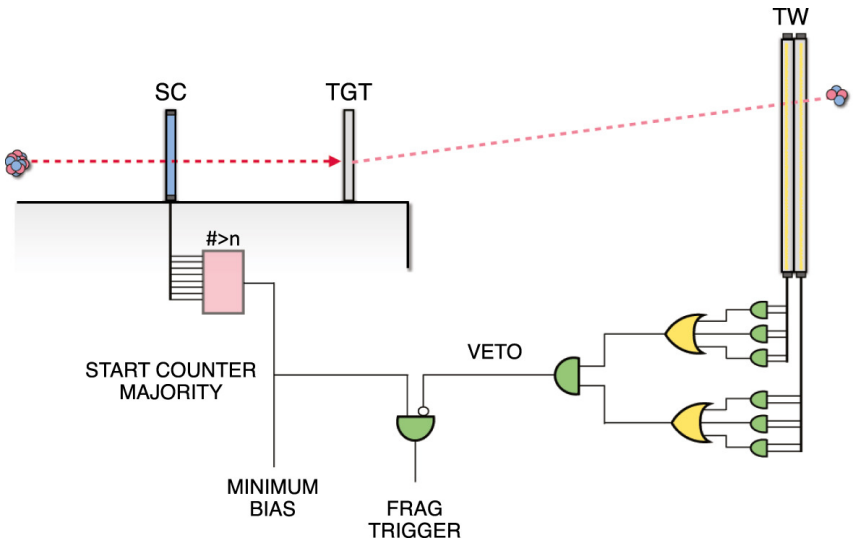

Figure 2.13: Logical scheme of the FOOT Minimum Bias and fragmentation triggers, highlighting also the logical scheme for the generation of the VETO signal in the TW (from [74]).

The latter trigger algorithm consists in a simple logic OR of all the channels connected to the CALO and, thus, creates a trigger every time there is at least one CALO crystal pulse above the Zero-Suppression.

The TDAQ has been designed to withstand the maximum acquisition rate achievable by the FOOT setup with the MB trigger, which is only dictated by the incoming beam rate and the dead time of the slowest detector. In the case of FOOT, the VT acquires three consecutive frames with a readout time of 185 μs each, meaning a maximum theoretical acquisition rate of 1.8 kHz. However, to reduce as much as possible pile-up effects on M28 chips, the TDAQ maximum acquisition rate is normally limited at 1 kHz. For this reason, in stable running conditions, the beam rate used for data acquisitions is usually of the order of 5-10 kHz at maximum. Considering an accelerator duty cycle of 30%, in stable running conditions, the FOOT experiment is expected to collect a maximum of 26 millions events per day of acquisition.

2.3 Emulsion spectrometer

The Emulsion Spectrometer of FOOT has been conceived with the aim of focusing on the characterization of low Z (≤ 3) fragments produced in fragmentation reactions. This setup has a much higher angular acceptance with respect to the Electronic Setup, going up to 70° from the primary direction, compatible with the wider emission angles expected for lighter fragments. The choice for a setup based on nuclear emulsion films comes from the very high spatial resolution of these devices in ionizing particle tracking, reaching up to sub-micrometric scales. Nuclear emulsions are made of a gelatine material filled with tiny AgBr crystals. These crystals are sensitized by the passage of ionizing particles and produce a latent image along their trajectories, which can then be enhanced by means of a chemical process and scanned via optical microscopes.

Systems based on nuclear emulsions also make it possible to create compact setups where detecting layers are interleaved with target material, which is perfectly compliant

with the requirement of a portable setup. Moreover, the advancements in automated scanning system techniques allow for a fast and precise analysis of huge data sets. [53, 75]

The nuclear emulsion films used in FOOT are produced by the Nagoya University (Japan) and Slavich Company (Russia). Each of the films consist in two 70 μm thick emulsion layers deposited on the sides of a 210 μm plastic base. The sensitivity of the films employed in FOOT corresponds to about 30 AgBr grains over a track length of 100 μm for a minimum ionizing particle (MIP). [76]

The FOOT Emulsion Spectrometer setup is made of two main components: the upstream region, which consists of the same Start Counter and Beam Monitor detectors of the Electronic Setup, and an Emulsion Cloud Chamber (ECC). In this setup, the SC and BM are used only to monitor the beam flux to avoid spatial pile-up of primaries. The actual cross section measurements are performed here with the ECC, sketched in Figure 2.14. This component is divided in three main sections with complementary purposes.

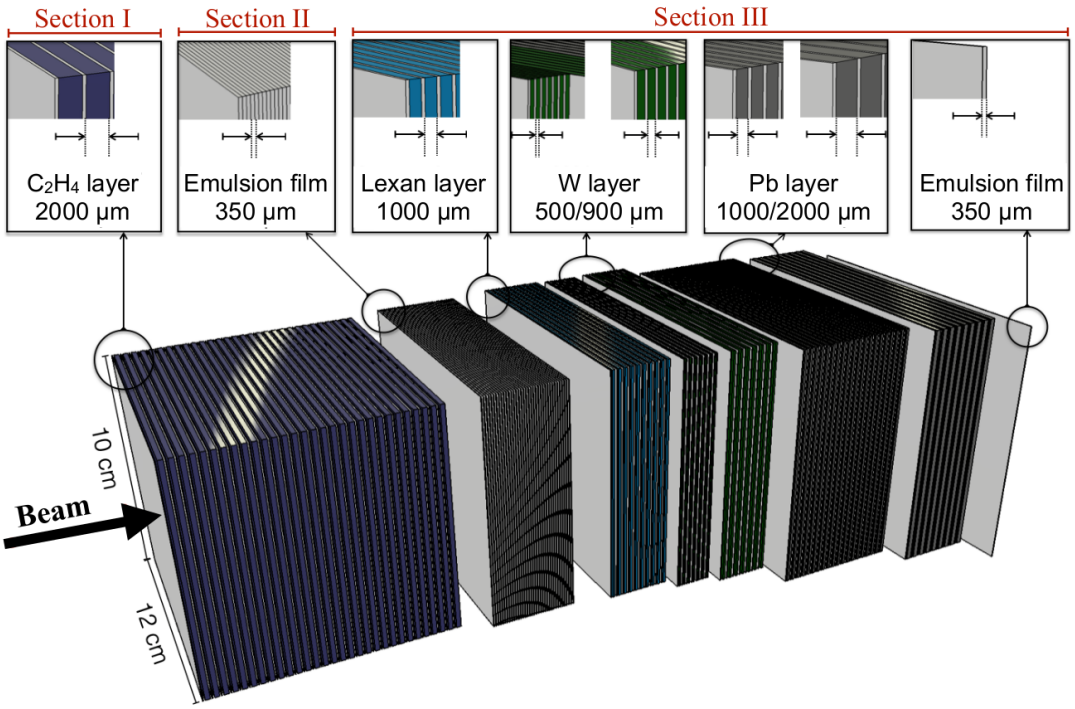

Figure 2.14: Schematic view of the FOOT Emulsion Cloud Chamber setup.

The first section is made of 30 nuclear emulsion films alternated with thin ($\sim$ 1-2 mm) layers of target material, i.e. polyethylene or carbon. This section is devoted to the identification of interaction points between primaries and target. The events in which a fragmentation reaction occurs in this portion of the spectrometer are selected for further analysis and used in cross section evaluation. The total length of this section has been chosen so that the Bragg peak of primary particles is completely included in it, meaning that only nuclear fragments can reach the downstream sections of the ECC. Moreover, the depth at which the fragmentation occurs makes it also possible to accurately reconstruct the energy of the primary at the moment of the interaction. This feature allows, in principle, to perform cross section measurements for different energies of the impinging beam with a single exposure.

The second section of the ECC is entirely made of nuclear emulsion layers and is dedicated to charge identification of fragments. The 36 emulsion films in this section

are divided into 9 cells of 4 layers. The four films of each cell are thermally treated at different temperatures to enhance their sensitivity to ionization, extending their dynamic range and enabling the possibility to discriminate particles with different charge.

The third and last section of the ECC is made of 55 emulsion films interleaved with layers of lexan and high density materials, such as tungsten and lead. This section is dedicated to the measurement of fragment momentum, which can be extracted from particle range and multiple Coulomb scattering. [76]

The Emulsion Spectrometer has been employed in several experimental campaigns since 2019. A picture of the whole setup on the beam line at the GSI facility in 2019 is shown in Figure 2.15. The data acquired in this occasion were used to perform the first assessment of charge identification capabilities with the ECC. The work reported in [76] shows that, using a mix of simple cuts and Principal Component Analysis techniques [77], the ECC is able to correctly identify the charge of lighter fragments emitted in fragmentation reactions inside the detector.

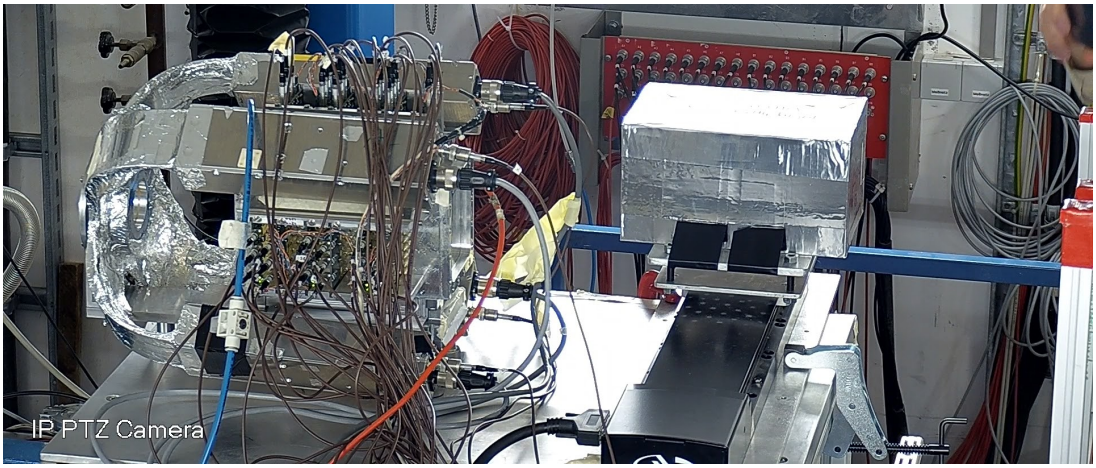

Figure 2.15: Picture of the ECC setup during a data taking at GSI in 2019.

Since the core of the work presented in this thesis is devoted to the reconstruction and data analysis of the Electronic Setup of FOOT, the Emulsion Spectrometer will not be further discussed in the following sections.

Chapter 3

Data processing and track reconstruction

The processing of all data acquired by FOOT is carried out through the main software of the Collaboration, which is called SHOE (Software for Hadrontherapy Optimization Experiment). SHOE is an object-oriented, flexible framework based on C++ and ROOT libraries, partially inherited from the FIRST experiment. The software takes care of the whole data processing, from raw data decoding of all sub-detectors to particle identification and tracking, up to the cross section evaluation.

The SHOE framework has also been conceived to generate all the input files needed to perform Monte Carlo simulations in FLUKA [78, 52] and Geant4 [79] for all the FOOT data acquisition campaigns. Custom user routines have also been implemented to decode the FLUKA scoring output and translate it in the ROOT format used for decoded data structures, so that the same reconstruction software can be used for both raw and simulated data sets. When working with MC generated files, SHOE also implements all the smearing of measured quantities, based on the evaluated experimental resolution of each detector in the setup.

In parallel with SHOE, the FOOT Collaboration has developed a set of tools dedicated to the online monitoring of data during acquisition campaigns, both directly interfaced with the TDAQ (Gnam) and stand-alone (SLIPPER). A scheme of the whole framework is reported in Figure 3.1.

During my thesis work, I have contributed to different aspects of the FOOT data processing and reconstruction, which will be discussed in the following sections.

3.1 WaveDAQ signal processing

One of the processing steps I mainly contributed to is the analysis of signals acquired by the WaveDAQ system. As stated in the previous chapters, this component of the FOOT TDAQ takes care of acquiring the signals of SC, TW and CALO. The WaveDAQ employs a set of custom acquisition boards called WaveDREAMs, based on the DRS4 chips developed at PSI (Paul Scherrer Institut, Villigen) for the MEG II experiment. The DRS4 are flexible systems capable of sampling signals with an acquisition rate ranging from 0.5 to 5 GSamples/s. Each WaveDREAM board hosts 2 DRS4 chips for a total of 16 acquisition channels and 2 internal 80 MHz clocks, one per DRS4. The clock signals are sampled and saved to the output in order to perform an accurate offline phase synchronization of all the channels. This feature makes it possible to limit the time jitter

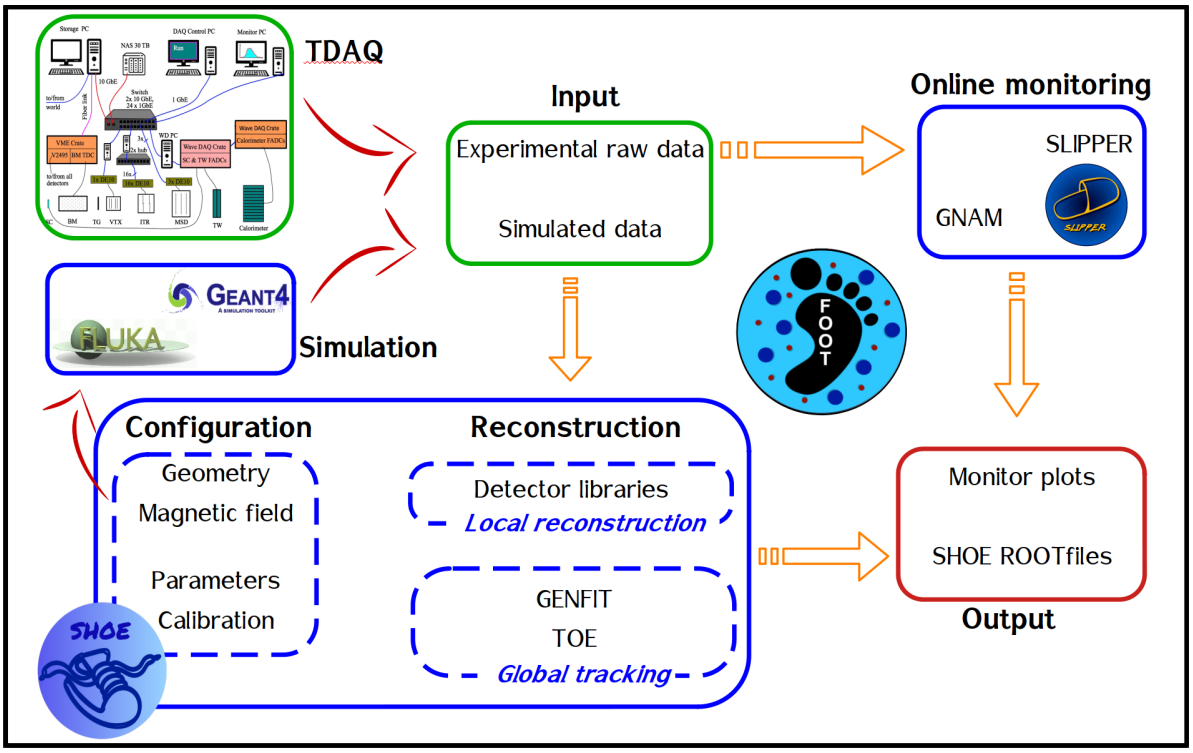

Figure 3.1: Scheme of the FOOT data acquisition, simulation and reconstruction framework.

directly introduced by the WaveDAQ to a maximum of 5 ps [72].

The WaveDAQ channels are equipped with programmable front-end gain (0.5-100), Zero Suppression threshold and Pole Zero Cancellation circuits for signal shaping. The system is also capable of supplying the bias voltage needed for the powering of all the readout SiPMs of the connected detectors. As it is operated in the FOOT experiment, each of the WaveDAQ channels acquires 1024 samples of its signal per trigger, meaning that the acquisition window of each channel is inversely proportional to the chosen sampling rate. Since BGO crystals have a much slower response compared to plastic scintillators, SC and TW channels are acquired at 3 GSamples/s (330 ns acquisition window) while CALO channels are acquired at 1 GSamples/s (1 μs window). In the final configuration of FOOT, the WaveDAQ will handle a total of about 420 signal channels distributed over 28 WaveDREAM boards.

3.1.1 Online signal processing

During data acquisition, the WaveDAQ signals are continuously monitored through the SLIPPER (Software for Live Interactive Plotting and Partial Event Reconstruction) software, an online processing tool that performs the evaluation of signal characteristics. SLIPPER is an object-oriented framework mainly based on C++ and ROOT classes. The software also includes a set of Python and Bash scripts that are used to handle the data processing flow. Python scripts are mainly used to implement multi-thread processing and online data monitoring, while the Bash scripts are used to interface the software with the high-throughput resources of CNAF Tier1 data centre. [80]

SLIPPER extracts all the relevant information to control the correct functioning of the SC, TW and CALO detectors while also monitoring the rate of impinging primaries

and the functioning of the fragmentation trigger. The routines used in SLIPPER for signal processing are the same employed in SHOE and will be discussed in the following sections. The main difference with SHOE is that this software has been designed to perform such operations in the fastest and most optimized way possible, removing also any processing step that is not strictly necessary for online monitoring. This allows to have a reliable feedback on data quality and check the performance and alignment of the FOOT scintillators and trigger in real time. At this stage, the software is capable of processing $\sim$ 3.5 kEvents/s, much faster than the FOOT TDAQ performances with the trackers connected, which means that each event acquired is also processed in real time and included in the monitoring plots.

The SLIPPER framework also implements a custom Graphical User Interface (GUI), developed in ROOT, which contains all the data monitoring plots for each of the detectors acquired with the WaveDAQ. A set of control graphs dedicated to the functioning of the different trigger algorithms employed by FOOT is also included in the software. The GUI serves as a useful tool during experimental campaigns, creating a much more user-friendly environment for users to monitor the quality of acquired data and spot any possible issue with the detectors in a short amount of time.

3.1.2 Start Counter

The SC detector is used to calculate the start time of each event and reject pile-up events in the upstream region of FOOT. An SC event consists of 8 signal channels and one reference clock, all sampled at 3 GSPS. The typical shape of the signal generated in one SC channel by the passage a primary particle is shown in Figure 3.2.

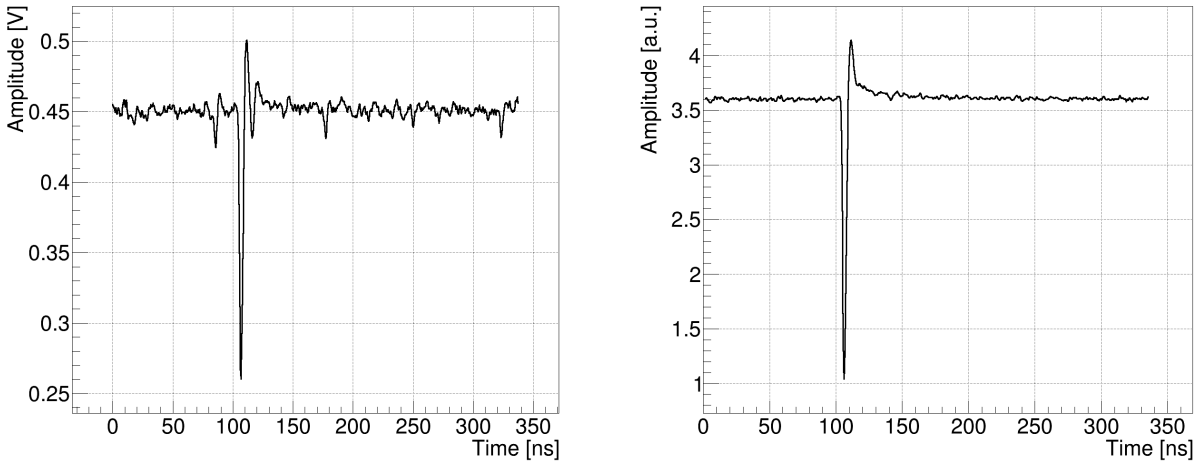

(a) (b)

Figure 3.2: (a) Typical shape of a SC raw signal as seen by the WaveDAQ and (b) example of the summed signal of all the 8 channels.

The extraction of the start time of the event is performed by taking all the 8 signal channels and summing them together through a "*bin-per-bin*" linear interpolation and thus obtaining a global waveform. This sum operation is used to combine all the information coming from each channel, while also strongly improving the signal to noise ratio, as it can be seen from Figure 3.2b.

After this sum, a digital Constant Fraction Discriminator (CFD) algorithm is applied to the total waveform to calculate the start time of each event: the time information of the signal is associated with the moment when the waveform reaches a certain fraction of its maximum amplitude. In the case of the SC, the threshold is set at the 20% of the signal amplitude from the baseline. The rationale for using a CFD algorithm is its capability to limit the effects of signal amplitude variations on the extracted time. The accuracy of the CFD strongly depends on the requirement that the shape, and thus the rise time, of the analyzed signals is constant except for a scaling factor. Figure 3.3 shows an example of how the algorithm works on a typical SC signal. Here, the baseline, CFD threshold and start time of the event are highlighted.

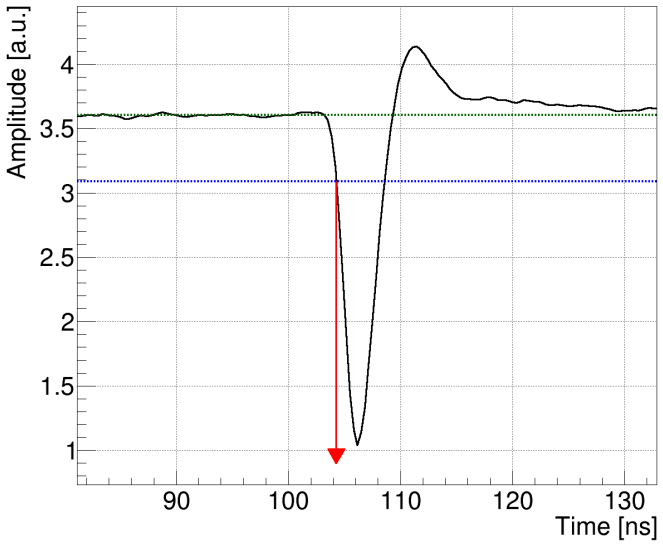

Figure 3.3: Constant Fraction Discriminator algorithm application to a SC summed signal. The green line represents the baseline of the pulse, while the blue one shows the 20% threshold of the CFD. The red arrow highlights the final time associated with the signal.

As already mentioned in Section 2.2.1, one of the purposes of the SC is the characterization of the primary beam. This also includes the identification of pile-up events. In the case of FOOT, an event is defined as a pile-up whenever more than one primary travels through the setup in the same trigger. Considering that the SC acquisition window is of the order of 250-350 ns (depending on the chosen sampling rate) and the typical working beam rate of FOOT is 1-10 kHz, the number of pile-up events is expected to be quite low. However, since fragmentation reactions occur only in a small fraction of the acquired events, it is crucial to lower as much as possible the contribution of any background component.

To remove pile-up events, the processing of SC channels also includes a pile-up rejection algorithm, which was designed following the Pulse Shape Analysis techniques used by the n_TOF Collaboration. The working principle is a simplified version of the one applied for pulse recognition in [81] and it is shown in Figure 3.4. The derivative a'_i of the summed SC signal is estimated at each time bin t_i as the moving incremental ratio

$$a'_i = \frac{a_{i+n} - a_{i-n}}{t_{i+n} - t_{i-n}} \tag{3.1}$$

where a_i and t_i are the amplitude and time values of the signal at the $i-$th bin, respectively. Since the optimal width for derivation is usually of the order of the signal rise time,

in the case of the SC n has been chosen to be equal to 5, corresponding to a time window of $\pm 1.6 - 1.7$ ns at 3 GSamples/s. After this step, two thresholds are applied to the derivative signal, equal to $\pm$ 30% of its peak-to-peak amplitude, and the routine counts how many times the signal crosses such thresholds. For a single primary crossing the SC, i.e. a clean event, the derivative signal is expected to cross these thresholds exactly 4 times. Any event showing a different number of crossings is flagged as a possible pile-up. An example of how the procedure works on events with and without pile-up is reported in Figure 3.4.

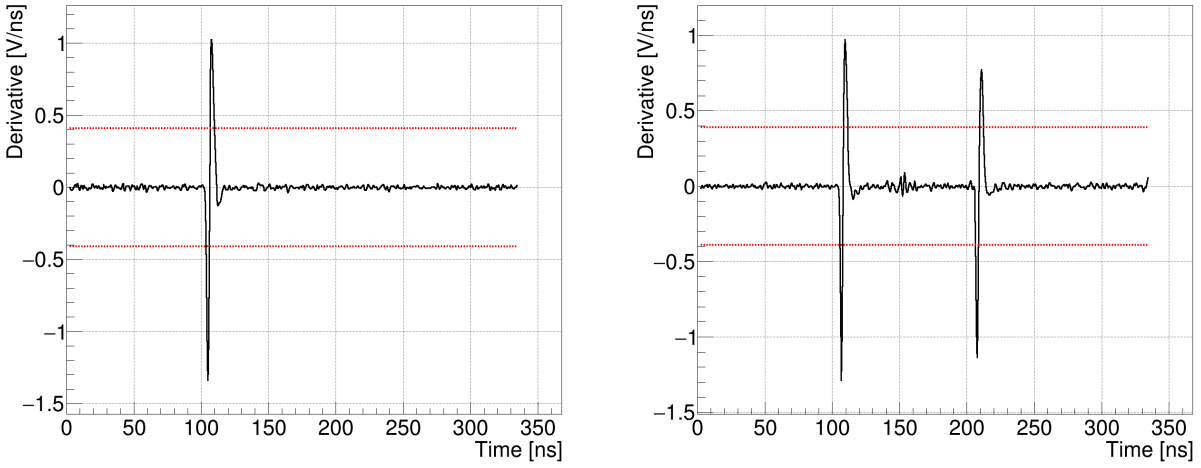

(a) 4 crossings: no pile-up

(b) 8 crossings: pile-up

Figure 3.4: Working principle of the pile-up rejection algorithm, with the red lines showing the associated thresholds: (a) reports the derivative calculated with Equation 3.1 of the signal in Figure 3.2b. Here, the waveform crosses the set thresholds 4 times, which is the signature of an event with no pile-up. (b) Example of an event with two primaries in the SC which is flagged as pile-up (8 crossings) by the algorithm.

The accuracy of this procedure can be appreciated studying the energy deposited in the SC in each event. This is evaluated as the integral of the summed SC waveform, taken considering only the part of the signal that is below the level of the baseline. The choice of cutting the component above the baseline was made in order to remove the overshoot (see Figure 3.2) introduced by the pole-zero cancellation circuit in the readout electronics. Figure 3.5 shows the integral of SC signals for a sample of ^{16}O ions at 400 MeV/u. As it can be seen, in Figure 3.5a the distribution shows two peaks, which are caused by the passage of either one or two primaries in the time acquisition window of the SC. Figure 3.5b shows the same energy loss distribution after removing all the events flagged as possible pile-up by the described algorithm. Here, the second peak is no longer present and the residual tail of the distribution is compatible with the stochastic variations of energy loss in the SC.

The main quantities monitored for the SC during data acquisitions are the beam and acquisition rates, as well as the percentage of events which are flagged as possible pile-ups. Moreover, the time information is used to check TOF performances in the TW.

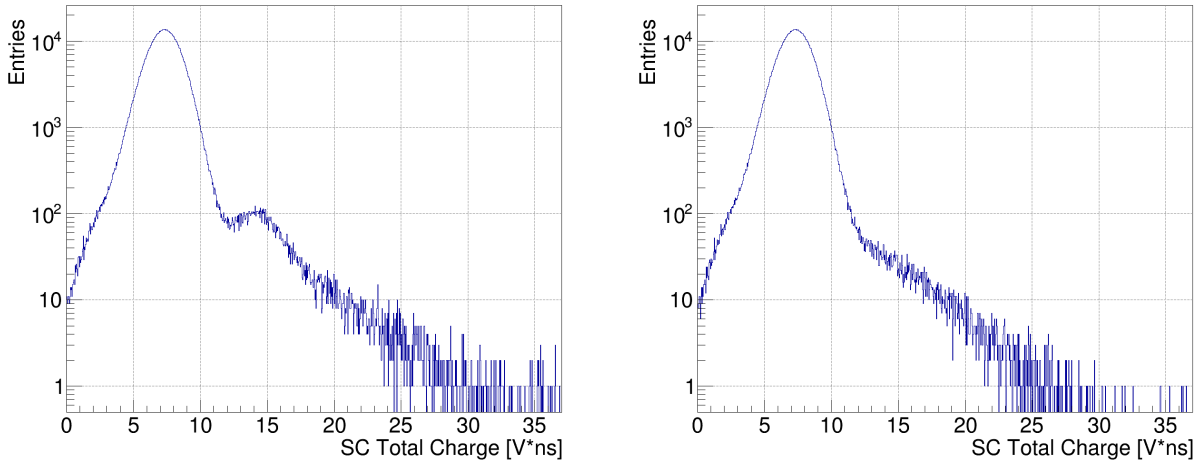

(a) All events (b) Pile-up cut

Figure 3.5: Raw energy deposition of primary particles in the SC detector evaluated as integral of the acquired signals: distribution (a) before and (b) after the cut of pile-up events.

3.1.3 TOF-Wall

The aim of the TW is to measure the energy loss ΔE and Time-Of-Flight TOF of the nuclear fragments, which are fundamental to determine their charge and mass. Thus, the most relevant information to be extracted from TW signals is related to the time of arrival and total energy deposition in the scintillator bars. To achieve this goal, the TW acquires signals at both ends (A/B) of each of its 40 bars for a total of 80 WaveDAQ channels. The information on raw time $T_{A/B}$ and collected charge $Q_{A/B}$ at both ends is then combined to obtain information on the particle raw Time-Of-Flight TOF_{raw} and energy deposition Q_{raw}

$$T_{bar} = \frac{T_A + T_B}{2} \qquad \mathrm{TOF}_{raw} = T_{bar} - T_{SC} \tag{3.2}$$

$$Q_{raw} = \sqrt{Q_A \cdot Q_B} \tag{3.3}$$

where T_{SC} is the start time of the event measured by the SC. The rationale for Equation 3.3 is the exponential attenuation of scintillation light propagating from the point of interaction in the TW bar to the SiPMs at the sides. An example of a typical TW signal is reported in Figure 3.6.

The time information of each TW signal is extracted via a modified implementation of the CFD algorithm. Particles can interact with TW bars in any position along the transverse plane. The light produced in the interaction has to travel to each end of the 44 cm long bar before being collected by the TW SiPMs, passing through a significant amount of material. As a consequence, the rise time of the signals obtained in the TW shows a non-negligible dependence on the impact position of the particle along the scintillator bar, as shown in Figure 3.7a. This ultimately results in a noticeable *time walk* on the standard CFD algorithm output which does not affect resolution but lowers the accuracy on time measurements. An example of this effect is shown in the results of Figure 3.7b, obtained with the same primary beam shot in different positions of a TW bar. Here, it can be noticed that the raw TOF measured at the center of a TW bar can be significantly

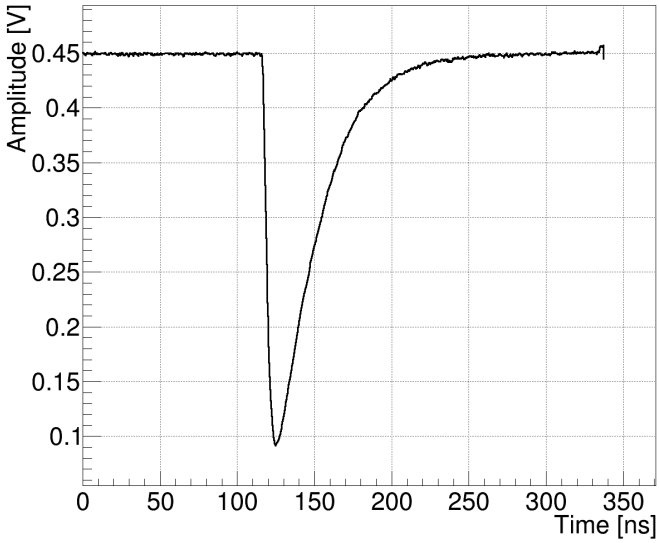

Figure 3.6: Example of the signal acquired by one TW channel as seen by the WaveDAQ.

higher than that obtained at the sides of the bar, even more than the TOF resolution of the system (shown by the error bars).

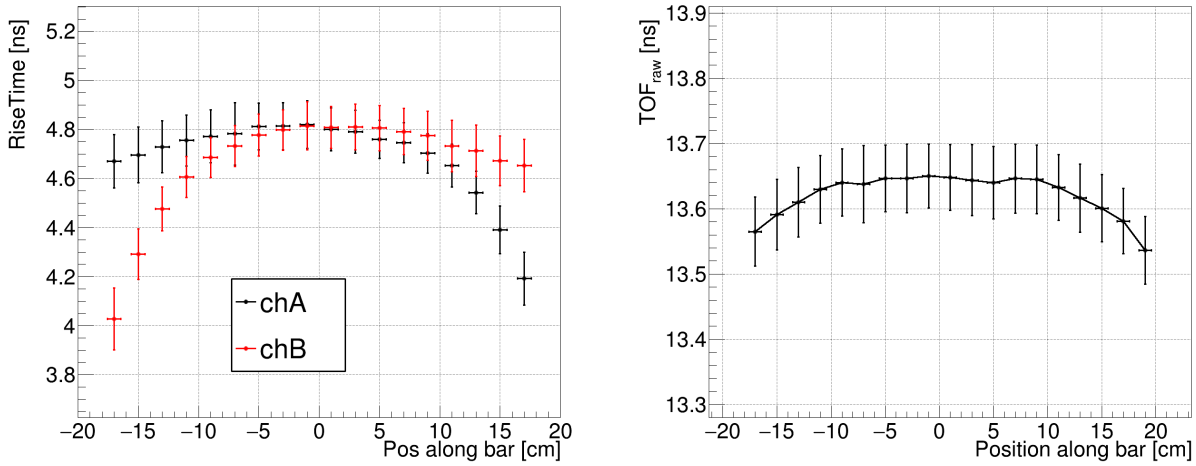

(a) (b)

Figure 3.7: (a) 10-90% rise time of the signals acquired at each end (A/B) of a TW bar as a function of the particle hit position. The rise time is significantly shorter when the particle crosses the bar close to the channel readout. (b) Raw TOF measured in different positions of a TW bar with the 400 MeV/u ^{16}O beam using the standard CFD algorithm described in Section 3.1.2. The error bars reported on the y-axis show the TOF resolution (standard deviation) of the system, with values close to 50 ps in all positions. The visible trend in the absolute TOF values is given by the time-walk of the CFD.

Another important and related aspect is that the difference between the signal arrival time at the two sides of a TW bar should be linked to the particle hit position through a linear relation. However, the time walk introduced by rise time variations has been observed to be relevant enough to spoil this expected linearity. To limit as much as possible the influence of this effect, the CFD algorithm for TW channels has been slightly modified.

An example of the routine actually used for signal time evaluation is shown in Figure 3.8a. The standard CFD algorithm (as shown in Section 3.1.2) is used only to find where the signal crosses the threshold, set at 30% for TW channels. Then, the tangent to the signal is computed at the crossing point and the start time of the signal is evaluated as the intercept of such tangent at the signal baseline. The TOF_{raw} obtained with this method as a function of the hit position is shown in Figure 3.8b, using the same dataset of Figure 3.7b. As it can be easily seen, the dependency with the particle hit position is strongly reduced with respect to the previous situation and is now compatible with the resolution of the system (~ 50 ps).

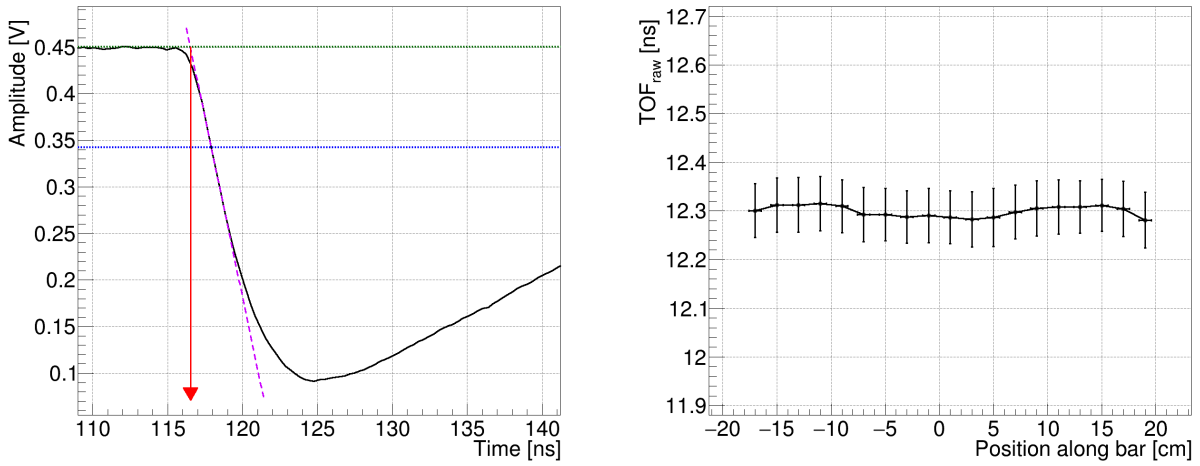

(a) TW modified CFD

(b) New TOF_{raw}

Figure 3.8: (a) Visualization of the CFD method employed to extract the time information from the TW signal in Figure 3.6. The green line is the baseline of the signal, the blue one represents the 30% threshold and the purple one is the tangent to the signal rising edge at said threshold. The extracted time value is highlighted by the red arrow. (b) TOF_{raw} in a TW bar as a function of the hit position calculated with the corrected CFD for the same dataset of Figure 3.7b. The lowering of the absolute TOF values is given by the different CFD applied, which anticipates the time measured by the TW with respect to the standard CFD.

The uniformity shown in Figure 3.8b for TOF_{raw} also implies that the time measured by each of the channels depends linearly on the particle hit position along the bar. This means that the time information at the ends of each bar can be used to reconstruct the hit position of an impinging particle. In particular, considering a reference axis going from channel B to channel A of the bar, the hit position x can be calculated as

$$x = \delta x - \frac{v_l(T_A - T_B)}{2} \tag{3.4}$$

where v_l is the speed of light propagation inside the scintillator bar and δx is an offset given by the cables connecting the channels to the WaveDAQ. These two parameters are different for each bar and thus have to be calibrated. Figure 3.9a shows an example of the calibration curve obtained for a single TW bar. The position reported on the y axis has been calculated using the nominal crossing with the bar hit on the other TW layer. As expected, the nominal position is linear with the time difference inside the experimental uncertainties. Figure 3.9b shows the hit position of particles reconstructed

with Equation 3.4 for a complete scan of the detector using ^{12}C ions at 200 MeV/u. The scan was carried out shooting the particles in the same spot while continuously moving the detector from remote. The visible pattern highlights the beam spills and overall duty cycle of the accelerator, showing the reliability of the applied technique.

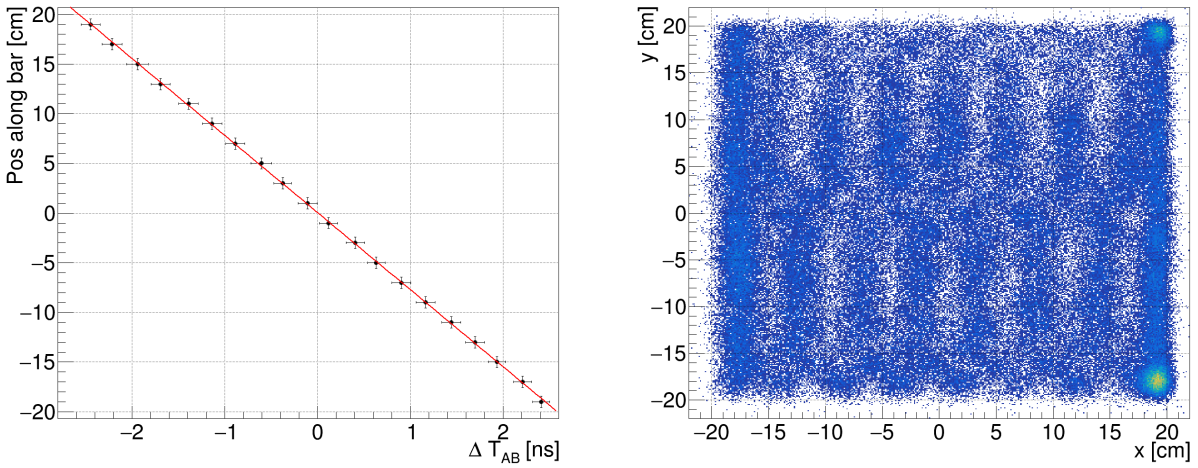

(a) (b)

Figure 3.9: (a) Example of the position calibration curve for a single TW bar, showing the linearity between the hit position and the channel time difference. (b) Reconstructed hit positions for a complete scan of the detector made with ^{12}C ions at 200 MeV/u. The x-y coordinates are reported in the local reference frame of the TW, where the detector spans in the [-20, 20] range in both directions.

For what concerns energy deposition in the TW bars, the collected charge $Q_{A/B}$ in each channel is evaluated from the integral of the corresponding waveform, calculated from the baseline. The total raw energy deposition is then extracted from Equation 3.3. An example of the raw energy deposition spectrum obtained in a TW bar is shown in Figure 3.10. The data shown here refer to an acquisition with ^{16}O ions at 400 MeV/u impinging on a carbon target. The rightmost peak is the one generated by primary ions while all the other peaks are given by lower Z fragments. The separation between different peaks is mainly dictated by the dependency on Z^2 of the energy loss (see Equation 1.1). However, it is clear that Q_{raw} does not scale linearly with the physical energy deposition in the scintillator. For example, given the dependency on the square of the charge, the energy loss of an O nucleus is approximately the double of that of a C nucleus with the same β. However, in Figure 3.10, it is clear that the ratio between the respective peaks (first and third from the right) is significantly lower than 2. This is a direct consequence of the light response of the plastic scintillator, which is intrinsically non-linear for higher energy depositions and thus needs to be carefully calibrated.

As it can be noticed, the energy loss already provides a good hint for charge identification and all possible Z values can be distinguished fairly well in the distribution. This is because FOOT detects the projectile fragments generated in beam-target interactions, which usually have a velocity similar to that of primary ions. This is mainly true for heavier fragments but not for light nuclei like H and He. As it will be discussed in Section 3.2, only the correlation between ΔE and TOF measurements can provide solid charge identification for all the observed particles.

During data acquisition, many quality checks are performed on the TW detector. The

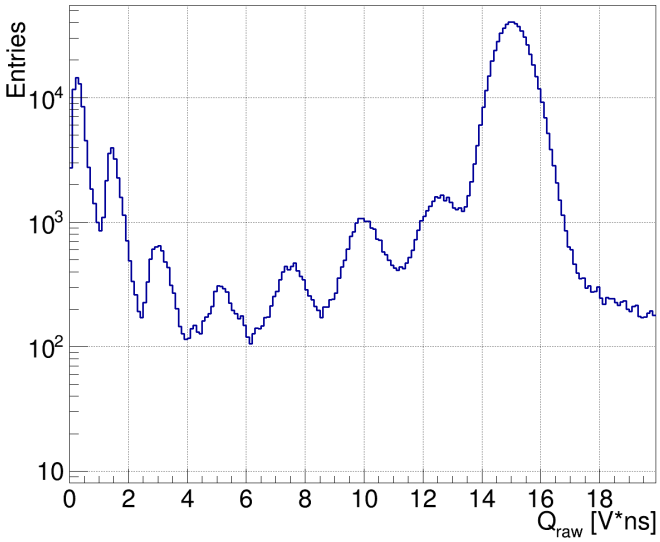

Figure 3.10: Example of raw energy loss distribution for one TW bar for a beam of ^{16}O ions at 400 MeV/u impinging on a carbon target. The visible peaks are generated by particles with different Z hitting the scintillator bar.

amplitude and Q_{raw} spectra of the central bars of the TW, i.e. those that participate in the fragmentation trigger VETO, are continuously monitored. This also allows to calculate online the thresholds for the fragmentation trigger and simulate the corresponding primary rejection performance through software without stopping the data acquisition. Moreover, the raw TOF is used to control the time resolution of the system and check its stability. Finally, a hit map of the detector is constructed by correlating bars fired in the front and rear layer of the TW to observe the irradiation of the detector.

3.1.4 Calorimeter

All the crystals of the FOOT calorimeter are connected to the WaveDAQ and acquired separately. The CALO has the final purpose to measure the kinetic energy of impinging particles, meaning that the most relevant information that needs to be extracted from signals is the total energy deposition in each of the crystals.

An example of the signals acquired from CALO crystals is shown in Figure 3.11. As expected, the response of BGO is much slower than the plastic scintillators, with resulting signals characterized by a long exponential tail. To acquire the whole signal, the sampling rate of CALO channels has been fixed at 1 GSample/s, which corresponds to an acquisition window of 1 μs.

The processing of CALO signals follows a procedure that is very similar to the one described for single TW channels. The main difference is that the integral of the waveforms, strongly related to energy deposition in the crystal, is evaluated up to the point where the signal starts to overshoot the baseline. This effect is solely related to the readout electronics and, thus, it would only spoil the information on the kinetic energy of the particle.

The online monitoring of CALO signals was shown to be of high relevance during detector calibration. In this phase the whole CALO has to be irradiated and a minimum statistics for each crystal is needed to correctly perform the calibration. The online monitoring of SLIPPER is mainly used to check the amplitude and raw energy spectra of

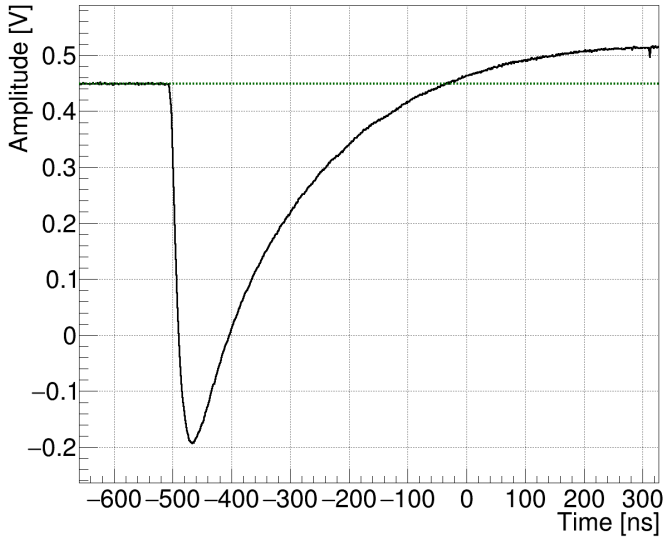

Figure 3.11: Typical signal acquired by a BGO crystal of the CALO as seen by the WaveDAQ. The green dotted line shows the baseline of the signal, highlighting the undershoot introduced by readout electronics. This component is the one removed during signal integration.

all the crystals and ensure that the required statistics for calibration is correctly acquired. This last check is performed building a global map of hits also for the CALO detector.

3.2 Fragment charge identification

Another important step of the analysis process is the charge identification of the detected particles. As said in the previous chapter, this step is carried out in FOOT through energy loss ΔE and Time-Of-Flight (TOF) measurements, performed by the SC and TW detectors. The reliability of this step is fundamental to obtain a correct evaluation of the interaction cross sections and, as described in Section 3.3, it also serves as a fundamental tool in track reconstruction.

The charge reconstruction algorithm is based on the combination of both data-driven and MC simulated information. For what concerns the first part, the raw quantities obtained from SC and TW signals (see Equations 3.2 and 3.3) have to be calibrated. The TOF calibration is straightforward: the TW detector undergoes a full scan with a particle beam of fixed and well-known energy, as that shown in Figure 3.9b. Then, the TOF_{raw} distributions are matched with the values for TOF obtained from MC simulations by applying a constant offset to each of the scintillator bars. The way these scans are performed, i.e. moving the detector perpendicularly to the fixed direction of the beam, also ensures that all primaries reaching the TW can be assumed to approximately have the same flight path.

At the contrary, the energy calibration of the TW is slightly more complicated to carry out, mainly because of two experimental effects on the detector response. First, the light output dL/dx of plastic scintillators does not depend linearly on the energy deposition in the material. In fact, to correctly model the response of such materials to ionizing

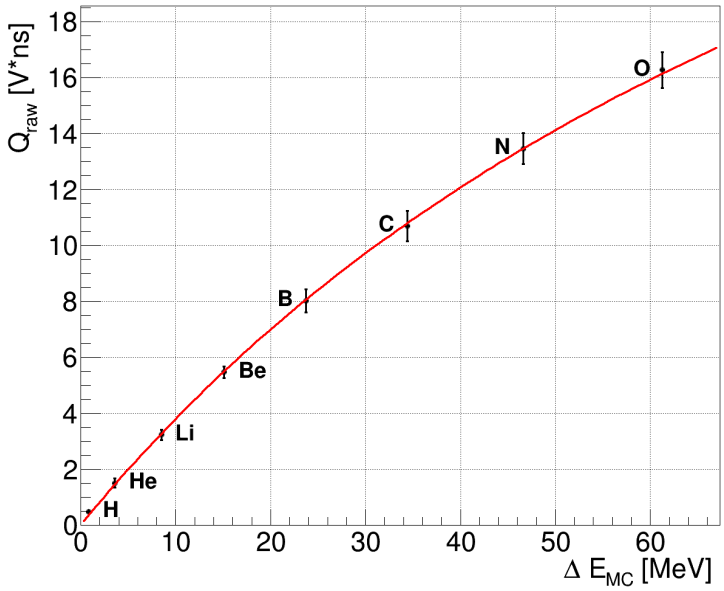

Figure 3.12: Example of the energy calibration curve of a TW pixel obtained using Equation 3.5. The different points are those associated to each Z observed. The data shown here have been obtained from a data acquisition with ^{16}O ions at 400 MeV/u.

radiation, it is mandatory to take into account the effect of saturation

$$\frac{dL}{dx} = \frac{S\frac{dE}{dx}}{1 + k\frac{dE}{dx}} \qquad \rightarrow \qquad Q_{raw} = \frac{p_0 \Delta E}{1 + p_1 \Delta E} \tag{3.5}$$

where p_0 (S) is proportional to the light output of the scintillator and p_1 (k) is the factor describing the quenching of light emission [82].

The other aspect that has to be considered is that the response of the TW slightly depends on the particle hit position along the bars. This is a direct consequence of the fact that light attenuation along the bar does not follow an exact exponential law, meaning that the raw energy deposition calculated with Equation 3.3 also retains a dependency on the hit position. Studies performed during several data takings with the TW detector have shown that the value of Q_{raw} between a particle hitting the center of the bar and one impinging on the side can vary of up to 15%, which is significantly higher than the required energy resolution.

The way these two effects are currently handled in FOOT is through a *pixel-by-pixel* energy calibration of the TW. The Q_{raw} distribution, as that shown in Figure 3.10, is calculated for each possible crossing of the TW, separately for the involved front and rear bars. Then, the peaks corresponding to each identifiable fragment are plotted against the expected energy loss from MC simulations and a fit using Equation 3.5 is performed. An example of a fit curve obtained with this procedure is shown in Figure 3.12. Once the p_0 and p_1 parameters have been evaluated, it is possible to obtain the energy release in a TW bar from Q_{raw}.

The approach chosen in this case is the one that optimizes the energy resolution achievable by the TW. However, it requires a non-negligible amount of statistics since it relies on the identification of fragment peaks which, as shown in Figure 3.10, are some orders of magnitude lower than primaries. Moreover, the underlying physics makes it impossible to observe heavier fragments in the TW crossings farthest from the center of the detector. This effect can be partially mitigated exploiting the TW scans needed to

perform TOF and position calibration. With such dedicated acquisitions, it is possible to measure the Q_{raw} for primary ions in all the pixels and obtain an energy calibration point in the region where the Birks curve saturates.

The other fundamental step needed to correctly apply the charge identification algorithm is the parameterization of the expected energy loss and TOF for each fragment. During data acquisition campaigns, the distance between each component of the experimental setup is accurately measured and then reproduced in FLUKA. Then, in the resulting MC simulations, the TOF and ΔE of all particles reaching the TW is saved and a Bethe-Bloch curve is computed to describe the average behavior of all ions with the same Z. An example of this procedure is shown in Figure 3.13a, where the eight regions corresponding to all possible charge values for a O beam are clearly distinguishable.

Once the calibration of the FOOT plastic scintillators has been performed and the Bethe-Bloch curves of all particles have been tuned with MC simulations, the charge identification algorithm can be applied. For each TW bar, the calibrated ΔE-TOF pair is plotted and the distance between the point and each Bethe-Bloch obtained from MC is computed. The charge Z associated to the bar hit is that of the closest curve in the ΔE-TOF plane.

Each particle crossing the TW is expected to switch on one scintillator bar per detector layer, meaning that a clustering algorithm is needed to properly combine the hits in the X and Y direction. The approach chosen in FOOT follows a so-called "*Z-match*" logic: each TW bar has a Z value associated and, between all possible crossings, only bars in the other layer which measured the same Z are considered as viable for clustering. If more than one combination of bars is possible, the one which matches best the hit position evaluated from Equation 3.4 is chosen. This criterion is considered quite reliable since the resolution on the position measurement ranges from 10 to 40 mm FWHM for higher and lower Z fragments, respectively [69], which is of the same order of the TW pixel size (2x2 cm^2).

An example of the charge identification resulting after the application of the Z-match is shown in Figure 3.13b. As it is easily noticeable, the main difference with the plot in Figure 3.13a is given by the energy and time resolution of the detector, which can lower the accuracy of charge measurement. The calibrated energy shown in Figure 3.13b is also slightly shifted with respect to the MC truth values. This is due to the ongoing energy calibration of the TW, which is still not optimized for the corresponding data acquisition campaign. However, it has been shown that, with the current experimental resolution and with an optimized TW energy calibration, the fragment charge mis-identification has been estimated to be less than 4% [50].

The charge identification algorithm of FOOT has been shown to be solid, producing reliable results with low mixing and, thus, high purity. It is important to notice that the "*Z-match*" condition constitutes a strong restriction on the number of TW bar crossings that could generate a valid point. This means that most of the ghost hits coming from misassociation of TW bars in the two layers are cut by the algorithm, leading to a significant decrease of the combinatorial background. However, this also leads to possible losses of signal whenever more than one particle hits the same bar. Suppose, for example, that two He fragments coming from the beam-target interaction arrive at the TW on the same bar of the first layer. In this situation it is almost impossible for the TW to disentangle the signals coming from each particle, meaning that they will create a single TW hit. Since $\Delta E \propto Z^2$, the charge identification algorithm is likely to associate $Z = 3$ to the hit. Two situations are thus possible:

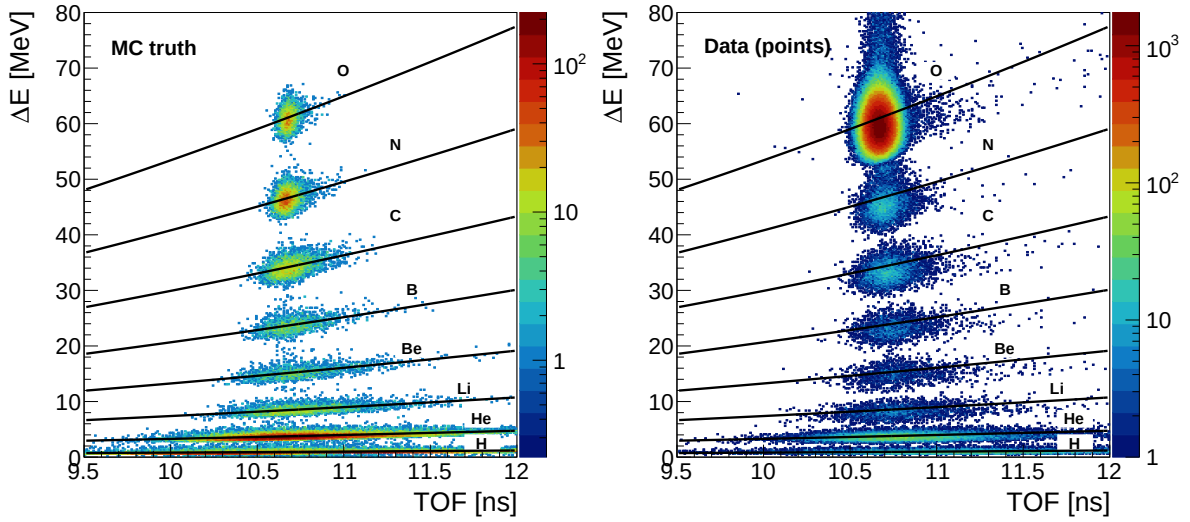

(a) MC truth

(b) Experimental data

Figure 3.13: Example of the charge identification algorithm application: (a) ΔE-TOF plane from MC simulations used for the tuning of Bethe-Bloch curves; (b) application of the charge identification algorithm to experimental data, showing the calibrated ΔE and TOF of all the reconstructed TW points.

- The two fragments cross two different bars in the other TW layer, creating two hits with $Z = 2$, as in Figure 3.14a. In this case, since the hit in the X layer is associated with a different Z, neither of the possible crossings satisfies the *Z-match* condition and they are both discarded by the charge identification algorithm.

- The two fragments reach the same TW bar also in the other layer, as shown in Figure 3.14b. In this situation the only active crossing actually identifies the same Z in both layers and the corresponding point is accepted by the algorithm. However, the detected Z is different from that of the particles hitting the detector.

The two examples described constitute the main limitations of the *Z-match* algorithm. As a matter of fact, the first situation leads to the rejection of some "good" fragmentation events, i.e. a loss of signal, while the second one determines a Z mis-identification background. Considering the performance of the detector in terms of time and energy resolution, it is very complicated to further optimize the charge identification using only the information coming from the TW. However, one of the main tools that can help to recognize - and eventually disentangle - such kind of events is particle tracking, which is performed by the FOOT Global Reconstruction.

3.3 Global track reconstruction

One of the fundamental steps in FOOT data processing is the extraction of particle momentum, the so-called *Global Reconstruction*. This consists in the identification, classification and fitting procedure of all the particle tracks in an event, from the primary interaction point in the target to the downstream region of the setup.

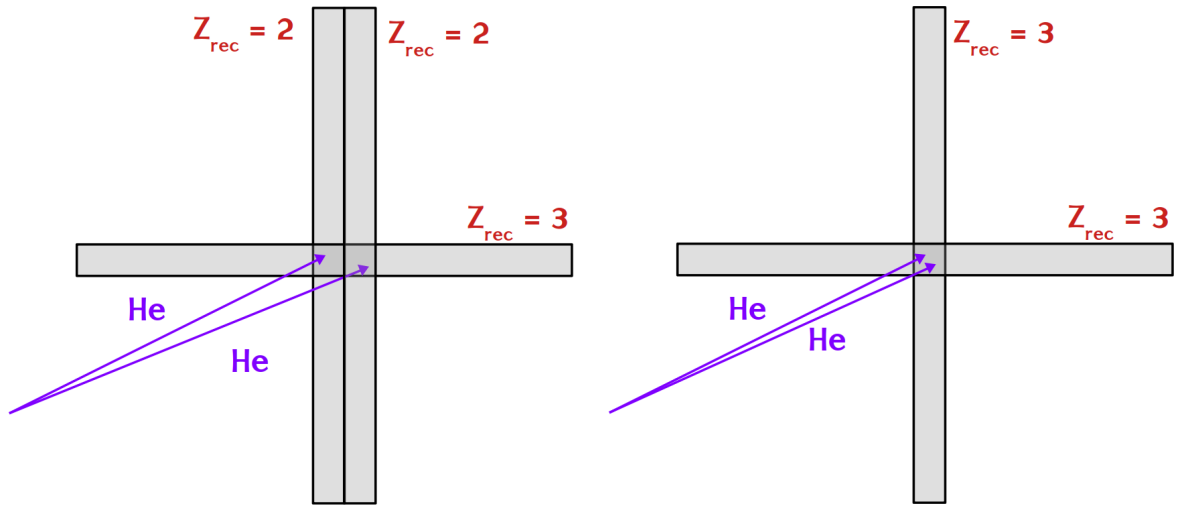

(a) Pile-up without matching (b) Pile-up with matching

Figure 3.14: Example of two different types of TW pile-up events and behavior of the Z-match algorithm. (a) Fragments hitting two bars in one layer and (b) two particles crossing the same TW point. The Z indicated is that reconstructed by each bar crossed in the event.

In general, any particle tracking algorithm is divided in two separate steps: *track-finding* and *track-fitting*. The aim of track-finding is to group all the measurements that are likely generated by the same particle traveling through the experimental apparatus. Accurate pattern recognition and track following procedures are needed to provide a set of suitable track candidates to the following step of the reconstruction. Track-fitting has the aim to evaluate the most suitable set of track parameters compatible with the measurements belonging to each of the track candidates, taking into account the uncertainties on the measurements and the interaction with materials along the trajectory.

Tracks are usually parameterized using the position $\vec{x}$ and momentum $\vec{p}$ of the particle moving through the setup, but many different choices can be made. In this sense, reconstructing a track means being able to calculate such parameters and their covariance at any given point of the trajectory of the particle.

As of today, two independent track reconstruction algorithms have been implemented in SHOE. The first one is based on the TOE package and is currently maintained by the Strasbourg group of FOOT [83], while the second one uses the GENFIT toolkit and has been developed by the Bologna group. During my thesis work, I mainly contributed to the development, testing and integration of the latter in the SHOE framework.

3.3.1 The GENFIT toolkit

GENFIT [84, 85] is an experiment-independent toolkit dedicated to the reconstruction of particle tracks made of a set of noisy measurements. It is an open-source C++ object-oriented, modular framework fully integrated with ROOT and Geant4. GENFIT provides a built-in flexible structure that is able to handle different types of detectors and measurements at the same time. The framework makes it possible to combine all the position measurements in a single track candidate that can then be processed with different fitting algorithms.

The structure of GENFIT is built on three main units:

- Measurements
- Track representations
- Fitting algorithms

Measurements are objects containing the coordinates measured by a sensitive device. They are always built using a detector plane as reference and contain information about local coordinate measurements and uncertainties on that plane. Any detector plane created in GENFIT is defined by its origin $\vec{o}$, local reference unit vectors $\hat{u}$ and $\hat{v}$ and normal versor $\hat{n} = \hat{u} \times \hat{v}$. The construction of active and passive components of the experimental setup is completely interfaced with ROOT geometry classes for easier implementation. The measurements provided by detector planes can be one-dimensional (e.g. from a stripped detector), two-dimensional (e.g. position measured in pixelated sensors) or three-dimensional (e.g. space points from a Time Projection Chamber).

In general, a track is described by a set of parameters (such as position and momentum) and their corresponding covariance matrix. In the absence of interaction, the trajectory of a charged particle moving inside a magnetic field is determined by the equation of motion. Knowing the values of the track parameters at a certain position in space, it is possible to define a model able to extrapolate the track parameters at any other given position along the trajectory. In GENFIT, *Track Representations* contain the information on both track parameterization and track extrapolation models.

Different types of Track Representations are available in GENFIT, but that employed in the FOOT Global Reconstruction is the one called `RKTrackRep`. In such kind of representation, the state $\mathbf{x}$ of a particle track with position $\vec{r}$ and direction $\vec{a}$ is parameterized in a local plane with origin $\vec{o}$ and normal versor $\hat{n}$ using a 5 coordinate vector

$$\begin{aligned} \mathbf{x} &= (q/p, u', v', u, v) \\ u' &= \frac{\vec{a} \cdot \hat{u}}{\vec{a} \cdot \hat{n}} \\ v' &= \frac{\vec{a} \cdot \hat{v}}{\vec{a} \cdot \hat{n}} \\ u &= (\vec{r} - \vec{o}) \cdot \hat{u} \\ v &= (\vec{r} - \vec{o}) \cdot \hat{v} \end{aligned} \tag{3.6}$$

where q and p are the charge and momentum of the particle and $\hat{u}$ and $\hat{v}$ are the versors of the local coordinate reference frame of the plane. u and v represent the coordinates of the track in the local reference frame of the plane, while u' and v' are the track direction cosines with respect to the versors of the plane. An example of all the relevant vectors used in the described track parameterization are shown in Figure 3.15.

For what concerns track parameters extrapolation, a particle moving inside a magnetic field is expected to follow a helical trajectory described by the equation of motion

$$\frac{\mathrm{d}^2\vec{r}}{\mathrm{d}s^2} = \frac{q}{p}\left(\frac{\mathrm{d}\vec{r}}{\mathrm{d}s} \times \vec{B}(\vec{r})\right) \tag{3.7}$$

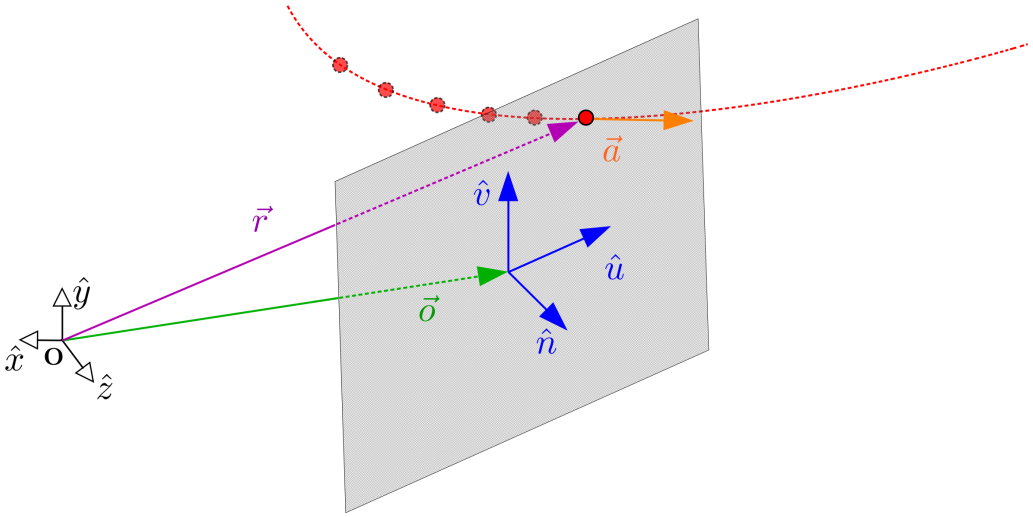

Figure 3.15: Visualization of a track parameterization in GENFIT. The origin $\vec{o}$ and local directional versors $\hat{u}$, $\hat{v}$ and $\hat{n}$ of the plane are shown.

where $\vec{r}$ is the position vector of the particle, s is the curvilinear coordinate along the track, q and p are the charge and momentum of the particle and $\vec{B}(\vec{r})$ is the magnetic field. Due to field inhomogeneities, however, it is normally impossible to solve such equation with an analytical approach. The `RKTrackRep` class overcomes this problem using a fourth order Runge-Kutta-Nysrtöm (RKN) method to perform track extrapolation in between different planes. RKN algorithms constitute a well-established, standard approach to provide numerical solutions to differential equations [86] and, in the case of particle trajectories, they can be employed to solve Equation 3.7. Given a certain state vector in the form of Equation 3.6, the `RKTrackRep` class applies the RKN method to Equation 3.7 in order to extrapolate the track parameters at any position along the trajectory. [87]

In GENFIT, *Tracks* are data structures containing a list of measurements and track representations. *Fitting algorithms* have access to all the information contained in tracks, meaning that they use all the measurements and track extrapolation functions of the representations to calculate the fit results. GENFIT provides a series of track fitting algorithms, described in detail in [88]. Among these, the one used in the FOOT Global Reconstruction is the Kalman Filter.

The Kalman Filter

The Kalman Filter [89] is a widely used regression algorithm in particle physics experiment for particle track reconstruction. It was developed with the aim of finding the optimal estimate for the state vector $\vec{x}_k$ and covariance matrix C_k of a system starting from a set of noisy measurements. It is an efficient progressive fitting algorithm which successively adds the information from single detector hits to the estimated track parameters using a quasi-linear model of track propagation.

Let us consider a system with state vector $\vec{x}_{k-1}$ and covariance matrix C_{k-1} determined through the information of all hits up to index $k-1$. The Kalman Filter recursive algorithm acts on such system through a two-stage process: prediction and update. In the *prediction* stage, the state vector and covariance matrix at index $k-1$ are extrapolated to the next point k. The predicted state vector $\tilde{\vec{x}}_k$ is obtained through the state extrapolation model, while the covariance matrix $\tilde{C}_k$ results from the sum of the extrapolated

covariance and a noise matrix $N_{k-1|k}$ that considers possible additional uncertainties in the propagation from state $k-1$ to state k

$$\begin{aligned} \tilde{\vec{x}}_k &= f(\vec{x}_{k-1}) \\ \tilde{C}_k &= J_{k-1|k} C_{k-1} J_{k-1|k}^T + N_{k-1|k} \end{aligned} \tag{3.8}$$

where $f(\vec{x})$ is the state extrapolation function and

$$J_{k-1|k} = \left. \frac{\partial f(\vec{x})}{\partial \vec{x}} \right|_{\vec{x}=\vec{x}_{k-1}}$$

denotes the Jacobian error propagation matrix given by the extrapolation model. Then, in the *update* step, the state vector $\vec{x}_k$ and the covariance matrix C_k are re-computed taking into account the k-th measurement $\vec{m}_k$:

$$\vec{x}_k = \tilde{\vec{x}}_k + K_k \tilde{\vec{r}}_k \tag{3.9}$$

$$C_k = (I - K_k H_k) \tilde{C}_k \tag{3.10}$$

where $\tilde{\vec{r}}_k$ denotes the residual of the predicted state

$$\tilde{\vec{r}}_k = \vec{m}_k - H_k \tilde{\vec{x}}_k \tag{3.11}$$

and the matrix K_k, called Kalman Gain, is the weight of the residual

$$K_k = \tilde{C}_k H_k^T \left(H_k \tilde{C}_k H_k^T + V_k \right)^{-1} \tag{3.12}$$

Here, the matrices I and V_k are the unit matrix and the covariance matrix of measurement $\vec{m}_k$, respectively. The matrix H_k performs the projection from the coordinate system of the state vector $\vec{x}_k$ to the one of m_k (as it can be noticed in Equation 3.11). If we rewrite Equation 3.9 using Equation 3.11, it can be noticed that

$$\vec{x}_k = (I - K_k H_k)\, \tilde{\vec{x}}_k - K_k \vec{m}_k \tag{3.13}$$

This expression means that the Kalman Gain matrix K_k determines how much the updated state vector $\vec{x}_k$ depends on the measurement $\vec{m}_k$ and on the predicted state $\tilde{\vec{x}}_k$. The weight of each component is solely dependent on the covariance matrices of both the hit and the track parameters.

With the formalism described above, the number of degrees of freedom $n_{d.o.f.}$ of the Kalman Filter fit will be given by

$$n_{d.o.f.} = \sum_k \dim(\vec{m}_k) - n_{par} \tag{3.14}$$

where n_{par} is the number of track parameters in the model chosen ($n_{par} = 5$ for the `RKTrackRep` class). The contribution of hit k to the χ^2 of the fit is calculated as

$$\chi_k^2 = \vec{r}_k{}^T \left(V_k - H_k C_k H_k^T \right)^{-1} \vec{r}_k \tag{3.15}$$

with $\vec{r}_k = \vec{m}_k - H_k \vec{x}_k$ indicating the residual on the updated state vector $\vec{x}_k$ calculated with Equation 3.9 [88, 90].

As it can be noticed, the Kalman Filter formalism does not depend on the nature of the system under study nor on the propagation models, meaning that it can be employed in many different research fields. In the case of particle tracking, the Kalman Filter is applied considering the state vector of the system as in the form of Equation 3.6. The extrapolation function is given by the track propagation model and the noise matrix takes into account the possible energy loss and multiple scattering effects due to crossed materials in the propagation between subsequent states.

One of the main reasons why the Kalman Filter is particularly suited for tracking is that, contrary to a normal least squares fit, the state vector of the system is re-computed at each point separately. This feature is crucial for particle track reconstruction since it enables the possibility to take into account the evolution of track parameters step-by-step as new reconstructed hits are added to the track. As a matter of fact, a global track fit with an helical trajectory would not be able to properly consider the deviations introduced by multiple scattering and particle energy deposition, while the Kalman Filter handles such perturbations through the noise matrix used in the propagation of track parameters covariance. This is particularly important when considering low momentum particles, where scattering and energy loss become more significant [91]. An example of the comparison between a standard least squares fit and the Kalman Filter is shown in Figure 3.16.

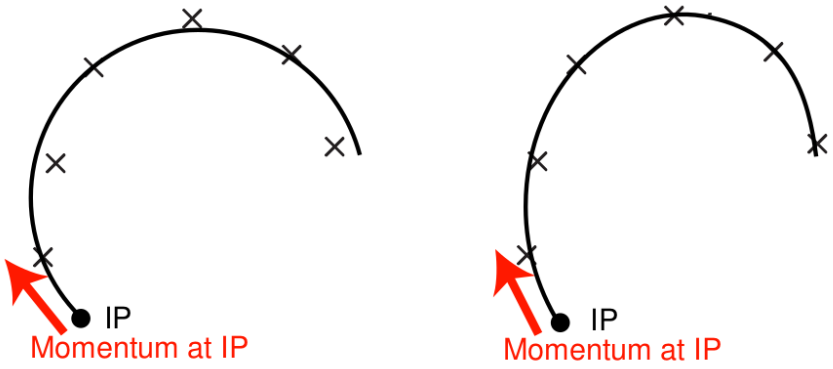

Figure 3.16: Comparison between normal least squares fitting (left) and Kalman filter based fitting (right) applied to the same trajectory. The track parameters are evaluated only once in the first case, while they are updated at each added point in the Kalman Filter approach (from [91]).

The Kalman Filter implemented in GENFIT contains also an additional feature. Since a single iteration of the Kalman Filter could be biased by the initial seed state vector provided for the fit, the algorithm is progressively applied to the tracks in the forward and backward direction multiple times. When switching between forward and backward fitting, the last state of the previous fit is used as seed for the next step of the iteration. Moreover, at each step, the track parameters estimated for all measurements in the previous iteration are taken as reference states . At the end of the procedure, the forward and backward fitted tracks are then combined through a weighted average in order to obtain the final track parameters at each point of the trajectory. This continuous smoothing process further improves the robustness of the fitting procedure [88].

To summarize, GENFIT provides a set of useful tools for track extrapolation and fitting, which also allow to effectively take into consideration the effects of multiple scattering and energy loss on particle trajectories. However, one important aspect to note is

that GENFIT itself does not provide any measurement classification or pattern recognition routine. This means that a separate track finding algorithm has to be developed in order to provide a set of suitable track candidates to be fitted. This is the core task of the FOOT Global Reconstruction.

3.3.2 The FOOT Global Reconstruction

The FOOT Global Reconstruction provides the connection between SHOE data structures and the GENFIT package. Its final purpose is to convert all the information provided by single detectors in particle tracks and evaluate the momentum of all detected nuclear fragments.

The first step performed by the Global Reconstruction is to import the FOOT geometry from SHOE configuration files in a GENFIT-like format. During this stage, all passive materials and active detector planes are defined in space according to the setup of the campaign under study. The detectors used for particle tracking are the three silicon stations of the magnetic spectrometer (VT, IT and MSD) and the TW detector. For each of these, suitable detector planes are defined in order to provide a reference for GENFIT measurements. In this stage, the full map of the magnetic field is also included and loaded into the geometry. A picture of the full FOOT setup reconstructed in GENFIT is visible in Figure 3.17.

Figure 3.17: Full geometry of the FOOT electronic setup as reconstructed in GENFIT.

The FOOT Global Reconstruction is employed on all the events which satisfy a minimal set of quality requirements in the upstream region of FOOT. In particular, before applying the Global Reconstruction, an event should have no pile-up in the SC (see Section 3.1.2) and only reconstruct one particle track in the BM. These two requests should be enough to remove the possibility of having multiple primaries in the same event and of observing nuclear fragments produced before the target, respectively. For what concerns the BM, the request of a single particle is also fundamental to obtain the fragment emission angle since the BM track has to be used as a reference for the measurement.

The event processing logic of the Global Reconstruction is made of three consecutive steps with different focus, each represented by a different class in SHOE:

- The *Uploader*, which takes the information from all the hits[1] identified in the dif-

[1]From here on, the points measured by each detecting plane of the spectrometer will be referred to as *hits*, *clusters* or *points*. The names *clusters* and *points* have been derived from those used in the SHOE software which refer to collections of pixels (VT and IT), strips (MSD) or bars (TW).

ferent FOOT detectors and converts it in a GENFIT-like format.

- The *Track Selector*, which performs the pattern recognition step and determines all the possible track candidates of an event, as well as their track representations.

- The *Track Fitter*, which performs the actual fit of the previously selected track candidates and records all the relevant information for further analysis.

These three steps are performed in series for each processed event. In general, the first and last step are always carried out in the same way. The Uploader works mainly as an intermediary between the SHOE objects and the GENFIT structures. For each of the detectors used for tracking, the Uploader saves the position of all the recorded clusters of hits and sends them to the Selector. The VT, IT and TW provide a 2-D position measurement on their sensitive planes, while MSD clusters are considered to be 1-D measurements along the silicon strips.

For what concerns the final step, the Track Fitter receives a list of track candidates from the Selector and tries to fit all of them with the Kalman Filter using a set of reasonable assumptions, all embedded in the corresponding track representations. If the fit performed on a certain candidate converges, the track measurements and resulting parameters are saved to the output for further analysis. The convergence criteria applied to track reconstruction are two: first, the change in the p-value of the fit has to be limited to 10^{-3} between two consecutive forward and backward iterations of the Kalman Filter and, then, a maximum $\chi^2/n_{d.o.f.}$ value is required. All the candidates that do not satisfy these convergence criteria after a maximum of 20 iteration of the Kalman Filter are marked as fakes and removed from the results of the reconstruction. An example of the fitted tracks obtained from the Track Fitter is shown in Figure 3.18.

The most important step of the Global Reconstruction is however the Track Selector, which provides the list of possible track candidates and representations to the Fitter. The Track Selector implements a set of track following algorithms with different focus and applications. However, all of them are based on local methods of pattern recognition and share a certain number of characteristics.

Firstly, all local methods of pattern recognition need a track model, i.e. a parameterization of particle trajectories and a set of functions that can be used to transport track parameters along the direction of motion. In the case of the Track Selector, this feature is ensured by the usage of GENFIT `RKTrackRep` class, described in Section 3.3.1, for track candidate construction, parameterization and extrapolation.

Secondly, the algorithm needs a method to produce a set of seed *tracklets*, i.e. initial track candidates which can be used as a starting point for the track following procedure. These tracklets are usually created using a minimal sub-set of the available detector planes using either physical or geometrical assumptions on the expected behavior of particles. The detector planes used to construct such seed tracks can belong to the same detector or to different ones depending on the chosen tracking approach. Two seed construction algorithms will be discussed in later sections.

Finally, track following algorithms need a set of quality criteria to decide whether a track should be considered as a viable candidate for the fitting procedure or not. The choice of these criteria can be made in terms of global characteristics of the candidate, e.g. a minimum number of assigned detector hits, or local features of the extrapolated states and measurements, e.g. the track propagation falls inside the geometrical acceptance of a certain detector.

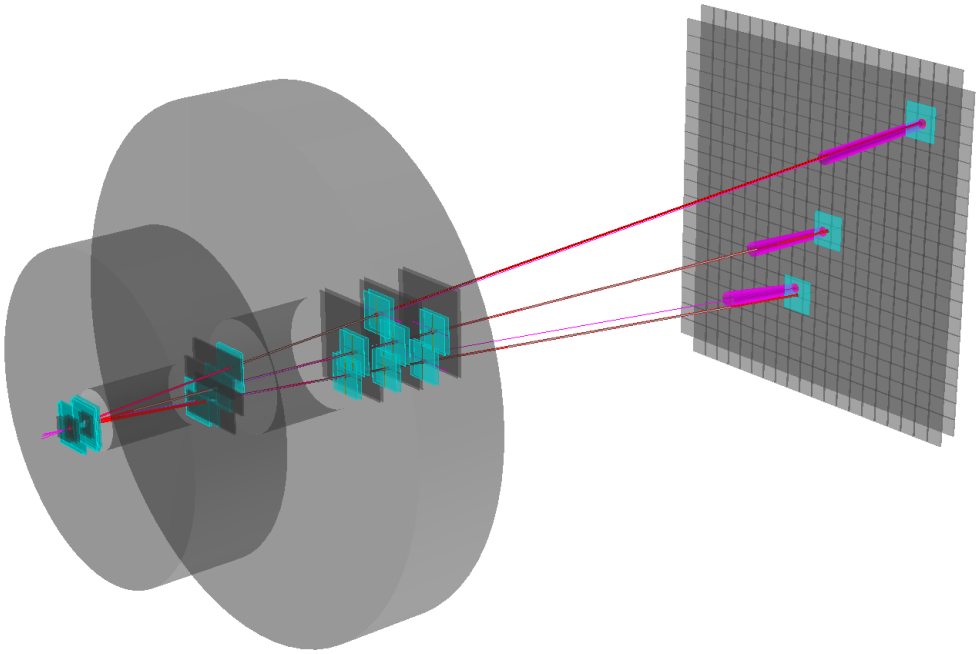

Figure 3.18: Example of a fragmentation event reconstructed using the FOOT Global Reconstruction. Here, the algorithm finds 3 particle tracks in the setup, shown with the red lines. The cyan and purple lines show the forward and backward Kalman Filter fits, respectively. The cyan squares highlight particle hits (yellow) on the different detector planes. The picture only shows the magnetic spectrometer and the TW detector, while all other parts of the setup have been removed for clarity.

In the case of the FOOT Global Reconstruction, the implemented track following algorithms also share the same cluster assignment logic. Each time a track candidate is extrapolated to the next detector, a new possible cluster from the corresponding sensitive plane can be assigned to the candidate. Given the low track multiplicity expected in FOOT fragmentation events, a simple proximity check is currently employed: all the hits on the plane are compared with the track extrapolation point and the closest one is added to the track candidate for further processing. This approach is based on the assumption that particles will follow the helical trajectory expected from the equation of motion. If the track propagation model is accurate and the geometry and magnetic field are known with enough precision, the extrapolated states are expected to reproduce the corresponding detector hits in accordance to experimental uncertainties.

The only expected and unavoidable deviation of particle trajectories is given by Multiple Coulomb Scattering. An efficient Track Selection algorithm should properly consider the effects of this component. Multiple Scattering can be considered mainly as a source of uncertainty, meaning that the Track Selector should take into account the expected deflections given by Multiple Scattering. This is usually treated by imposing a reasonable tolerance for cluster assignment, i.e. a maximum accepted geometrical distance between the track candidate extrapolation to a detector plane and the reconstructed cluster to be assigned. All clusters of a detector plane outside the tolerance region of a track candidate are not considered in the assignment. A visualization of this requirement is shown in Figure 3.19. Note also that, with the implemented selection logic, only one cluster per detector plane can be assigned at maximum to the track candidate. At the same

time, a single cluster can be assigned to multiple track candidates, taking into account the possibility of having more particles traveling through the same reconstructed detector hit.

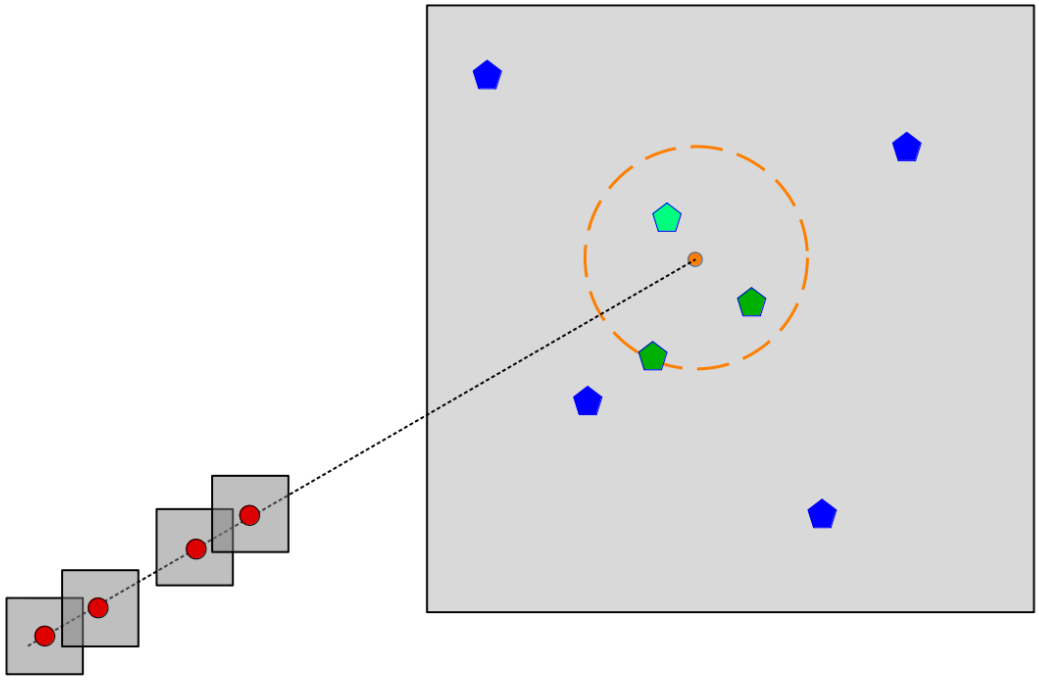

Figure 3.19: Example showing the algorithm for cluster assignment to a track candidate: the track candidate containing the already assigned clusters (red dots) is extrapolated up to the following detector plane. From the point found through the extrapolation (orange dot), all clusters at a further distance with respect to the chosen tolerance are discarded from the assignment (blue). The distance of all the clusters inside the tolerance region (dark green) is computed and the closest one to the extrapolation (light green) is assigned to the track.

In some rare cases, a particle real trajectory can be scattered outside the chosen extrapolation tolerance. These tracks are lost during the track finding step but they do not pose a problem, since they would be removed anyways by the convergence criterion applied during the track fitting procedure. In all the other, most probable cases, the deflection of trajectories is very small and the reconstructed cluster falls inside the tolerance region.

Here, a list of all the currently available track following algorithms in the FOOT Global Reconstruction is provided, together with a detailed description of their approach and application.

TrueParticle algorithm

The *TrueParticle* is the only selection algorithm in SHOE that has been conceived to run exclusively on Monte Carlo simulated data. It emulates perfect cluster selection and track candidate construction hypothesis, such as particle charge, mass and initial momentum, using directly the information from Monte Carlo truth. This type of algorithm was developed with the aim of carrying out performance studies on the track fitting step and have a direct comparison with other selection algorithms.

This track following algorithm is the only one implemented in SHOE that has complete access to the MC information and, thus, can not be used on real data. Every other selection algorithm is performed using a "data-like" approach, which treats MC generated clusters in the same way as it would for raw data, i.e. using only reconstructed quantities, and can then be applied indistinctly to both.

Standard algorithm

The *Standard* algorithm implements a forward track following approach. This selection algorithm tries to follow the possible track candidates from the target up to the TW, assigning additional measurements while going through the different detectors. The steps of the algorithm are shown in Figure 3.20.

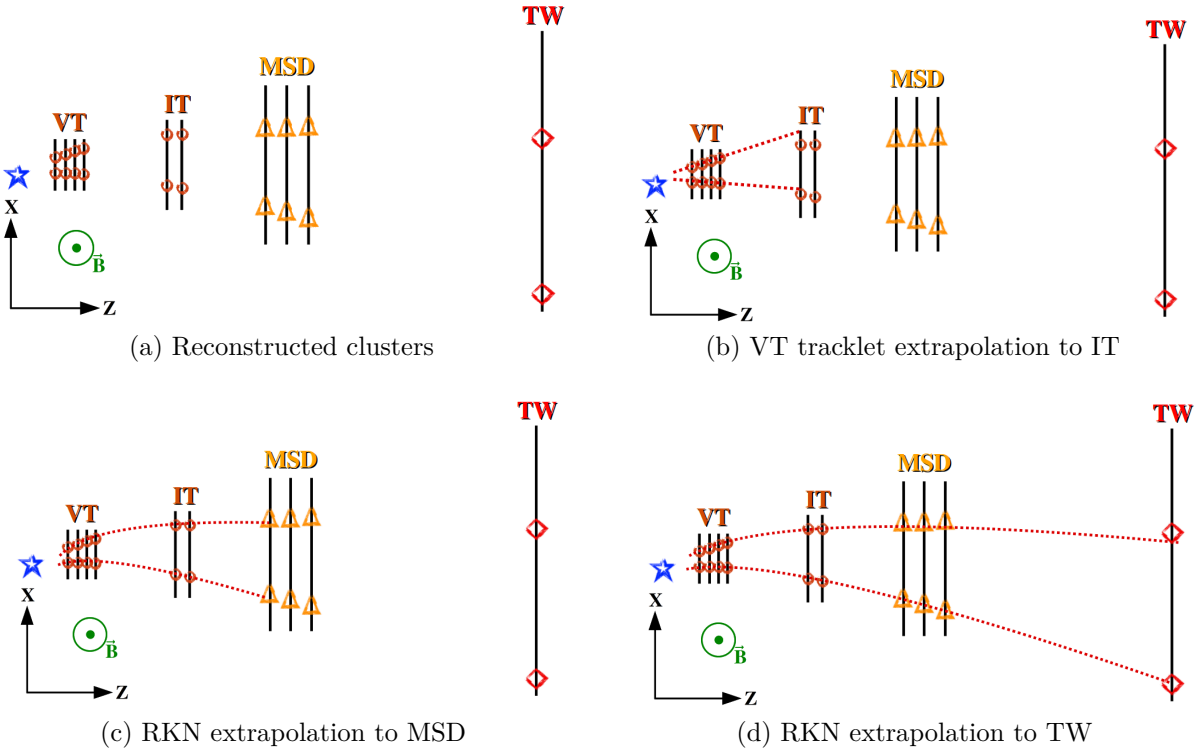

(a) Reconstructed clusters

(b) VT tracklet extrapolation to IT

(c) RKN extrapolation to MSD

(d) RKN extrapolation to TW

Figure 3.20: Steps of the *Standard* selection algorithm in a (a) typical event with magnetic field. In the different panels, a sketch of the FOOT setup in the XZ projection is shown, with the magnetic field directed along Y exiting from the page. Each station of the MSD is represented as a unique system that comprehends an X and a Y stripped sensor. (b) The VT tracklets are linearly extrapolated to the IT and the nearest clusters are added to the candidate. (c) The new candidate is extrapolated to the MSD and (d) then to the TW using the Runge-Kutta-Nyström model.

The *Standard* algorithm starts from the tracklets identified inside the VT detector alone. The VT provides a series of algorithms for tracklet construction, all based on an approach similar to the one described above for cluster assignment in global tracking. Two of the four chips of the VT are used as seed and a segment is created for all possible couples of clusters. These segments are linearly extrapolated to the other two planes and the closest clusters, inside a reasonable tolerance, are added to the tracklet. The main difference with global tracking is that, in the case of the VT, a cluster can only

be assigned to a single tracklet. This exclusion logic can reasonably be applied to the VT sensors for their very high granularity (20μm pixel pitch), but the same can not be stated for global tracking. As an example, the measurements produced in the MSD are 1-dimensional, meaning that two particles hitting the detector in different positions could leave a signal on the same strip. In that case, the resulting cluster should have to be assigned to two track candidates, which is not possible using the same assignment logic of the VT detector.

The tracklets found by the VT with at least 3 clusters are then projected in the forward direction up to the IT using a linear extrapolation. The closest cluster is assigned to each track candidate and the extrapolation is repeated through all the geometry of the IT. In this step, the distance for cluster assignment is taken using only the axis of the FOOT geometry along which particle trajectories do not bend, i.e. in the direction of the magnetic field. This choice is made to avoid using the RKN extrapolation while no knowledge of the particle kinematics is available. As a matter of fact, the RKN model needs a seed state to start the extrapolation, which means an initial guess of the particle position and rigidity q/p. At the level of the VT, no information about the possible charge and momentum of the particle is known and any wrong assumption would lead to errors in the extrapolation and cluster assignment.

The assumption on particle type and kinematics is made after the IT cluster assignment to perform the track extrapolation up to the first plane of the MSD. At this stage, a separate Track Representation is created for each possible Z seen by the TW in the event. The starting position for the fit is set as that of the VT cluster in the closest plane to the target. The seed value for the momentum of each of these fits is constructed assuming that the particle has the mass of the most abundant isotope with the corresponding Z (e.g. ^{7}Li for $Z = 3$) and the β of the primary. These approximations are made considering that the nuclear fragments observed by FOOT are all projectile fragments, which are generally emitted with speed similar to that of the primary ion.

Starting from these seed states, the track is fitted with one iteration of the Kalman Filter using all possible representations and the one with the lowest $\chi^2/n_{d.o.f.}$ is kept as good. The track is then extrapolated with the RKN model to all the planes of the MSD to add new clusters to the track candidate. Here, the distance used for hit assignment is the 1-D separation between the cluster measurement and the track projection. For each new added cluster, the track is re-processed with a single iteration of the Kalman Filter to slightly correct the intermediate state vectors. The final step of the algorithm is the RKN extrapolation and hit assignment at the TW level. When the closest point is added to the track, a correction to the initial guess on the seed state of the track is performed using the information of the TW. In particular, the Z chosen in the previous steps of the algorithm is checked against the one calculated from the TW and matched to it if needed. Moreover, the new seed for the momentum is computed using the measured TOF of the fragment and the length of the track candidate.

During each of the iteration of the Kalman Filter used in track extrapolation, the candidates which do not satisfy the convergence criteria of the fit are discarded from the processing. Instead, those reaching the end of the extrapolation are sent to the Track Fitter with the corrected seed states to undergo the actual fitting procedure.

The *Standard* algorithm strictly requires the presence of the VT and TW detectors in the setup. If either the IT or the MSD were missing in the analyzed data set, the corresponding steps of the track finding algorithm are simply skipped. The same applies for acquisition campaigns without the magnetic field.

Linear algorithm

The *Linear* selection algorithm was developed with the aim of simulating the *Standard* pattern recognition in the case where no magnetic field is present in the FOOT setup. The main purpose was to try and achieve the same performance of the RKN track extrapolation with a much less demanding approach, both in terms of computing power and processing time.

When the magnetic field is not present, the particles are expected to follow an approximately straight path through the setup. The working principle of this algorithm follows the same steps of the *Standard* one but it never uses the RKN extrapolation in the track following procedure. The slope of each track candidate identified by the VT detector is computed and used to perform a linear extrapolation to all of the other detector planes. For each of these planes, the cluster closest to the extrapolation is added to the track candidate. As for the *Standard* algorithm, a pre-defined tolerance on the maximum distance between track extrapolation and reconstructed clusters is set for each detector. In the case of the *Linear* algorithm, the extrapolation tolerance is set to include the possible deviations from a straight trajectory due to Multiple Scattering.

As for the *Standard* algorithm, the *Linear* algorithm strictly requests only the presence of the VT and TW detectors.

Backtracking algorithm

The *Backtracking* algorithm is based on a completely different approach with respect to the other data-like procedures. It starts the pattern recognition of particle tracks from the last detector considered for tracking, i.e. the TW, and tries to reconstruct the trajectories in the backward direction, towards the target. The steps of the whole procedure are sketched in Figure 3.21.

The starting point of the *Backtracking* algorithm is the construction of track candidates from TW points and MSD clusters. The first tracklets are constructed using a combinatorial approach: each TW point is associated to all possible couples of X and Y clusters in the central MSD station. This approach yields a starting number of tracks that is likely higher than the actual one, so each further step has to take into account possible track mixing. The position of the MSD and TW measurements provides a seed for track direction which is used for the extrapolation to all other planes of the MSD. The cluster of each plane closest to the extrapolation, if compliant with a maximum tolerance, is then added to the tracklet.

From here, tracks with a minimum of 4 assigned clusters in the MSD are processed with a preliminary fit to check if the trajectory is compliant with a realistic one. To perform the fit, a track representation and seed are needed. In the case of the *Backtracking* algorithm, both are inferred using the information coming from the TW point, i.e. the measured TOF and Z of the particle. The track representation is initially set as the most abundant isotope with charge Z, for example ^{11}B for $Z = 5$ or ^{4}He for $Z = 2$. TOF is then used to estimate the β of the particle and thus extract the corresponding momentum seed for the supposed particle. With these assumptions, track candidates are fitted with a single iteration of the Kalman Filter and the non-converging ones are deleted. This control is fundamental (and in most cases sufficient) to remove most of the combinatorial fake tracks constructed with the first step of the reconstruction.

The remaining track candidates are then extrapolated backwards to the planes of the IT detector, adding reconstructed hits according to the cluster assignment process

already described. For each added cluster, the track candidates undergo an additional single iteration of the Kalman Filter and the consequent removal in case the regression fails. The process is then repeated on the VT detector planes for all remaining candidates. After this step, an additional quality criterion is applied and only the track candidates with at least two clusters in the VT and IT are considered as reliable and sent to the Track Fitter.

One of the main advantages of this algorithm is that it starts the track-finding step from the detector with the lowest occupancy, the TW, which also provides a set of reasonable assumptions for the track seed. As a matter of fact, the TW point provides both the TOF measurement and the charge Z of the observed fragment, meaning that such information is available from the start of the pattern recognition step. This improves significantly the accuracy of track extrapolation between the different measuring stations of the magnetic spectrometer.

The *Backtracking* algorithm requests the presence of MSD and TW for the construction of seed track candidates, while the IT and VT are not strictly required. This means that it can be applied to all the data sets of the experiment which include the MSD and TW detectors, both with and without a magnetic field.

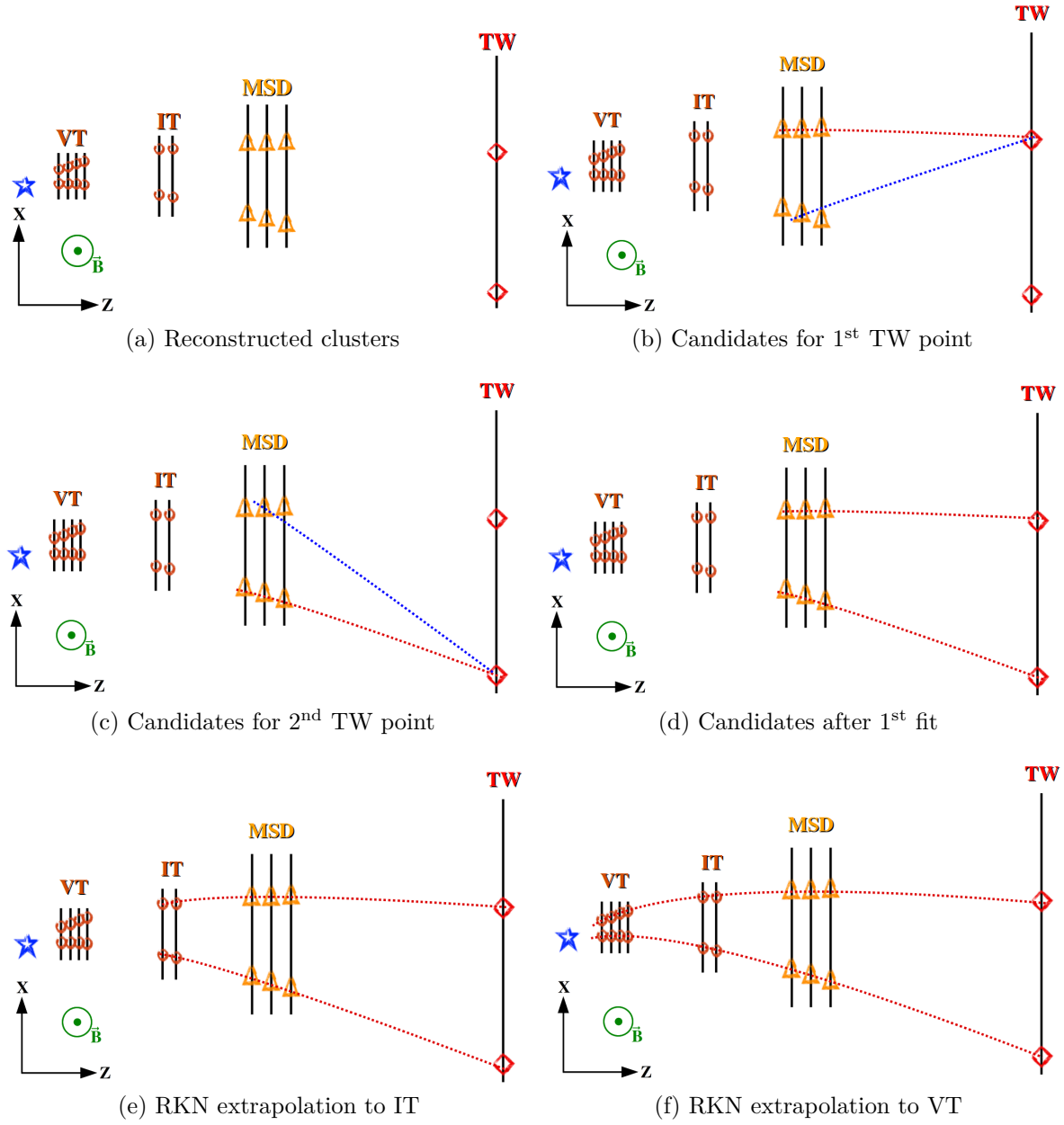

(a) Reconstructed clusters

(b) Candidates for 1st TW point

(c) Candidates for 2nd TW point

(d) Candidates after 1st fit

(e) RKN extrapolation to IT

(f) RKN extrapolation to VT

Figure 3.21: Steps of the *Backtracking* selection algorithm in a (a) typical event with magnetic field, show in the same view of Figure 3.20. For both TW points ((b) and (c)), a track candidate is created using all possible combinations with the central station of the MSD. (d) After the 1^{st} fit, only the candidates compliant with the requirements are left and (e) are extrapolated to the IT. (f) The track candidates are extrapolated to the VT and the respective closest clusters are added.

Chapter 4

Data analysis

As said in the previous chapters, the goal of the FOOT experiment is to characterize nuclear fragmentation reactions evaluating their double differential cross section in terms of emission angle and kinetic energy. The reliability of the analysis procedure stems from the evaluation of the performance of the whole reconstruction chain. One of the most important steps is then the characterization of the FOOT Global Reconstruction. As a matter of fact, the developed global tracking algorithms have never been employed before on real data and on MC and, thus, they have to be properly characterized. The main objective of this work is the evaluation of the Global Reconstruction performance, from track selection to background rejection and cross section calculation.

To perform such task, all the algorithms described in Section 3.3 were tested on two Monte Carlo simulated samples:

- A *Partial* setup, which is a precise replica of that used during a data acquisition campaign at GSI, shown in Figure 4.1. The configuration consists in the complete upstream region (SC and BM), part of the tracking system (VT and MSD), the TW detector and one CALO module prototype. In this setup, the two permanent magnets are not present and the downstream region is placed at about 1.9 m from the target. In this case, a beam of ^{16}O ions at 400 MeV/u impinging on a 5 mm C target was simulated in order to be as close as possible to the experimental conditions. The total statistics generated for this setup was of $5 \cdot 10^6$ primaries on target.

- A *Full* setup, which includes all the detectors and the permanent magnets in their final nominal position, i.e. the one shown in Figure 3.17. Here, the downstream detectors were also shifted along the positive X axis to have the best possible geometrical acceptance compliant with the magnetic field bending. In particular, with the TW at 175 cm from the target, both downstream detectors had to be moved of 11 cm along the X axis. In this case, the beam was ^{12}C at 200 MeV/u on a 5 mm C target. In total, 10^7 primaries on target were generated for this configuration.

On the one hand, the simulation of the *Partial* setup had the main purpose of evaluating the reconstruction performance on straight tracks, i.e. with no magnetic field, constructed without one of the tracking stations, the IT. The accurate recreation of the experimental setup in the simulation was made in order to obtain a reconstruction efficiency which could mimic the experimental one of the data taking performed at the GSI laboratories. In particular, even though there is no possibility to measure the momentum

Figure 4.1: Scheme of the setup used during the experimental campaign at GSI and reproduced for the MC simulation of the *Partial* setup. The main differences with the *Full* setup of Figure 3.17 are the absence of the magnets and of the IT and the presence of only one 3x3 module of calorimeter.

of fragments in this case, particle tracking still serves as a fundamental tool to reconstruct the full event signature and to identify and remove the background generated by *out-of-target* fragmentation. These kind of events are mostly impossible to remove without tracking and their contribution has to be otherwise measured experimentally, through dedicated runs without target on the beam line.

On the other hand, the aim of the *Full* setup simulation was to estimate the current reconstruction efficiency and purity which could be expected during a full-system data acquisition. The presence of the magnetic field makes it also possible to actually evaluate the momentum of detected particles. In this sense, the *Full* setup simulation is also useful to estimate the momentum resolution that can be achieved by the tracking system.

4.1 Track reconstruction performance

The comparison of the different tracking algorithms depends on the definition of a set of quality parameters. For what concerns the reconstruction, very few constraints on track candidates were applied before the track fitting step. This choice was made with the explicit intent of limiting as much as possible the number of cuts at the reconstruction level, which makes it possible to evaluate the raw performance of all tracking algorithms and subsequently tune the event selection at a following step. The main request for all track candidates was to set a minimum number of points to proceed with the track fit. In particular, the choice was to require at least a point in about 70% of the available tracker planes, i.e. a minimum of 8 for the *Partial* setup ($n_{points,max} = 11$) and of 9 for the *Full* simulation ($n_{points,max} = 13-15$, depending if 2 or 4 IT planes are crossed by the particle). Every selected track candidate with less points was discarded before the track-fitting step. As a last requirement, tracks not containing a TW point were discarded as well. This choice was dictated by different reasons. First of all, tracks not hitting the TW simply fall outside the geometrical acceptance of FOOT, which means that they have to be discarded anyways from the reconstruction. Then, the absence of a TW point makes it impossible to actually retrieve the correct value of the charge and, thus, of the momentum. As a matter of fact, given a set of track points and a seed state, the global reconstruction fit returns a value for the rigidity p/Z of the particle. Without any information on the particle charge, it is impossible to reconstruct its momentum. Lastly, for some algorithms the information obtained from the TW point (i.e. TOF and Z) is crucial to both track extrapolation and seed state evaluation. In particular, the *Backtracking* algorithm strictly requires the

presence of the TW to construct its track candidates and begin the extrapolation to the other detectors of the setup. It is important to notice that, with such requirements, the particle track is also required to contain a set of points generated in at least 3 different detectors. This means that, for the *Partial* simulation, at least one point in the VT, MSD and TW is needed, while for the *Full* simulation all 3-detectors combination with the IT are also possible.

The first performance check performed on the different algorithms was the evaluation of their track reconstruction efficiency. To do so, a reference set of "good" tracks has been defined for both the *Partial* and *Full* MC simulations. The only requirements are that the corresponding particle has to be produced inside the target and it has to leave a signal in the geometrical acceptance of the TW. These, in principle, are the particle tracks that FOOT wants to fully reconstruct, while also removing as much as possible the background generated by *out-of-target* fragmentation reactions.

Considering a set of N_{ref} reference tracks, the efficiency of a tracking algorithm has been defined as

$$\varepsilon = \frac{N_{reco}}{N_{ref}} \tag{4.1}$$

where N_{reco} is the number of particle tracks that have been correctly identified and fitted by the Global Reconstruction. In this definition, a track is considered as correctly reconstructed if it satisfies two basic requirements:

- The Kalman Filter fit has fully converged, i.e. each intermediate state of the track is compatible with the model.
- The charge Z associated to the track is the same of the most frequent MC particle along the trajectory. This means that the majority of the clusters assigned to the track have to belong to the particle that reached the TW.

The errors on ε were calculated from the variance of a binomial distribution

$$\delta\varepsilon = \sqrt{\frac{\varepsilon\,(1-\varepsilon)}{N_{ref}}} \tag{4.2}$$

The efficiency can also be evaluated as a function of the reconstructed Z and angle of emission θ by changing N_{reco} and N_{ref} accordingly.

The results obtained for ε using the different tracking algorithms are shown in Figure 4.2. The track reconstruction efficiency is reported in the graphs as a function of the reconstructed charge Z.

A series of considerations can be made from these plots. First of all, the efficiency of the *TrueParticle* algorithm has been reported as a reference. Considering the definition of N_{reco}, there is only two ways in which the reconstruction could fail for this track selection strategy. On the one hand, if a particle is scattered at any point along the trajectory, there is a chance that the Kalman Filter fails to converge if the deflection is too high. However, this kind of effect has been estimated to introduce an inefficiency at maximum of about 2% for lighter fragments, meaning that it is not enough to explain a 10-35% difference between N_{reco} and N_{ref} with perfect reconstruction hypothesis. The only other source of inefficiency is then the charge identification. As described in Section 3.2, the *Z-match* logic employed in FOOT asks for very clean events where both TW bars of a crossing return the same Z. Given that both the energy and time resolution of the TW are included in MC simulation, a part of good TW points is necessarily cut by the

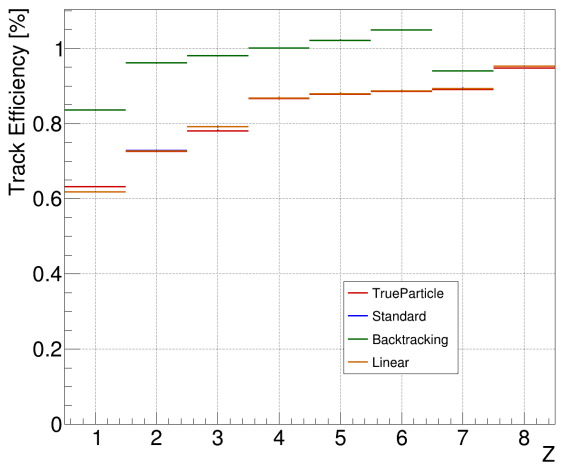

(a) *Partial* simulation

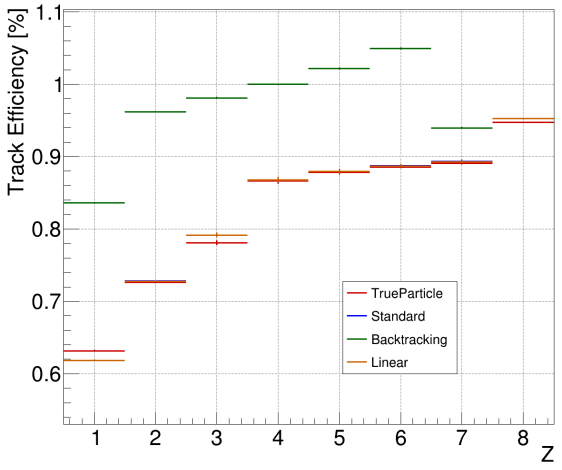

(b) *Partial* simulation, zoomed

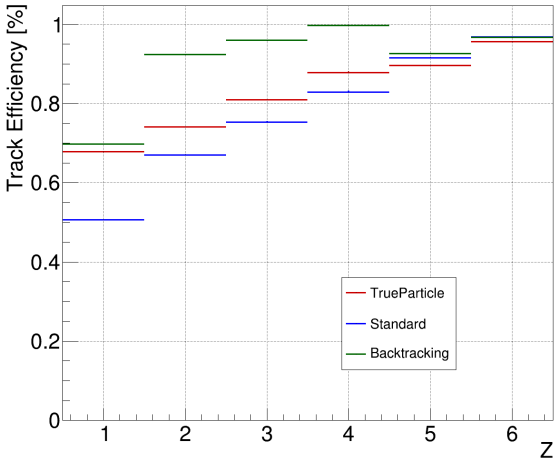

(c) *Full* simulation

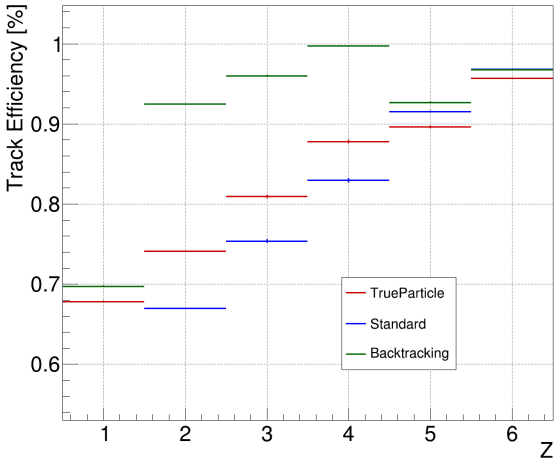

(d) *Full* simulation, zoomed

Figure 4.2: Global track reconstruction efficiency as a function of the charge Z measured from the TW for the different track selection algorithms: results for the (a) *Partial* and (c) *Full* setup simulation. Figures 4.2b and 4.2d report a zoom of Figures 4.2a and 4.2c, respectively. As for other following plots, the *Linear* algorithm is reported only for the *Partial* simulation, i.e. that with no magnetic field where it can actually be applied.

charge identification requirements. This means that the "*data-like*" algorithms have to be compared to the *TrueParticle* selection rather than considering their efficiency by itself. Anyhow it has to be noticed that the efficiency for both simulations is consistently above 80% for the "heavier" fragments observed in FOOT, i.e. for $Z \geq 3$, and becomes lower for lighter particles.

For what concerns the two forward tracking algorithms, the evaluated ε reported in Figure 4.2a indicates that both selections have an efficiency compatible with the *TrueParticle* when no magnetic field is present. This is a very promising result for further analysis of data acquired without the magnetic field since it indicates that, once the alignment and performance of detectors are under control, both forward tracking algorithms are already reliable for cross section evaluation. The efficiency of the *Standard* algorithm is instead slightly lower in the case of the *Full* simulation. This is likely due to the different impact of track seed hypothesis in the extrapolation and and fit of the track candidates. In fact, as stated in Section 3.3, the forward extrapolation of track candidates at the IT

is made through a linear interpolation, while the following steps are done using stronger assumptions on the rigidity of the track. When no magnetic field is present, the forward extrapolation is independent from the hypothesis on charge and momentum[2] and both algorithms successfully follow the straight tracks of nuclear fragments. The lowering of the efficiency in Figure 4.2c is then the consequence of the non-ideal hypothesis on particle mass and momentum used during the RKN extrapolation. This effect is significant at the moment since no information on particle mass from the CALO has been used, but it could be strongly reduced by associating the TW point with clusters in the calorimeter.

The *Backtracking* algorithm shows instead a behavior slightly more difficult to understand. The calculated efficiency is higher than the *TrueParticle* one for all Z and even reaches values over 1 for intermediate ions in both simulations. Since the number of reference tracks is always the same, this result indicates that there is some effect in the algorithm which enlarges the number of reconstructed tracks over the reference value.

Given the results obtained for the *Backtracking* selection, the following performance check that was carried out was the evaluation of the number of track clones reconstructed by each algorithm. If a particle m is described in the same event by $N_{m,reco}$ global tracks, the number of track clones is defined as

$$N_{m,clone} = \begin{cases} N_{m,reco} - 1 & \text{if } N_{m,reco} > 1 \\ 0 & \text{otherwise} \end{cases} \tag{4.3}$$

The particle m in this calculation has been chosen as the most frequent one along the track points, identified using the *MC-truth* information. A rate of track clones can also be defined as

$$R_{clone} = \frac{N_{clone}}{N_{ref}} = \frac{\sum_m N_{m,clone}}{N_{ref}} \tag{4.4}$$

The results concerning track cloning for all algorithms are reported in Figure 4.3 for both the *Partial* and *Full* simulation.

As it can be noticed from the plots, the *Backtracking* algorithm is, by far, the one that is more subject to track cloning, with values of R_{clone} reaching up to 30-40% of the reference MC tracks. These results can be understood from the track selection logic implemented, which is currently easily prone to cloning. As a matter of fact, on the one hand, the choice of a combinatorial approach in the first step of the selection increases the chance of seed tracklets containing the same TW point. On the other hand, the implemented non-exclusion logic in the back extrapolation makes it possible to assign the same clusters in the IT and VT to different tracks. This stems mainly from the fact that the extrapolation tolerances implemented for these two detectors have not being carefully optimized and have thus been purposely set to a large value (5 mm) to avoid losing track candidates in the backwards extrapolation step.

For what concerns the two forward track selection algorithms, the number of track clones is instead significantly lower. The track clone rate R_{clone} is of the order of 10^{-4} for the simulation without the magnetic field and of 10^{-3} for the *Full* setup, even without further cuts on the reconstruction. This means that, for these two algorithms, the contribution of track clones to particle yield evaluation is expected to be negligible or of the same order of statistical fluctuations. Nevertheless, a set of reasonable selection cuts to further reduce the impact of track cloning could also be applied, as for example removing track candidates which contain the same TW point.

[2]except for the evaluation of Multiple Scattering effects

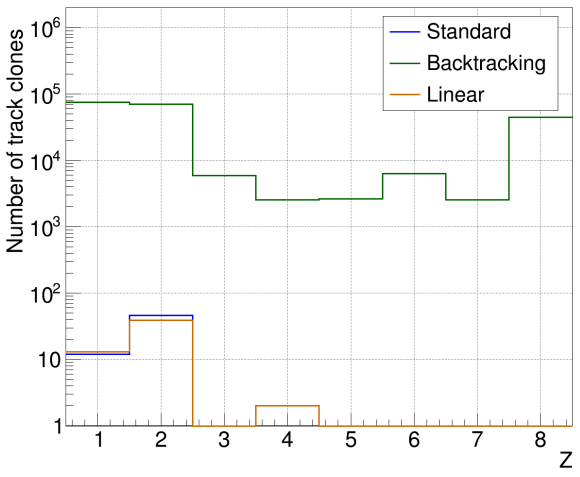

(a) N_{clone}: *Partial* simulation

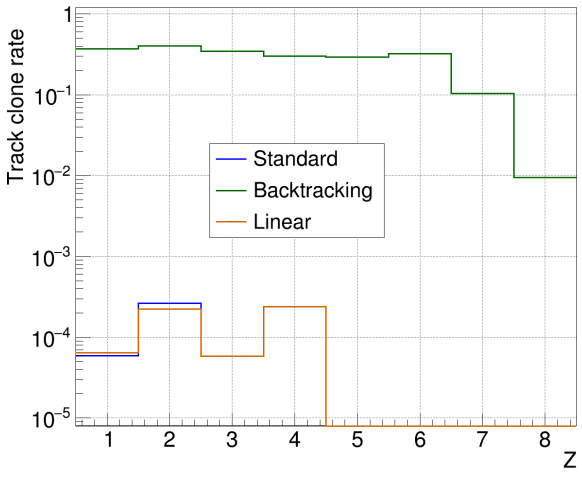

(b) R_{clone}: *Partial* simulation

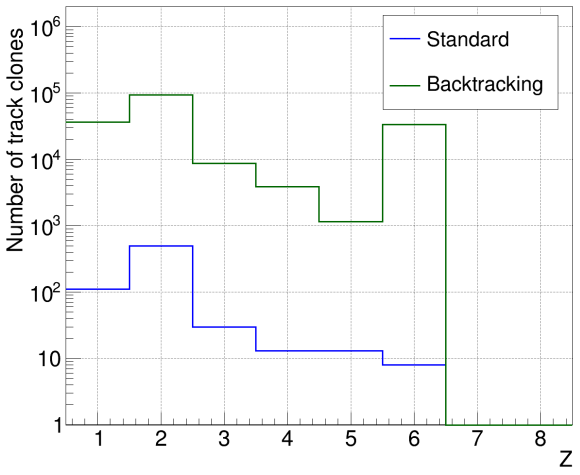

(c) N_{clone}: *Full* simulation

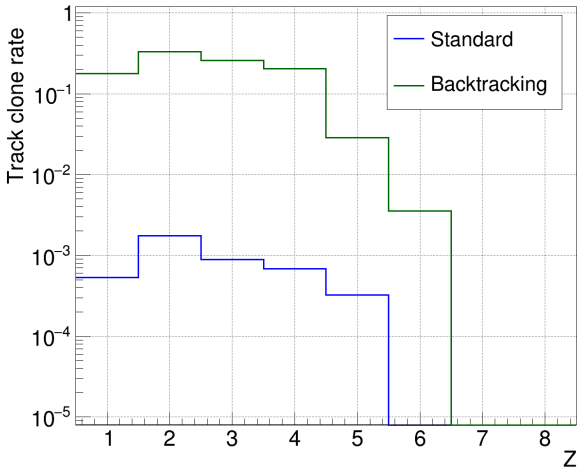

(d) R_{clone}: *Full* simulation

Figure 4.3: Global track clone number and rate as a function of the reconstructed charge Z for the different tracking algorithms. The first row of plots refers to the *Partial* simulation, while the second row is relative to the *Full* setup simulation. Here, the *TrueParticle* selection is not reported since it is not affected by track cloning.

The impact of track mis-association and cloning can be also evaluated through the definition of a quality parameter for particle tracks. The *quality* Q of a reconstructed global track has been defined as

$$Q = \frac{n_{mfp}}{n_{tot}} \tag{4.5}$$

where n_{tot} is the total number of points in the track and n_{mfp} is the number of points that belong to the most frequent particle in the track. It represents the efficiency of the pattern recognition steps, since a track with $Q < 1$ surely contains a certain degree of mixing, i.e. points generated by different particles. The track quality obtained for all selection algorithms in both simulations is reported in Figure 4.4.

In both plots the *TrueParticle* algorithm only reconstructs tracks with $Q = 1$ as expected, indicating that it has been correctly implemented. It is also quite evident that all data-like algorithms are instead affected by a certain degree of mixing in the selection phase, which is easily understandable considering the high extrapolation tolerances em-

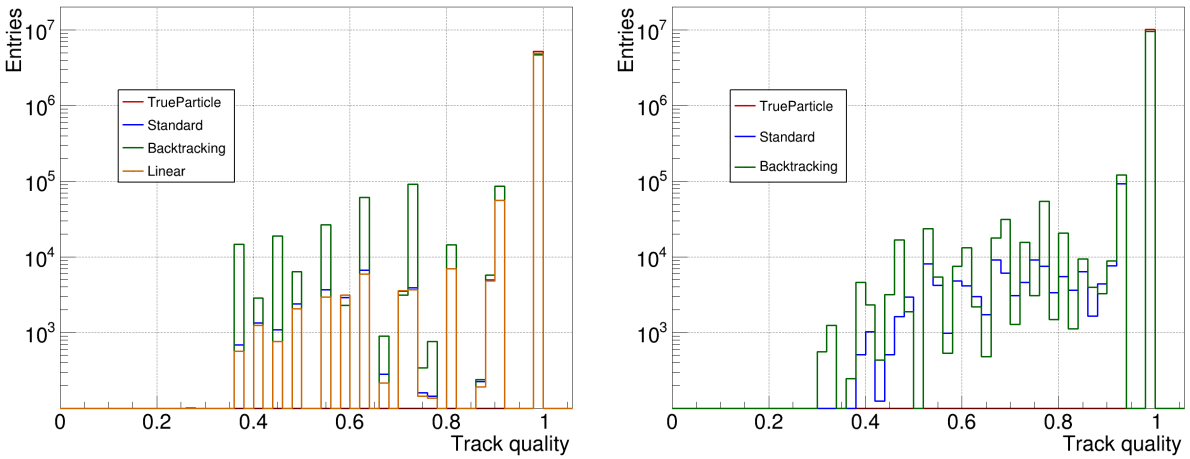

(a) *Partial* simulation (b) *Full* simulation

Figure 4.4: Global track quality obtained with different tracking algorithms for the (a) *Partial* and (b) *Full* simulation.

ployed so far. The *Backtracking* algorithm seems to be the one that identifies the highest number of tracks with $Q < 1$, while the *Linear* and *Standard* selections perform in a similar manner. The first effect is likely caused by the combinatorial approach chosen for the TW-MSD track candidates construction and by the total absence, as of now, of cuts applied on the reconstructed tracks. The similarities in the *Standard* and *Linear* algorithms is due to the absence of the magnetic field and the fact that both selections use the VT tracklets as the seed for the forward extrapolation. For what concerns the *Full* simulation, at this stage the forward tracking algorithm seems to perform slightly better than the *Backtracking* approach. This is due to the higher granularity of the VT with respect to the MSD and TW, which guarantees a lower probability of track mixing in the creation of seed tracklets at the beginning of each selection algorithm.

The results shown in this section, summarized in Table 4.1, indicate that the *Backtracking* algorithm is currently not optimized enough to perform further analysis. As a matter of fact, the rate of track clones is currently very high leading also to non-physical values for the reconstruction efficiency. Anyhow, this is understandable since the *Backtracking* is the algorithm which was developed last and it yet needs to be optimized.

On the contrary, the *Standard* and *Linear* algorithms are less affected by track cloning and mixing, meaning that they provide more reliable results. Their performance in terms of efficiency, clone rate and track quality are compatible within the statistical uncertainties for the *Partial* setup simulation, which means that they could be also employed for the evaluation of systematic effects on experimental data analysis.

4.2 Momentum reconstruction performance

As said before, the *Full* setup simulation made it also possible to perform a study on the expected momentum reconstruction performance. The fit of particle tracks makes it possible to evaluate the momentum at each position along the track. For what concerns FOOT measurements, the most important information is the momentum of the particle at the vertex of the fragmentation reaction, i.e. the target.

The momentum resolution of the FOOT global reconstruction has been evaluated by

	Algorithm	$\overline{\varepsilon}$ [%]	$\overline{R}_{clone}$ [%]	$\overline{Q}$ [%]	$Q \neq 1$ [%]
***Partial* setup**	*TrueParticle*	73.35(6)	0	100	0
	Standard	73.14(6)	0.009(2)	99.64(4)	1.911(6)
	Backtracking	98.65(2)	32.0(1)	98.06(4)	6.68(1)
	Linear	72.12(6)	0.009(2)	99.67(4)	1.864(6)
***Full* setup**	*TrueParticle*	75.60(6)	0	100	0
	Standard	68.12(6)	0.079(4)	99.61(3)	2.034(5)
	Backtracking	95.15(2)	14.81(6)	99.09(3)	3.811(6)

Table 4.1: Summary of the FOOT Global Reconstruction performance for different tracking algorithms. The tracking efficiency and clone rate are reported here as integral values averaged over all charges lower than the primary. The track quality is averaged over all tracks (primaries included) and the percentage of tracks with quality lower than 1 is also reported in the last column of the table. All values in the table are reported as percentage for better clarity. The errors on the calculated values are reported inside the round brackets and refer to the uncertainty on the last digits.

comparing the reconstructed value p_{reco} to the *true* one from MC p_{MC}, both evaluated at the target

$$\frac{\Delta p}{p} = \frac{p_{reco} - p_{MC}}{p_{MC}} \tag{4.6}$$

For each different ion specie, $\Delta p/p$ was plotted as a function of particle momentum and the resulting distributions were fitted with a Gaussian function to extract their mean μ and standard deviation σ, with this latter representing the actual momentum resolution. The obtained results are reported in Figure 4.5.

As it can be noticed, the momentum resolution (Figures 4.5b, 4.5d and 4.5f) sets around 2.5% for all tracking algorithms in the whole energy range of the simulation, with a slight worsening at lower values of p. The resolution calculated with this method is much better than the one required by the design of the experiment (around 4-5%), meaning that the system could potentially be more precise than expected. The momentum resolutions obtained with the perfect track selection (*TrueParticle*) and both "data-like" algorithms are in good agreement over the whole energy range, indicating that the global reconstruction can maintain such precision also on real data. This is of utmost importance when considering the need for a solid and accurate mass identification.

It has to be also pointed out that, at the moment, the global reconstruction seems to slightly overestimate the reconstructed momentum of the particles by a factor between 0.5 and 1% of the "true" value. This issue is present also in the tracks obtained with the *TrueParticle* selection algorithm (Figure 4.5a), which starts with perfect reconstruction hypothesis. This means that the overestimation does not depend on the track selection algorithm, but more on the track fit itself or on the extrapolation of the track parameters at the target. This systematic shift has to be further investigated, but it is important to notice that the effect is compatible with zero when considering the evaluated momentum resolution of the spectrometer.

The reconstructed momentum can also be combined with the TOF information from the TW point to calculate the mass of the detected particle. A direct application of

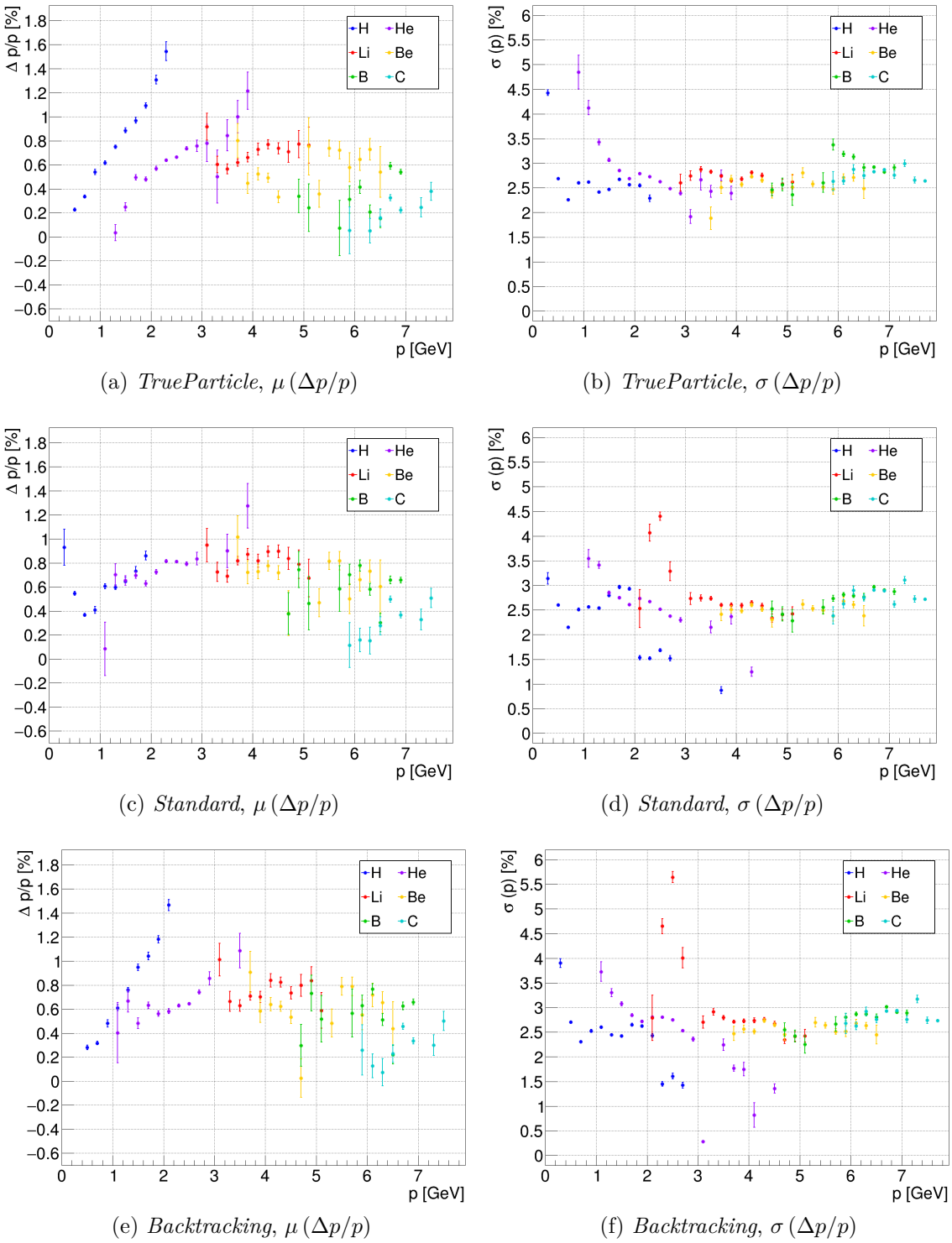

(a) *TrueParticle*, $\mu\,(\Delta p/p)$ (b) *TrueParticle*, $\sigma\,(\Delta p/p)$

(c) *Standard*, $\mu\,(\Delta p/p)$ (d) *Standard*, $\sigma\,(\Delta p/p)$

(e) *Backtracking*, $\mu\,(\Delta p/p)$ (f) *Backtracking*, $\sigma\,(\Delta p/p)$

Figure 4.5: Momentum evaluation performance of different Global reconstruction algorithms. The graphs show the mean and standard deviation values of the $\Delta p/p$ distributions calculated with Equation 4.6 for different reconstruction algorithms: (a) and (b) *TrueParticle*, (c) and (d) *Standard*, (e) and (f) *Backtracking*. The errors reported in the different graphs are those of the Gaussian fit parameters of each $\Delta p/p$ distributions.

Equation 2.10 to all reconstructed tracks leads to the results reported in Figure 4.6. The first important result that can be inferred from these plots is that the current *TOF* and

p reconstruction performance of FOOT seem good enough to identify the mass of nuclear fragments. As a matter of fact, it is possible to distinguish the peaks generated by different isotopes for all Z observed. As expected, the separation between different isotopes gets slightly worse with increasing mass, even if the p resolution is approximately constant and the TOF gets more precise for heavy ions. This is because the relative mass difference between isotopes decreases for heavier nuclei. As an example, the relative mass separation between ^{1}H and ^{2}H is $\sim 100\%$, while between ^{10}B and ^{11}B there is only a $\sim 9\%$ difference. However, the only ion for which the isotopic structures are not visible is the impinging beam, i.e. C, where the signal is strongly dominated by primaries.

The spectra reported in Figure 4.6 show a slight overestimation of the reconstructed mass number. This effect is likely due to the overestimation of p, which has a double impact on the mass calculation with Equation 2.10. As a matter of fact, a change in p leads to a different bending of the particle trajectory, i.e. a different flight path between target and TW. In particular, an overestimation of p leads to a higher track rigidity, which reflects in a shorter flight path and, thus, an underestimation of the β and γ factors. The cause of this effect is currently being investigated, but it is important to notice that the observed shift is compatible with the expected experimental resolution of FOOT. Moreover, this mass measurement is only one of the possible that FOOT can perform, as described in Section 2.2. Once the information on kinetic energy coming from the CALO will be combined with p and TOF, the isotopic identification will improve further.

It can also be noticed that the mass spectra reconstructed using "data-like" algorithms are mainly affected by two different background components. The first one is clearly visible in the *Backtracking* spectra and leads to an increase of the counts in the whole mass range. This is likely caused by the high number of track clones present in the selection algorithm at the current state, which can determine a wrong $p - TOF$ association in several ways. In general, track cloning is more significant at lower Z values. As a matter of fact, a lower Z associated to a track also translates in higher tolerances for Multiple Scattering effects in the Kalman Filter, meaning that the fit is more likely to converge even when there is some degree of cluster mis-association.

The second background component, visible in both "data-like" algorithms, instead only affects the spectra around $A/Z \simeq 2$, i.e. the mass to atomic number ratio of the primary. This type of background is generated by the physics of out-of-target fragmentation reactions. As already stated in Section 1.2.3, projectile fragments are normally emitted in the forward direction and retain a high percentage of the velocity of the primary particle. Let us suppose that a primary ^{12}C nucleus fragments in the air between the MSD and the TW, generating a ^{9}Be and an ^{3}He as sketched in Figure 4.7. With such cluster placement, the selection algorithm will create one track containing all the points from the primary, plus the TW point of the ^{9}Be. The reconstructed rigidity of this track will be approximately the same as that of a non-fragmented primary track, which has $A/Z = 2$. Since the charge is evaluated through the TW point and, for a fixed β, we have that $p/Z \propto m/Z \simeq A/Z$, the track will be wrongly reconstructed with the momentum of a ^{8}Be nucleus. This is compatible with what is shown in Figure 4.6d and also explains the presence of the same effect for $Z = 5$. Another indication that the excess counts at $A/Z \simeq 2$ are the consequence of out of target fragmentations is given by their decreasing impact at lower Z values. As a matter of fact, the emission of heavier fragments is mostly forward peaked, while lighter ejectiles have a broader angular (and energy) distribution. This means that it is much more likely to have a fragment with $Z > 2$ follow the trajectory of the primary particle within the forward extrapolation tolerances.

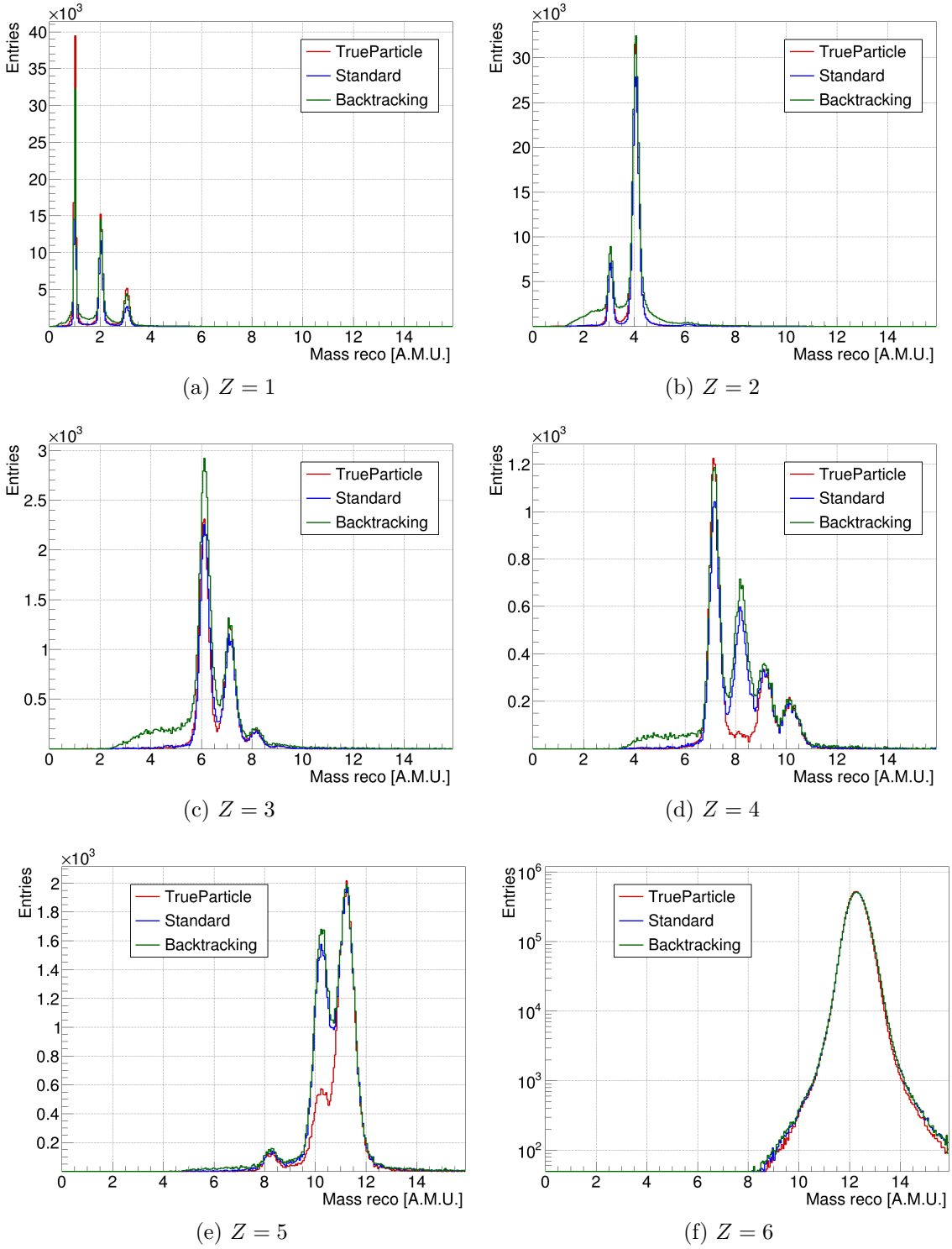

(a) $Z = 1$ (b) $Z = 2$

(c) $Z = 3$ (d) $Z = 4$

(e) $Z = 5$ (f) $Z = 6$

Figure 4.6: Reconstructed mass spectra for all different Z values: simulation of ^{12}C beam at 200 MeV/u on a 5mm C target with the *Full* setup of FOOT. The plot for $Z = 6$ is reported in logarithmic scale because of the much higher statistics given by non-fragmented primary ions.

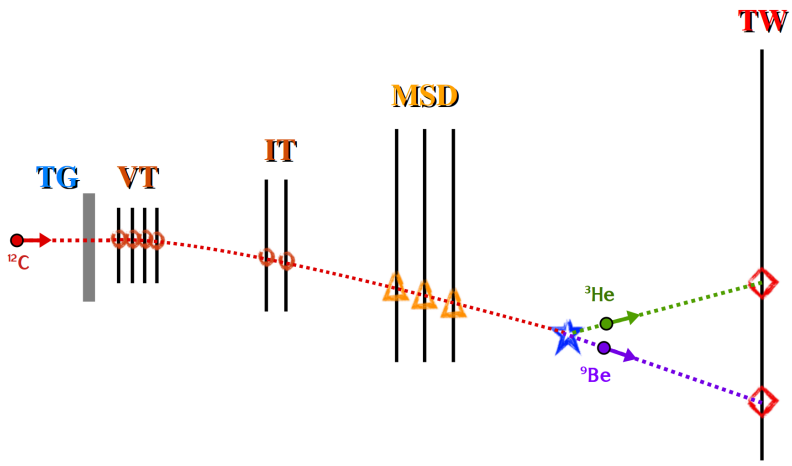

Figure 4.7: Example of event with fragmentation reaction happening out of target. The trajectories of all particles and the points they leave along the tracker are shown with different colors. The Global Reconstruction selection algorithms in such event will select the trajectory followed by the ^{12}C and then the TW point created by the ^{9}Be fragment.

4.3 Event selection

As indicated by the previous results, the background generated by out-of-target fragmentation reactions is one the most significant in FOOT. The components of the magnetic spectrometer were designed with the aim of minimizing the amount of material crossed by the fragments. However, estimates based on MC simulations indicate that the number of fragmentation reactions happening out-of-target can reach up to 25% of those inside the target. This means that such kind of events can still strongly impact the results of the Global Reconstruction and, thus, of cross section measurements.

The performance reported in the previous sections indicate that all tracking algorithms are subject to a certain degree of background and cloning. At present, the most reliable approaches seem to be the two based on forward extrapolation, i.e. the *Standard* and *Linear* algorithms. As a matter of fact, the impact of track cloning and mixing effects is still non-negligible for the *Backtracking* selection, meaning that it needs to be further optimized before employing it in tracking analysis for cross section evaluation. Since the *Standard* selection is the only forward tracking that can be applied to both the simulations under study, it will be the algorithm utilized in all the following studies.

In general, an event selection cut has the purpose to improve the *purity* of a sample. In the case of FOOT Global Reconstruction, the purity ϱ has been defined as the fraction of particle tracks where the reconstructed charge Z matches that of the most frequent particle Z_{mfp}. Following the same approach used for the calculation of efficiency, we have

$$\varrho(Z) = \frac{N_{reco}(Z = Z_{mfp})}{N_{reco}(Z)} \tag{4.7}$$

and the corresponding error

$$\delta\varrho(Z) = \sqrt{\frac{\varrho(Z)\left[1 - \varrho(Z)\right]}{N_{reco}(Z)}} \tag{4.8}$$

The purity thus calculated gives a measurement of how many of the reconstructed tracks can be considered as "good" during the analysis. By definition, any chance of increasing

the purity using an event selection cut will also lead to a decrease of the track reconstruction efficiency. The goal is to determine a set of reasonable selection cuts which constitute a good trade-off between increasing ϱ and decreasing ε.

The first cut was defined in terms of χ^2 of the Kalman Filter fit. Since the number of degrees of freedom for the fit varies with the number of points along the track, the best choice was to define a cut based on the p-value of the fit. Here, the p-value is the standard right-tail probability of the χ^2 distribution, i.e. the probability of observing a χ^2 value that is higher than the measured one. In our case, we chose to select only tracks with a p-value > 0.01, which corresponds to $\chi^2/n.d.o.f. \lesssim 2$, and the corresponding cut will be addressed as "χ^2" cut.

Another requirement was set on the number of global tracks reconstructed in each event. Since FOOT focuses on fragmentation reactions, one can expect that most of the "interesting" events contain more than one track in the setup. To follow this claim, an additional cut was applied on the reconstructed events by requesting the presence of more than one global track. This cut is indicated in the following plots as "MT" or "*Multi-Track*".

One of the background components that was previously pointed out is that given by pile-up in the TW detector. The events in which the charge identification fails because of pile-up (see Figure 3.14) can be removed by requesting that each reconstructed track contains a different TW point. The recognition of such events is possible because of the higher granularity of the trackers with respect to the TW, which makes the silicon detectors much less subject to pile-up. With this request, every time two global tracks are extrapolated to the same TW point, they are both discarded by the selection. The corresponding cut will be addressed as "PU" or "*Pile-Up*" in the following.

The last requirement applied during event selection was to ask for a perfect matching between the number of reconstructed global tracks and TW points in the event. The aim of this additional request is to avoid any possible instance where both an in-target fragmentation and an out-of-target fragmentation happen in the same event. Let's suppose for example that an ^{16}O primary undergoes a nuclear interaction in the target producing a ^{12}C and a ^{4}He ion. If the ^{4}He remains in the acceptance of the setup and the ^{12}C follows a path like the one shown in Figure 4.7, it is possible to reconstruct two global tracks passing all the previous selection cuts, with one of them containing an out-of-target fragmentation. The request for the same number of global tracks and TW points is able to identify such events and remove them. This cut will be indicated as "TW match".

To assess the performance of each of these cuts, the first check performed was focused on two aspects. On the one hand, the *charge migration matrix (CMM)* of the reconstructed global tracks was studied. The CMM correlates the measured Z of a fitted track (Z_{reco}) with that of the most frequent particle along the trajectory (Z_{mfp}). Ideally, the CMM should be as close as possible to a diagonal matrix, which indicates the events where the reconstructed charge matches the MC one. On the other hand, the MC truth information was used to extract the z coordinate of origin of the particles generating the TW point of each track. This quantity is very important to keep track of the background contribution given by out of target fragmentations. The CMMs and z-coordinate plots obtained for the *Partial* and *Full* simulation after the application of the different event selection cuts (one after the other) are reported in Figure 4.8 and 4.9, respectively.

As it can be seen from Figure 4.8a and 4.9a, the CMMs of all reconstructed tracks before the selection cuts contain a significant number of events out of the diagonal. In particular, there is a very evident background in the first row of the CMM, where the

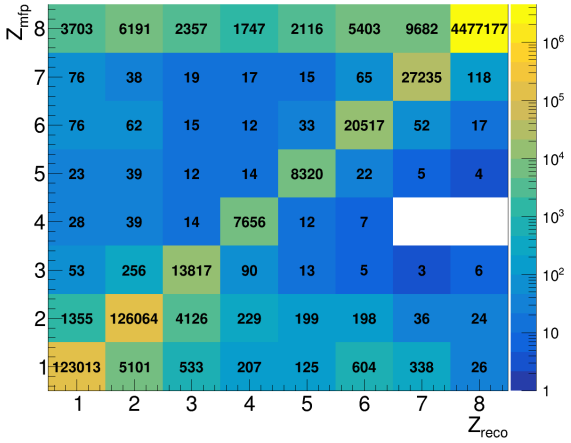

(a) All

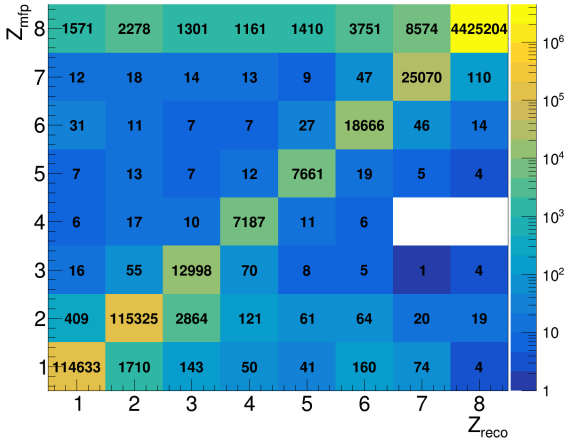

(b) χ^2-cut

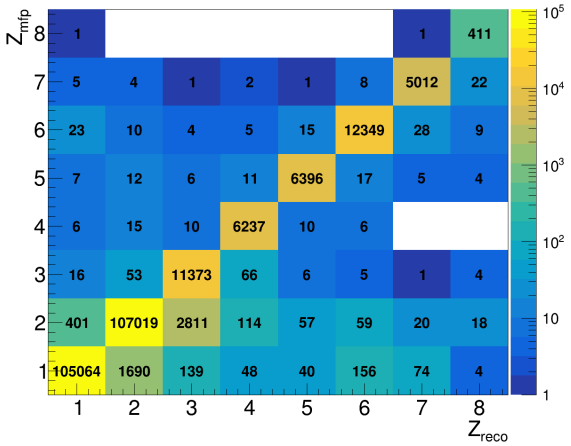

(c) MultiTrack cut

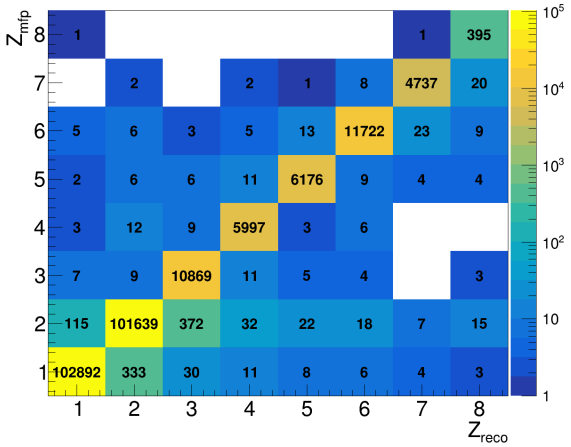

(d) Pile-up cut

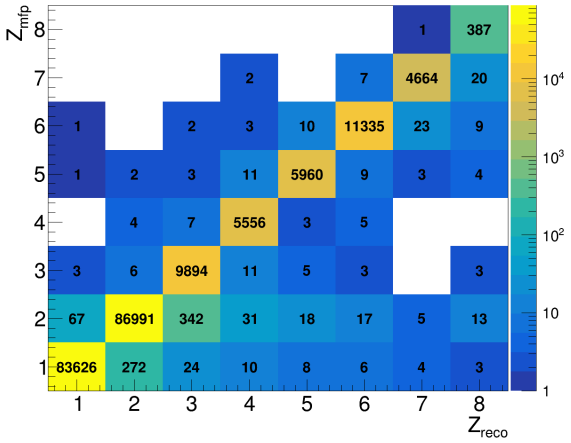

(e) TW match

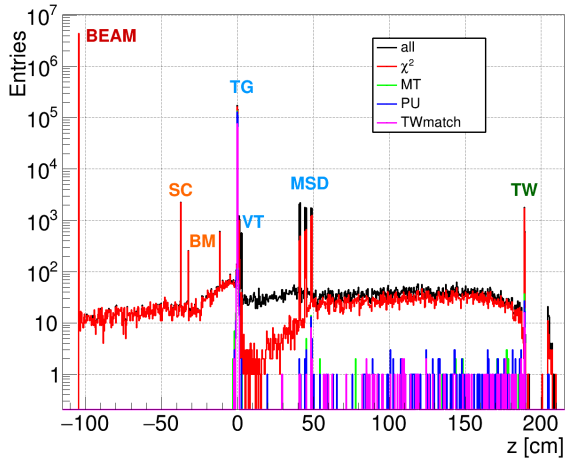

(f) Particle origin position

Figure 4.8: (a) to (e): Charge mixing matrix for the reconstructed global tracks in the *Partial* setup simulation for all different event selection cuts applied sequentially. (f): z-coordinate of origin of the particles generating the TW points in the global tracks. The position of each detector along the setup is also reported.

most frequent particle is the primary ion but the TW point reconstructs a lower charge. Except for $Z_{reco} = 7$ where a part of the counts is given by charge mis-identification,

this is the clear signature of out-of-target fragmentation events. It is also possible to notice that there is a non negligible contribution out of the diagonal for $Z \leq 3$, where the probability of track mixing and TW pile-up become more significant. The contribution given by out of target fragmentations is also evident in Figure 4.8f and 4.9f. In both plots, the two highest peaks, one at the most negative z and one at $z = 0$, are those relative to the primary beam generation point and the in-target interactions, respectively. All the counts outside of these two regions come from out of target fragmentations in either the detectors or in the surrounding air[3]. It can also be noticed that there is a contribution coming from fragments generated before the target

The application of the χ^2 cut (Figures 4.8b and 4.9b) leads to a reduction of the counts on the diagonal of the CMM of about 10-15% but has a more significant impact on the out of diagonal tracks, even up to 90% in some case. This means that it already leads to an improvement of the signal to noise ratio in the CMM. For what concerns the z-coordinate, the χ^2 cut contributes in removing part of the fragmentation in the first portion of the spectrometer, with a less significant effect after the MSD.

The first very strong difference is achieved with the MT cut. This request cancels the out of diagonal contribution on the first row of the CMM (see Figures 4.8c and 4.9c), basically removing the out-of-target fragmentations of the primary ion. This is easily understandable when considering the logic of the *Standard* selection algorithm. As a matter of fact, any event as the one shown in Figure 4.7 contains only one tracklet in the VT, implying that it is impossible to reconstruct more than one global track. This cut comes also with the drawback of removing a significant portion of the counts for heavier fragments. However, if the fraction of matched tracks is known and under control, it is possible to evaluate the relative track reconstruction efficiency and retrieve the real counts. The improvement in background rejection after this cut is also visible in Figure 4.8f and 4.9f. Here, the contribution from pre-target reactions is completely removed and the number of events coming from fragmentation in air or detectors after the target is significantly reduced.

It has to be pointed out that the MT cut necessarily leads to the removal of some reactions of interest. In fact, in-target fragmentations which emit only one fragment in the geometrical acceptance of the whole spectrometer are very likely to be removed by the MT request. This is because partial tracks in the spectrometer are either not recognized as global tracks by the algorithm or discarded by the request of a minimum number of points. For the physics cases explored in FOOT, the conservation of charge and baryonic number implies that the production of heavier fragments ($Z > 4$) is necessarily coupled to an emission of lighter fragments. The former have a narrow angular distribution and are likely to travel through the whole setup. The latter have a much wider angular and energy distribution, meaning that they can exit the spectrometer at any point, especially when the magnetic field is present. With these considerations, it is easy to understand how the number of heavier fragment tracks is significantly suppressed after the MT cut. The MT request is very efficient for background removal, but further studies will be performed to define a selection cut with lower impact on in-target fragmentation reactions.

The following cut applied is the PU, which strongly lowers the charge mixing at $Z \leq 3$ with almost no impact on the number of counts on the diagonal of the CMM. As an example, events of the type shown in Figure 3.14b, i.e. with $Z_{mfp} = 2$ and $Z_{reco} = 3$, are reduced by 75-80% in both setups. This indicates that the cut behaves as expected, removing most of the events where there is pile-up in a TW point.

[3]The two peaks around the BM correspond to the two mylar windows of the drift chamber.

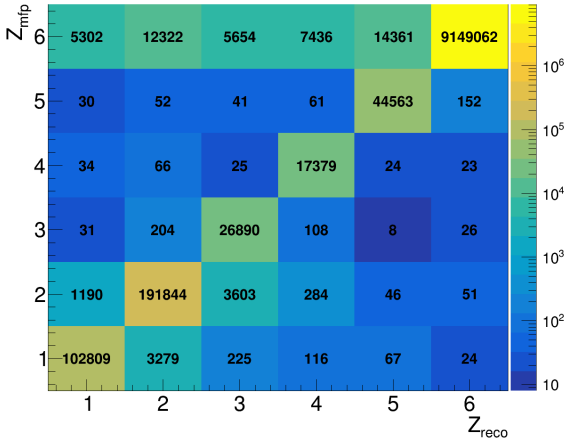

(a) All

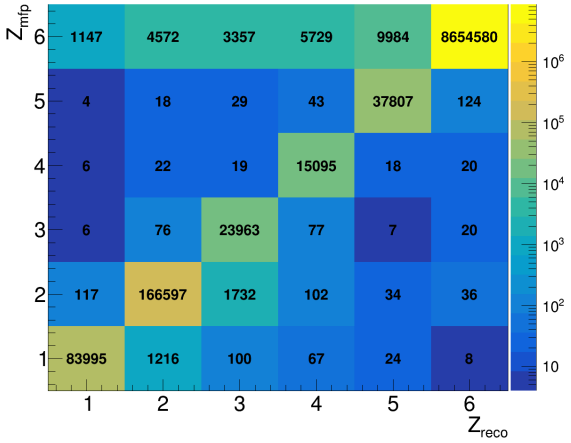

(b) χ^2-cut

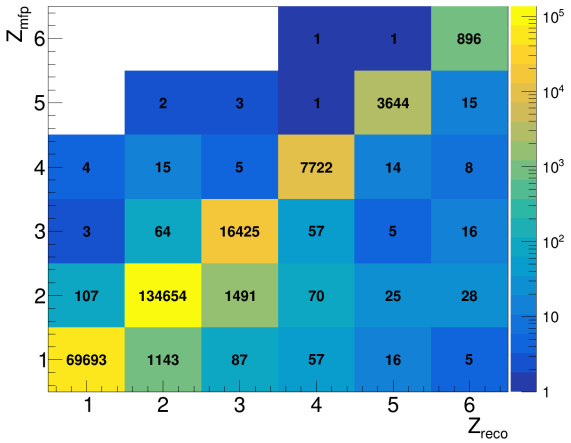

(c) MultiTrack cut

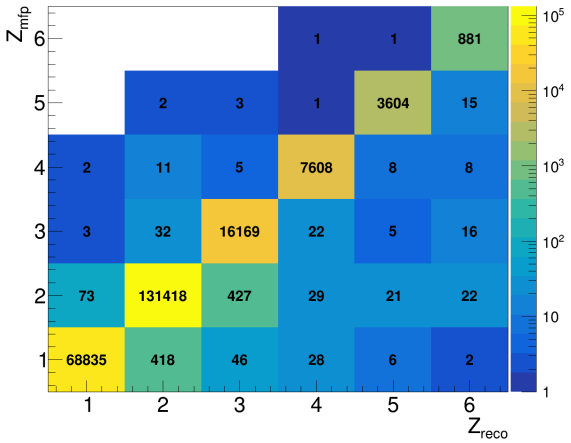

(d) Pile-up cut

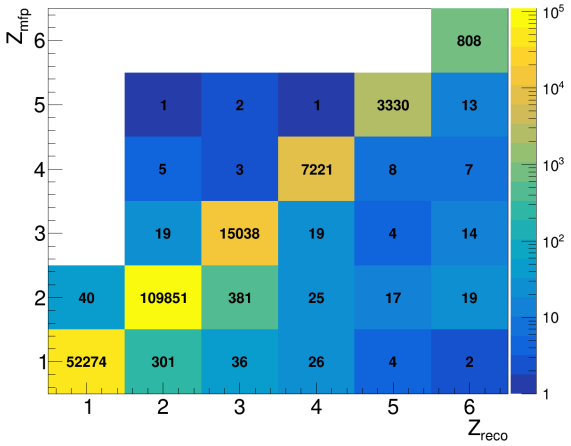

(e) TW match

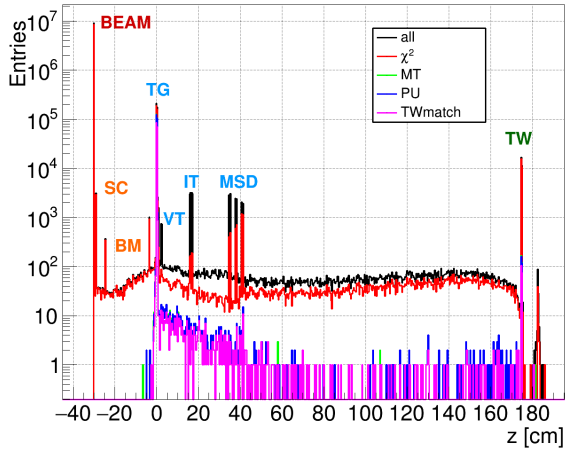

(f) Particle origin position

Figure 4.9: (a) to (e): Charge mixing matrix for the reconstructed global tracks in the *Full* setup simulation for all different event selection cuts applied sequentially. (f): z-coordinate of origin of the particles generating the TW points in the global tracks. The position of each detector along the setup is also reported.

Lastly, the application of the "TW match" condition leads to an additional lowering of the out of diagonal counts, mainly affecting the region where $Z_{mfp} > Z_{reco}$. However,

this request leads also to a non negligible loss of signal also in the diagonal of the CMM for $Z \leq 2$ and there is no clear gain in the signal to noise ratio at this stage. This means that such request has to be treated with more care and further evaluate its usage for cross section evaluation.

The next step for the study of our selection cuts was the evaluation of their impact on the track reconstruction efficiency and purity. Both of these quantities were evaluated for the two simulations as a function of Z and of the fragment emission angle θ. This latter was evaluated as the polar angle between the reconstructed global track and the primary ion track extracted by the Beam Monitor detector in the corresponding event. The direction of the global track was evaluated at the vertex of the fragmentation interaction inside the target calculated by the VT detector.

The integral and differential track reconstruction efficiency obtained as a function of the different cuts for the two simulations is reported in Figure 4.10 and 4.11. All the differential plots are reported up to 10°, which matches approximately the angular acceptance of the TW detector. As expected, every additional cut lowers the value of ε, with the *Multi-Track* request having the strongest impact on the heavier fragments of each simulation. The different ranges of $\varepsilon(\theta)$ as a function of Z are given by the angular distribution of the corresponding fragments. The differential efficiency for primary particles is not reported since all the cuts have the aim of also removing events without fragmentation.

The integral and differential track purity as a function of the different cuts is reported in Figure 4.12 and 4.13. The plots of primary particles are not reported for the same reason just explained for track reconstruction efficiency. The results show that, even if the track efficiency gets significantly lowered by the selection, the value of ϱ strongly improves with each applied cut. The track purity evaluated without any event selection clearly shows a strong reduction at low angles. This is again due to the out of target fragmentation reactions. As a matter of fact, for such events the track angle is expected to be very close to zero since there is no interaction in the target but $Z_{mfp} \neq Z_{reco}$. Here, the event selection cuts completely remove this contribution, leading to a purity always above 95% for all Z in their respective angular range. The purity seems to slightly lower for heavier fragments at wider angles, where the statistics is strongly suppressed. The only fragment that shows a wider angular range where the purity is further from 1 is the Li, which is the ion mostly affected by pile-up in the TW points due to the high yield of He fragments. This is also compatible with the strong improvement in the track purity of Li fragments given by the "PU" cut, as shown in Figure 4.12d and 4.13d.

One of the most important conclusions that can be drawn from these plots is that the described event selection cuts are able to effectively clean the sample of reconstructed tracks, removing most of the background induced by out-of-target fragmentations or any other interaction of no interest for FOOT measurements. This has significant implications also on the organization of future data acquisition campaigns of the Collaboration. As a matter of fact, the beam time available for FOOT in different facilities is limited and only very few acquisition campaigns can be scheduled each year. Up to now, a non negligible portion of the beam time of each campaign had to be dedicated to the characterization of background coming from out-of-target fragmentations, which was carried out removing the target from the beam line. This allows for direct subtraction of the background but, at the same time, requires a significant time allocation to limit as much as possible the statistical fluctuations in the results. Even though no-target runs will always be carried out for calibration and alignment purposes, the FOOT Global Reconstruction, paired

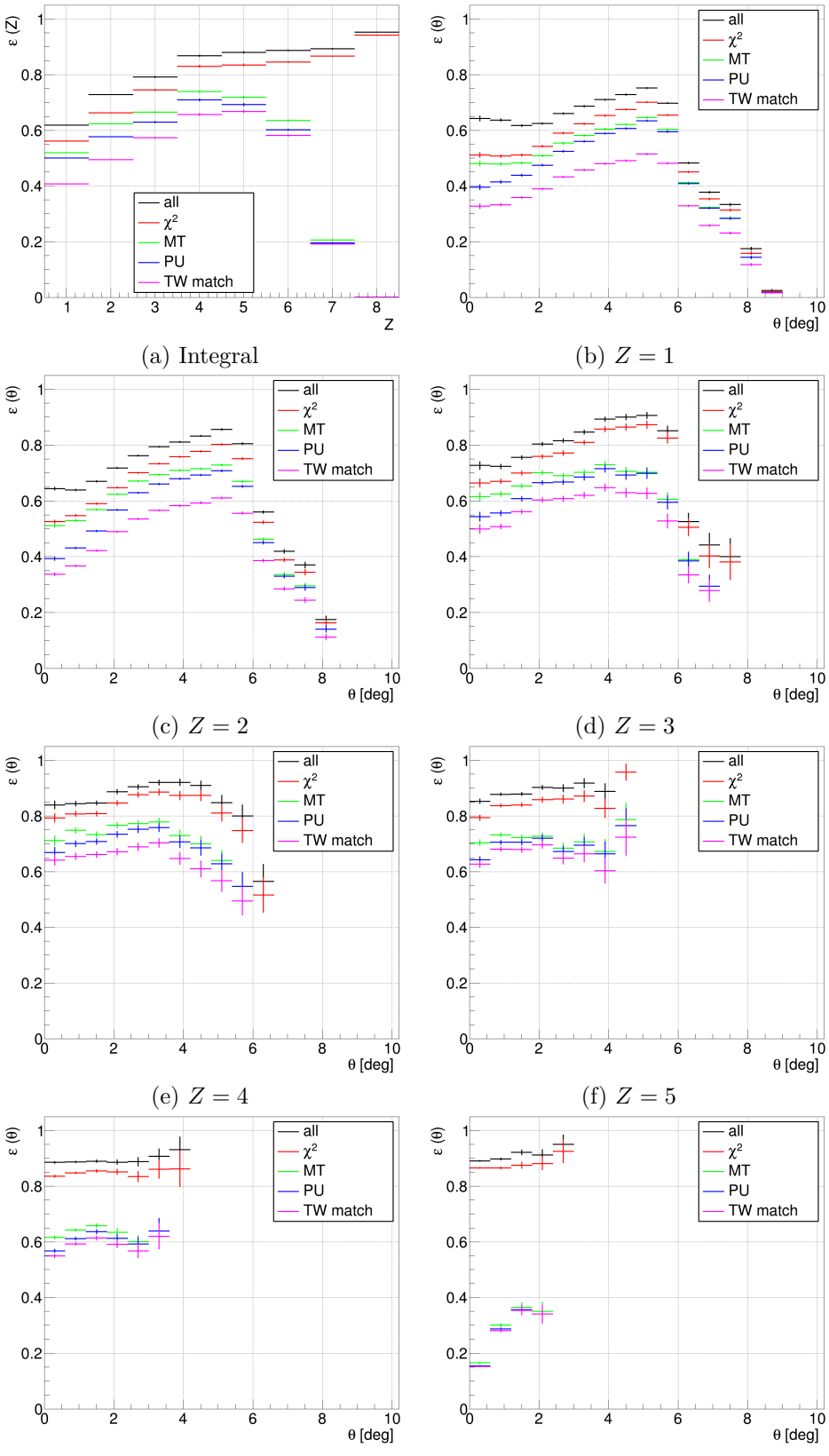

(a) Integral (b) $Z = 1$

(c) $Z = 2$ (d) $Z = 3$

(e) $Z = 4$ (f) $Z = 5$

(g) $Z = 6$ (h) $Z = 7$

Figure 4.10: Total and angular track reconstruction efficiency for the *Partial* setup divided by Z. It is possible to see the effect of all the different event selection cuts applied.

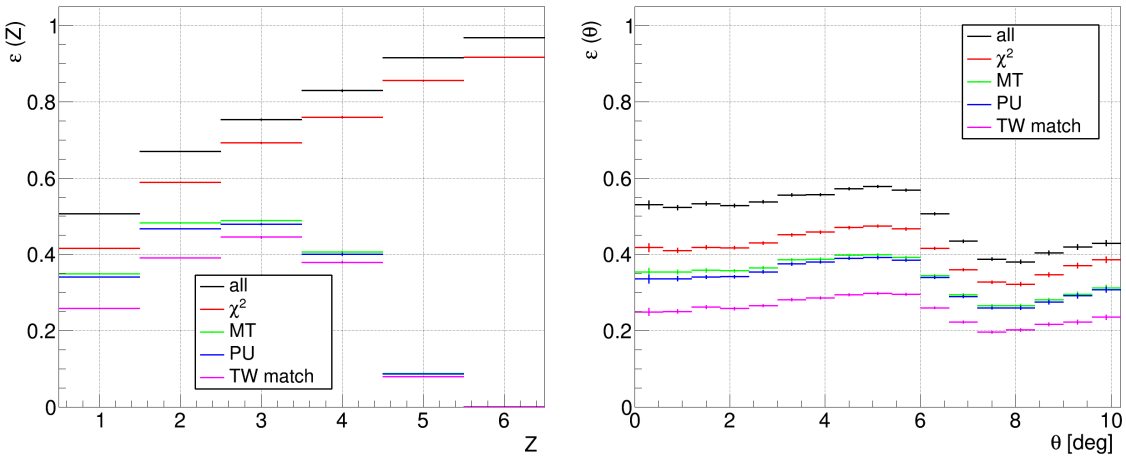

(a) Integral

(b) $Z = 1$

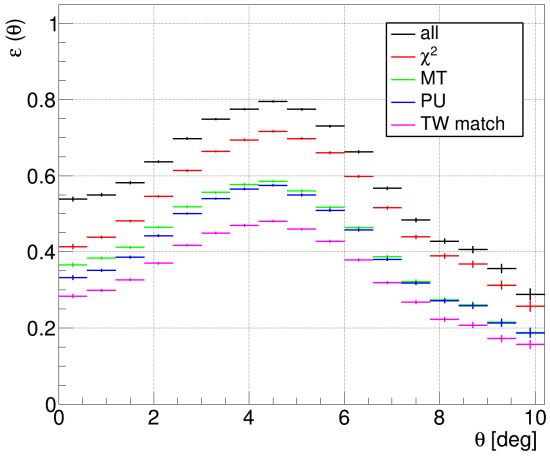

(c) $Z = 2$

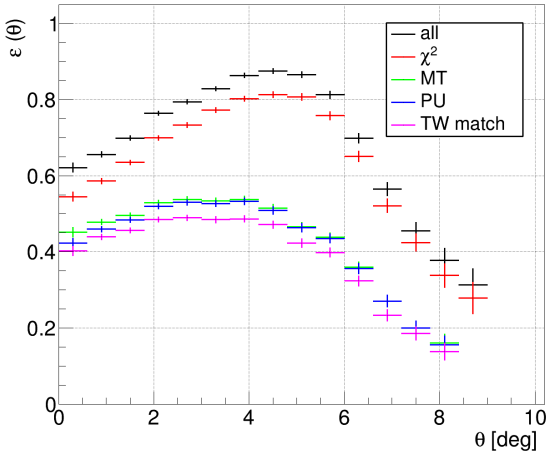

(d) $Z = 3$

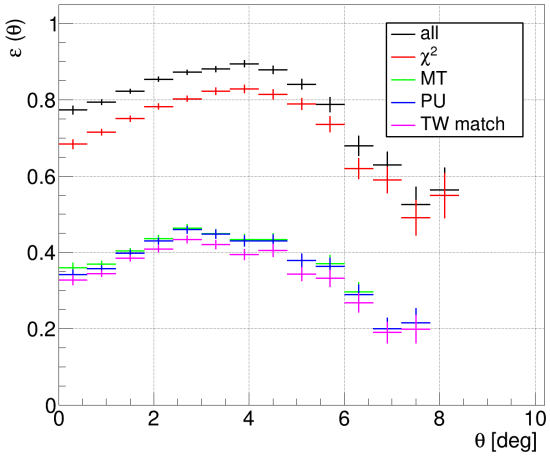

(e) $Z = 4$

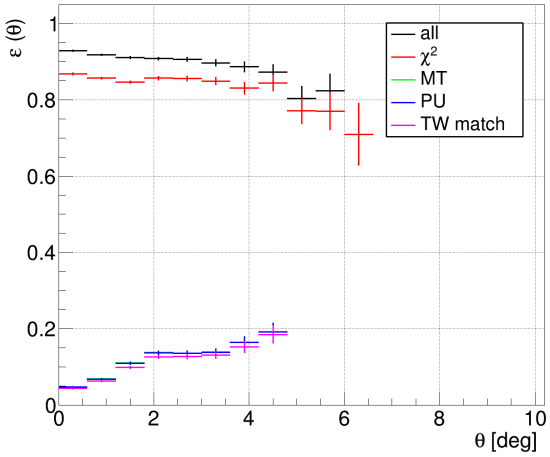

(f) $Z = 5$

Figure 4.11: Total and angular track reconstruction efficiency for the *Full* setup divided by Z. It is possible to see the effect of all the different event selection cuts applied.

with the event selection cuts showed above, could help lowering the time dedicated to these runs and, thus, increase the beam availability for physics runs.

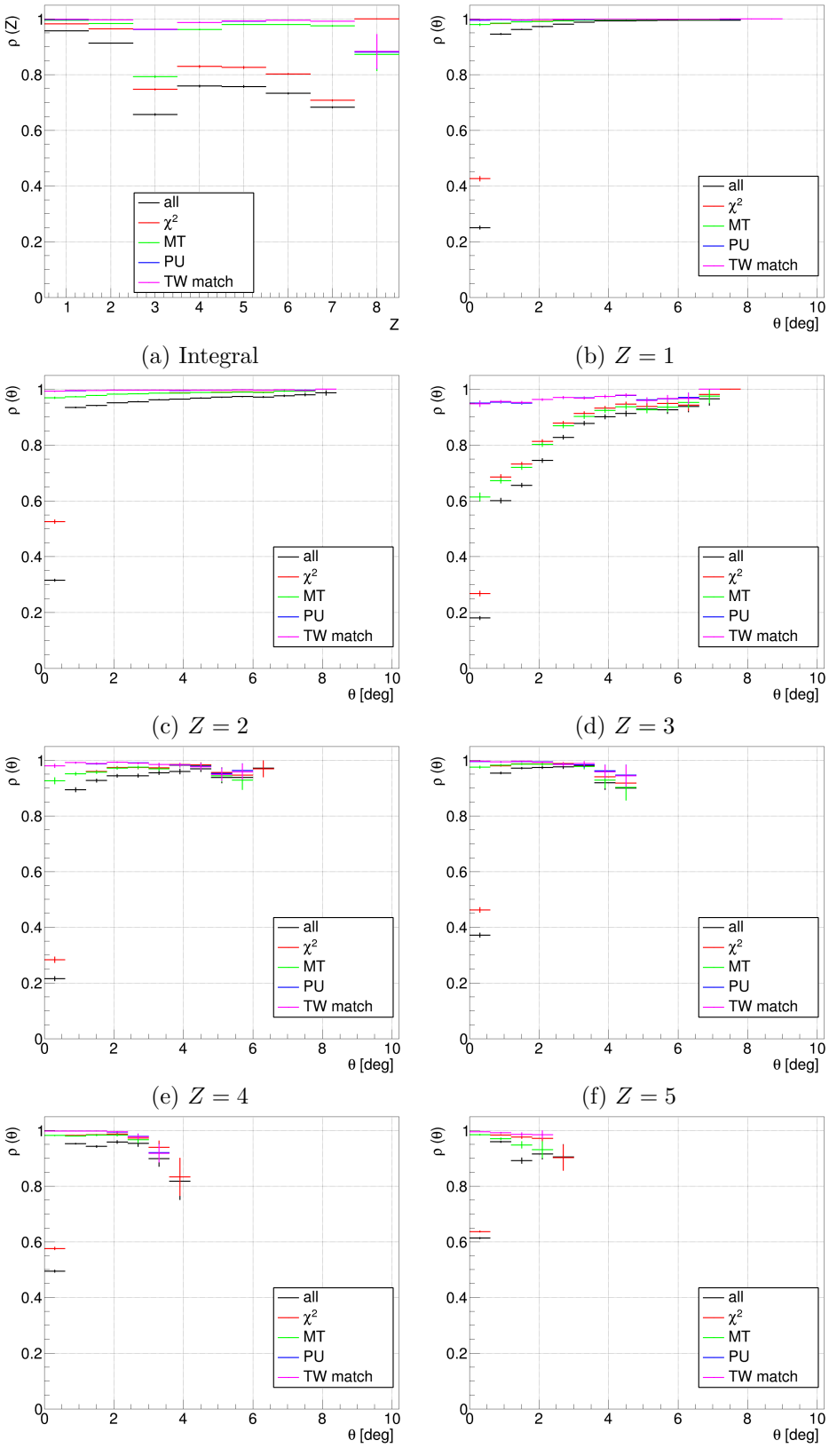

(a) Integral (b) $Z = 1$

(c) $Z = 2$ (d) $Z = 3$

(e) $Z = 4$ (f) $Z = 5$

(g) $Z = 6$ (h) $Z = 7$

Figure 4.12: Total and angular track purity for the *Partial* setup divided by Z, showing the effect of each consecutive selection cut.

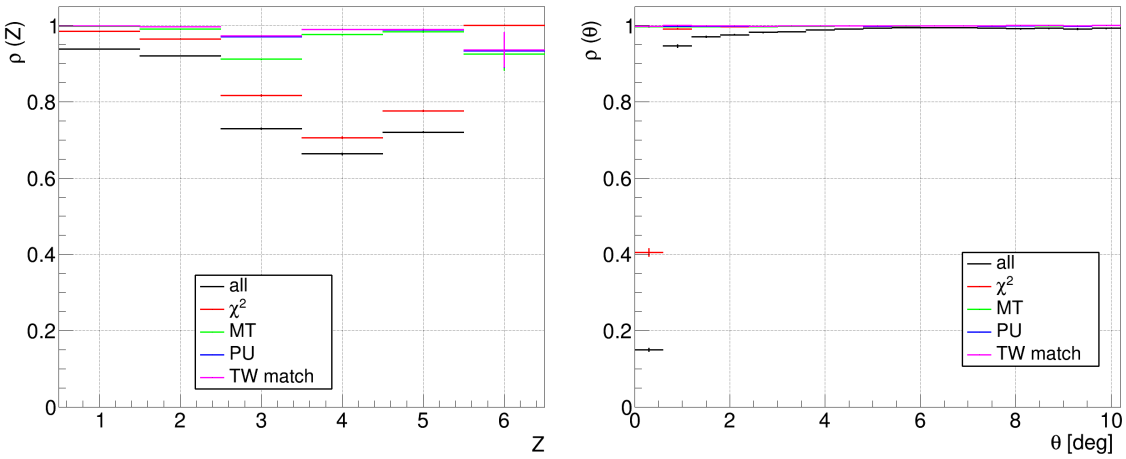

(a) Integral

(b) $Z = 1$

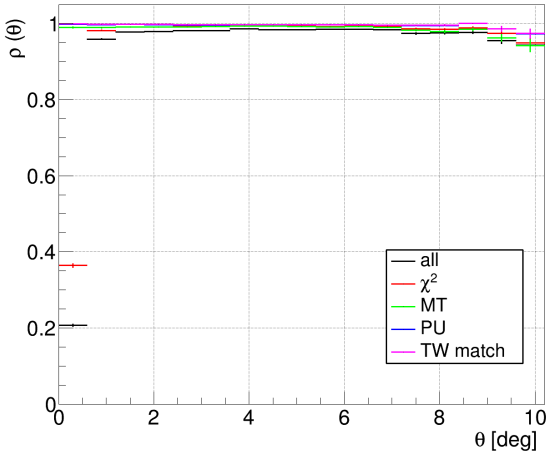

(c) $Z = 2$

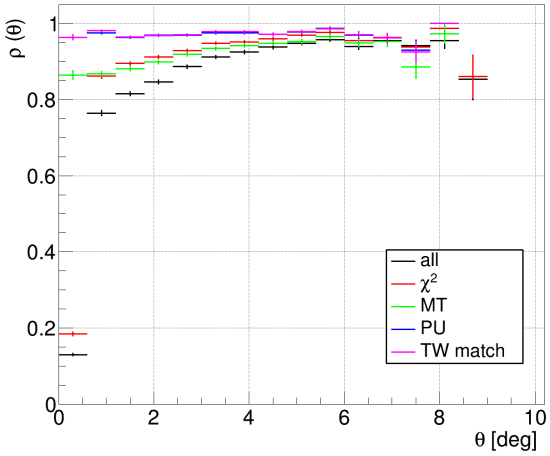

(d) $Z = 3$

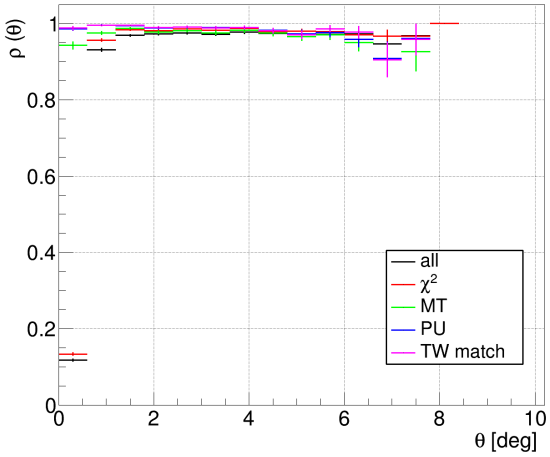

(e) $Z = 4$

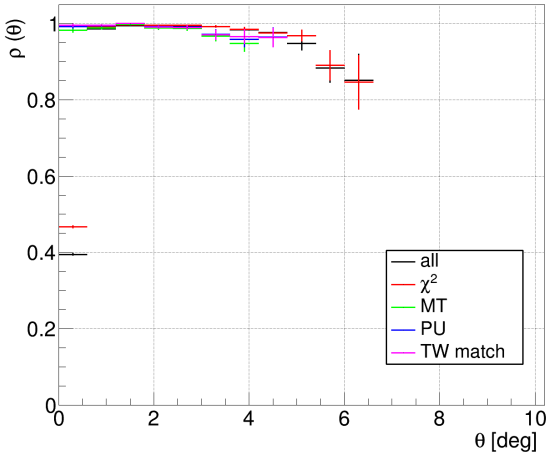

(f) $Z = 5$

Figure 4.13: Total and angular track purity for the *Full* setup divided by Z, showing the effect of each consecutive selection cut.

Angular resolution

Another study that was carried out is on the reconstruction performance of the fragment emission angle. The results obtained for track purity after the event selection cuts

show that the remaining tracks are well reconstructed. Using the cleanest sample available, i.e. after the "TW match" request, the direction of fitted tracks was compared to the *true* momentum of the corresponding MC particle at the interaction point inside the target. For each fragment, the angle between these two vectors $\theta_{reco-MC}$ was evaluated as a function of the MC track polar angle θ_{MC}, obtaining a distribution like those shown in Figure 4.14a and 4.14c. The first important result shown by these graphs is that the angle reconstruction performance is almost independent from the track angle for both simulations, i.e. with or without the magnetic field, with values of $\theta_{reco-MC}$ at the level of a few mrad. The main difference between the two cases is that, as it could be expected, $\theta_{reco-MC}$ has a broader distribution for the *Full* simulation where the tracking is more challenging. However, the difference between the MC and reconstructed direction is still at the level of mrad, which is compatible with the requested accuracy of the experiment. This is due to the very good position resolution of the VT detector, which has the highest impact in the track reconstruction at the target level.

The angular resolution of the tracking system can be obtained by taking the $\theta_{reco-MC}$ distribution of each θ_{MC} bin and calculating its mean. The corresponding results are shown in Figure 4.14b and 4.14d for each possible ion. The obtained resolution is almost constant up to 8° for both simulations and then gets slightly worse at higher emission angles. This could be due to the change in position resolution in the VT for tracks with high tilt. As a matter of fact, when particles cross a VT sensor in a direction different from the perpendicular, the relative pixel clusters are created in a non-circular shape and the resolution on one coordinate could be different from the other. In the *Full* simulation, this effect is enhanced by the intrinsic asymmetry introduced by the magnetic field on the bending axis (the x-axis in the FOOT case) and leads to a slightly worse angular resolution. This kind of effect, however, does not pose a problem for our purposes since the resolution is still very close to 1 mrad in the whole angular range of the FOOT setup and is, thus, compatible with the experimental requirements.

As it can be seen, in the *Partial* simulation (Figure 4.14b) the resolution is almost the same for all ions, with the exception of proton tracks that give a slightly worse result. This is again due to the different position resolution in the VT, which depends on the energy deposition in the different layers. The same behavior can be observed for the *Full* simulation (Figure 4.14d). Here, there is also the possibility to see the response of the tracking system at $\theta_{MC} > 9°$, since the TW was placed at a closer distance and the bending of the magnets makes it possible to see part of the light ions emitted at higher angles. For high θ_{MC} the angular resolution starts increasing more significantly, which is compatible with the worsening of the position resolution in the VT and the approaching of the geometrical acceptance limit of the tracking system.

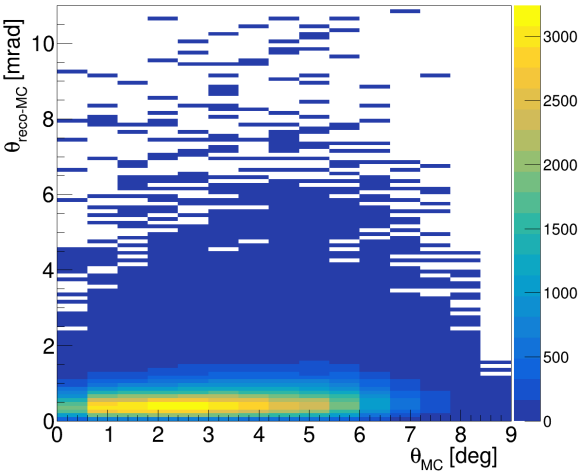

(a) *Partial* simulation, $\theta_{reco-MC}$ vs θ_{MC}

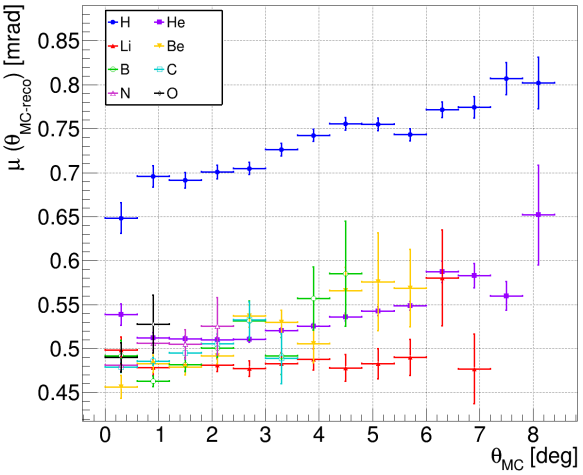

(b) *Partial* simulation, resolution

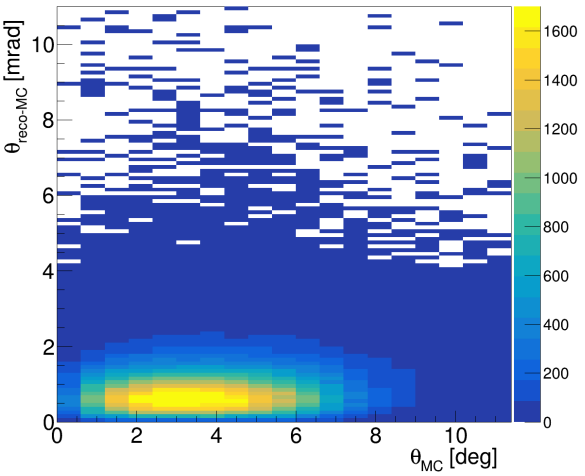

(c) *Full* simulation, $\theta_{reco-MC}$ vs θ_{MC}

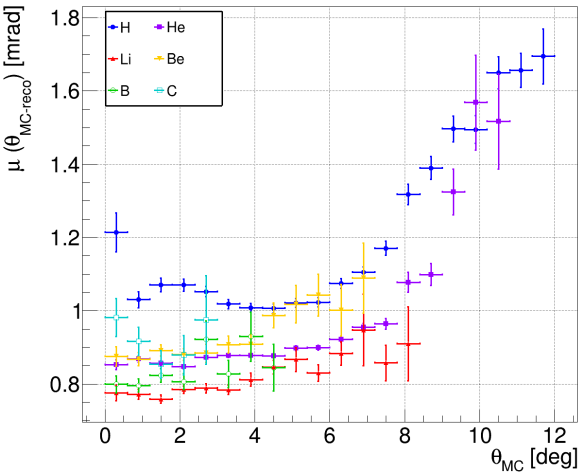

(d) *Full* simulation, resolution

Figure 4.14: (a) and (c): distribution of the angle between MC and reconstructed particle direction at the point of production as a function of the MC angle θ_{MC}. (b) and (d): Angular resolution of the tracking system calculated for the two MC simulations. The values and uncertainties reported are the mean of the $\theta_{reco-MC}$ distributions and their corresponding error.

Chapter 5

Results

One of the goals of this work is to determine a set of event selection cuts and requirements for global tracks with the aim of performing accurate cross section measurements. The results reported in the previous Chapter provide a global overview of the current status of the FOOT Global Reconstruction, showing that the chosen event selection chain is able to remove to background coming from out-of-target fragmentation reactions and, thus, produce a highly pure sample of particle tracks. This means that the corresponding tracking efficiency can be safely employed to re-compute the true fragment yields for cross section evaluation.

The final closure test to be performed is the evaluation of Monte Carlo cross sections using only information in a "*data-like*" manner, i.e. without the use of MC truth at any point of the analysis except for the evaluation of reconstruction efficiencies.

5.1 Cross section

Once the event reconstruction efficiency and purity are under control, the evaluation of the fragmentation cross section for a reaction in direct kinematics is quite straightforward. The elemental cross section for the production of fragments with charge Z can be written as

$$\sigma(Z) = \int_{E_{min}}^{E_{max}} \int_{0}^{\theta_{max}} \left(\frac{\partial^2 \sigma}{\partial \theta \partial E_{kin}} \right) \mathrm{d}\theta \mathrm{d}E_{kin} = \frac{C(Z)}{N_{beam} \cdot N_{TG} \cdot \varepsilon(Z)} \tag{5.1}$$

where the boundaries of the integral in kinetic energy E_{kin} and angle θ represent the TOF range where the charge identification algorithm is expected to work properly (100-800 MeV/u) and the angular acceptance of the TW for the corresponding setup, respectively, $C(Z)$ is the number of reconstructed fragments for each charge, N_{beam} is the number of primaries considered, $\varepsilon(Z)$ is the total reconstruction efficiency for a given charge (as calculated in Equation 4.1). N_{TG} represents the number of interaction centers per unit area in the target

$$N_{TG} = \frac{\rho \cdot \Delta x \cdot N_A}{A} \tag{5.2}$$

where N_A is the Avogadro Number and ρ, Δx and A are the density, thickness and mass number of the target. In both simulations under study, the chosen target was made of graphite ($A_{C-nat} = 12.0107$, $\rho = 1.83$ g/cm^2 as measured on the actual FOOT target) and had a thickness of $\Delta x = 0.5$ cm. N_{beam} corresponds to the number of primaries generated in each simulation, reported at the beginning of Chapter 4.

The angular differential cross section can be obtained by integration of only the kinetic energy part, i.e.

$$\frac{\mathrm{d}\sigma}{\mathrm{d}\theta}(Z,\theta) = \frac{C(Z,\theta)}{N_{beam} \cdot N_{TG} \cdot \Delta\theta \cdot \varepsilon(Z,\theta)} \tag{5.3}$$

where the counts $C(Z,\theta)$ and efficiency $\varepsilon(Z,\theta)$ are both evaluated at the corresponding angle and $\Delta\theta$ indicates the portion of phase space considered, i.e. the angular bin width. This can be also expressed in terms of the solid angle Ω as

$$\frac{\mathrm{d}\sigma}{\mathrm{d}\Omega}(Z,\theta) = \frac{C(Z,\theta)}{N_{beam} \cdot N_{TG} \cdot \Delta\Omega \cdot \varepsilon(Z,\theta)} \tag{5.4}$$

where the phase space portion is now given by the solid angle $\Delta\Omega = 2\pi \sin(\theta)\Delta\theta$. Here, the interaction has been considered symmetrical in the azimuthal angle φ since no physical consideration indicates a possible asymmetry in the fragment emission distribution in the transverse plane.

It has to be pointed out that Equations 5.1, 5.3 and 5.4 are reported in this form because the number of reconstructed tracks coming from background events has been considered negligible. This is a consequence of the results obtained in Section 4.3, which show how the purity of the reconstructed tracks after all the event selection cuts is close to 100% for all ions and over the whole angular range. If this was not the case, the contribution from background would have to be evaluated for each sample and then subtracted before cross section evaluation.

The reconstructed integral and differential cross sections in Ω for both setups are reported in Figure 5.1, 5.2 and 5.3. They have been obtained using the cleanest sample possible, i.e. applying all the event selection cuts described in Section 4.3. The differential cross sections are reported as a function of the particle angle of emission θ, calculated as the angle between the primary track reconstructed in the BM and the fragment direction after it exits from the target. Each of the shown graphs also contains its MC cross section, computed using the *true* information and indicated as σ_{MC}. In particular, σ_{MC} is calculated using Equations 5.1 and 5.4 and considering $C = N_{ref}$ (see Section 4.1) and $\varepsilon = 1$. Each of the plots also reports the difference between the reconstructed cross sections and the MC values, normalized to σ_{MC}. The reported uncertainties have been calculated considering the statistical uncertainty on C and N_{beam}, while the error on reconstruction efficiency is given by Equation 4.2.

For what concerns the *Partial* setup simulation, after all the event selection cuts, the reconstructed integral cross section is compatible with the true MC values at a level ranging from 2 to 5%. This is in general compatible also with the statistical uncertainty on the MC cross section values extracted from the N_{ref} yields. The calculated $\sigma(Z)$ is systematically slightly higher than the MC one, indicating that there still is some unknown effect causing a minor bias in the reconstruction, in particular for particles with $Z = 3$. For what concerns the differential cross sections, the $\mathrm{d}\sigma/\mathrm{d}\Omega$ is mostly compatible with the MC statistical uncertainty, showing only a $\sim 5\%$ overestimation for $Z = 3$ over the whole angular range and a minor drift in the values of heavier ions at large angles. However, it can be noticed that both of these effects are under control since the reconstructed and MC cross section values are compatible within one standard deviation.

The slight discrepancy found for $Z = 3$ is currently under study but one of the possible explanations could be linked to fragmentation events happening inside the TW detector. If, for example, a Be nucleus produced in the target reaches the TW detector and fragments in two He ions in the first layer of the detector, the charge reconstruction

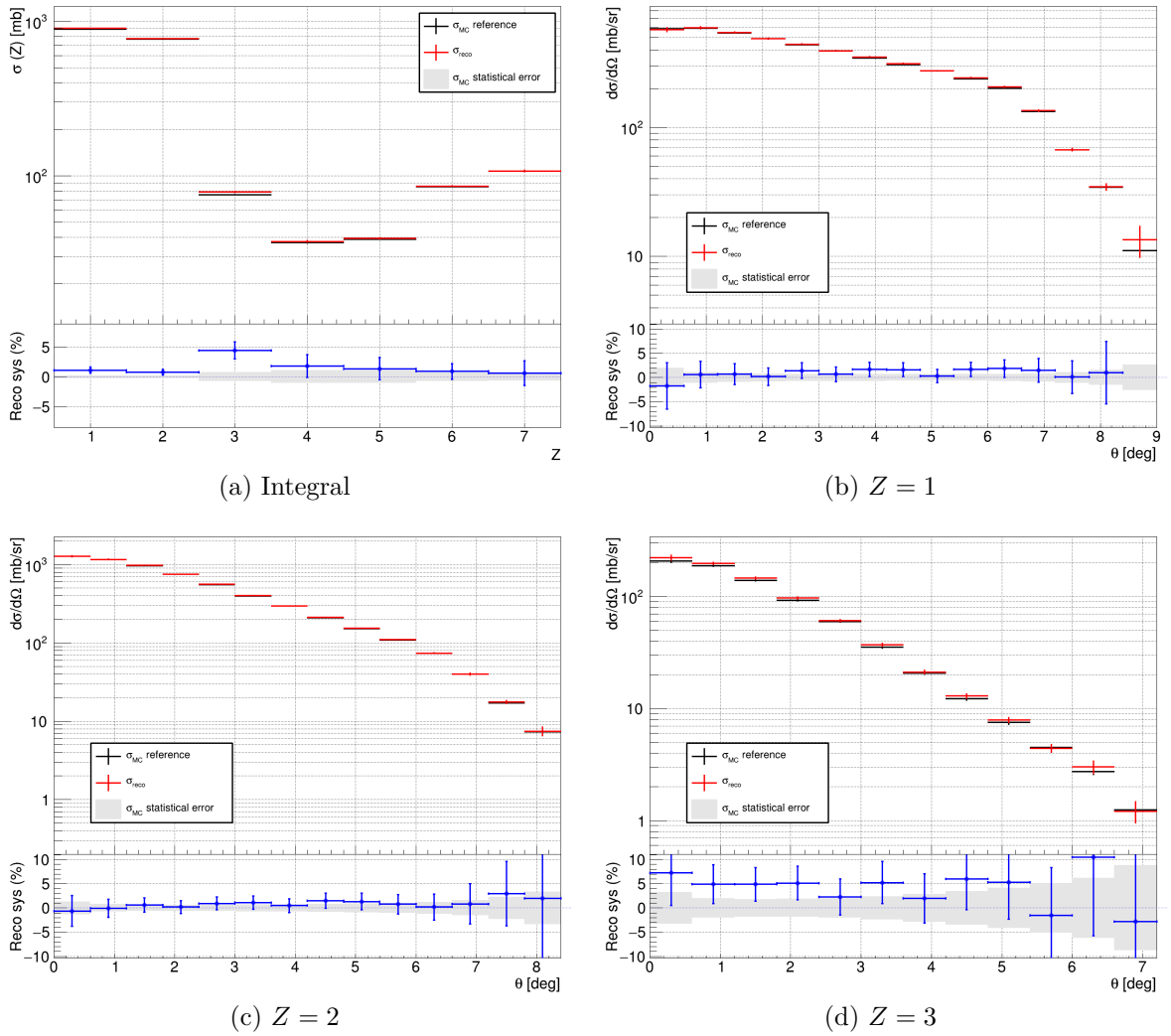

(a) Integral (b) $Z = 1$

(c) $Z = 2$ (d) $Z = 3$

Figure 5.1: (a) Total and (b)-(d) differential fragmentation cross section in the solid angle Ω for the ^{16}O + C reaction at 400 MeV/u of projectile energy (*Partial* setup). The differential cross sections reported here are for particles with $Z \leq 3$. The gray area in the pad of each graph represents the statistical uncertainty of the MC sample under study and is reported also in the following plots.

algorithm will associate the corresponding TW point with $Z = 3$ (see Figure 3.14b). In this case, the reconstructed track is actually produced by a real fragment of the primary and will thus satisfy all the event selection requirements but, at the same time, leading to an overestimation of the counts for Li cross section evaluation. The fact that this effect is particularly significant for Li could be explained by the high yield of He ions in fragmentation reactions. However, further investigation is currently ongoing to properly identify the root cause of this minor discrepancy.

Regarding the *Full* setup simulation, the reconstructed elemental cross sections are compatible with the MC values up to a maximum of 5%. The values obtained for $Z = 1$, $Z = 2$ and $Z = 4$ are compatible with MC both for the integral and for the differential cross section over the whole angular range well within 5% and mostly within one standard deviation of the MC statistical fluctuations. The minor overestimation for Li is still noticeable, also in the differential cross section values (Figure 5.3d), meaning that

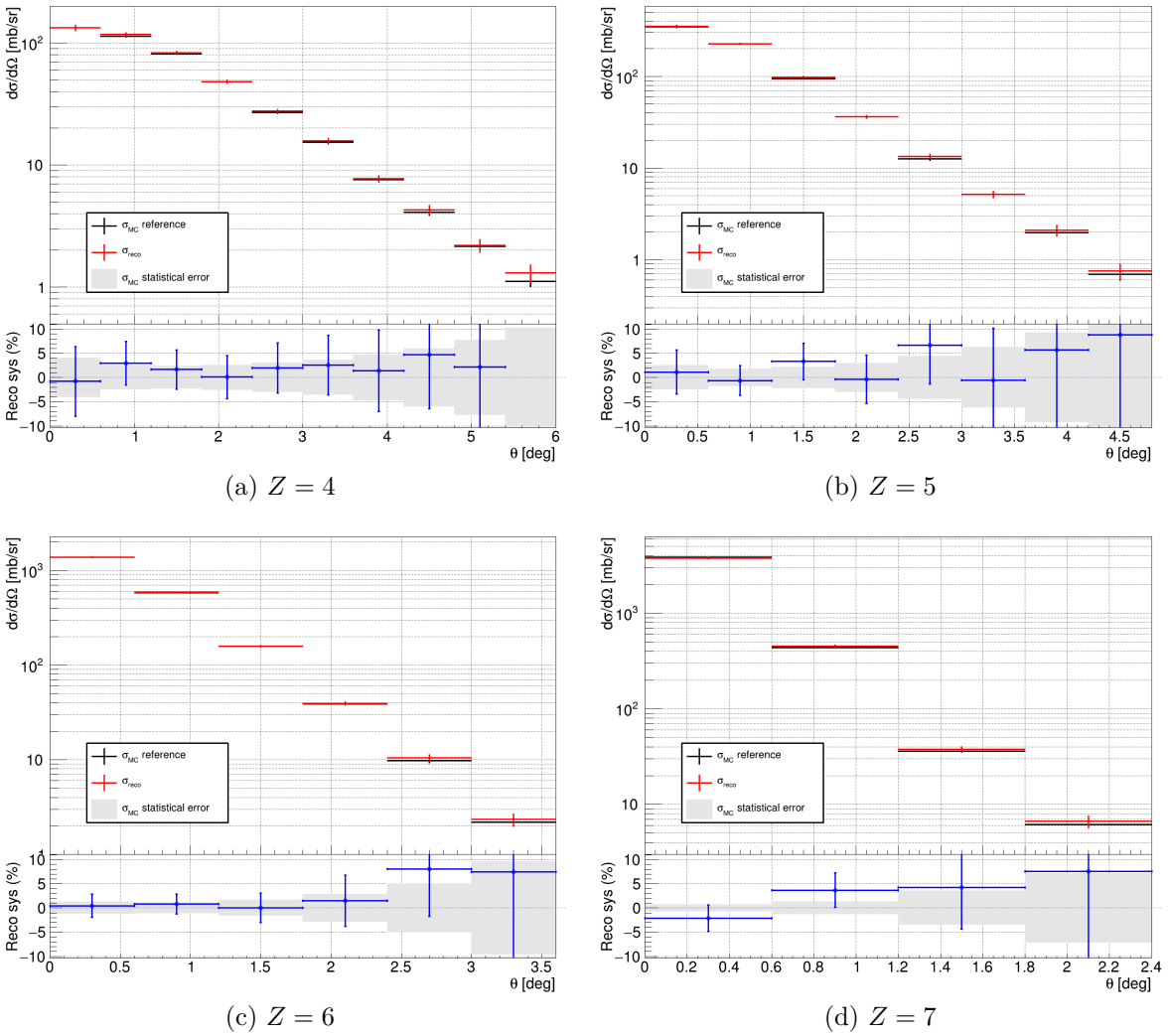

(a) $Z = 4$ (b) $Z = 5$

(c) $Z = 6$ (d) $Z = 7$

Figure 5.2: Differential fragmentation cross section in the solid angle Ω for the ^{16}O + C reaction at 400 MeV/u of projectile energy (*Partial* setup). The results reported here refer to all particles with $Z \geq 4$.

the effect causing this discrepancy is present also for the *Full* setup and needs further investigation. The reconstructed integral cross section for B ions is also affected by some systematic effect that causes an increase in the particle counts, which is easily noticeable in Figure 5.3a. The differential values reported in Figure 5.3f show that the effect is however less significant at low emission angle, where the cross section is at its maximum, while it increases at higher θ. This discrepancy is also now being studied and could be linked to the slight discrepancy present for Li.

To summarize, the full analysis chain of FOOT is currently capable of reconstructing the MC cross sections. Despite some minor systematic effects that are currently under study, the applied analysis has worked successfully on both simulations, with and without the magnetic field. In both cases, the reconstructed values are compatible with the true ones better than 5% for both the total and differential cross sections, showing that the closure test reported in this work constitutes a solid workflow for future analysis on experimental data.

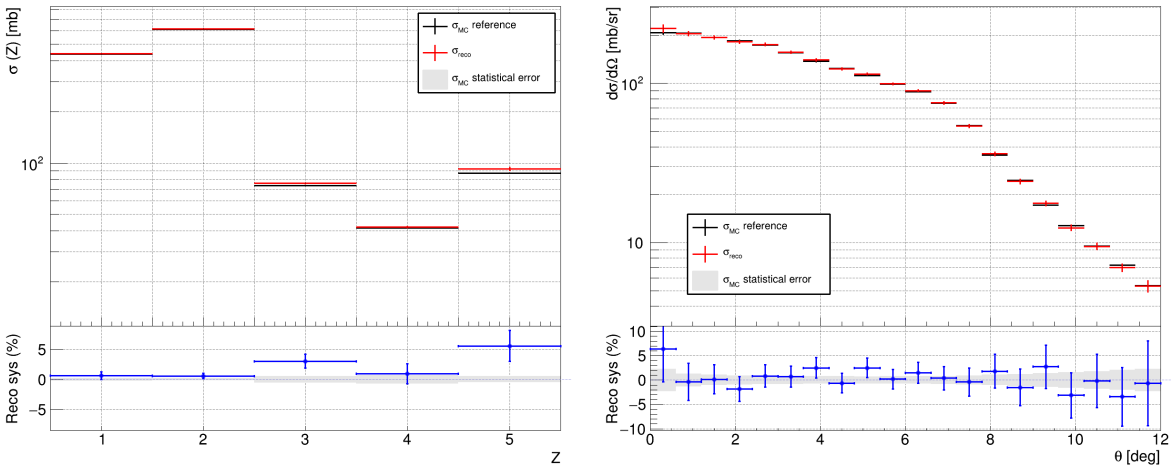

(a) Integral

(b) $Z = 1$

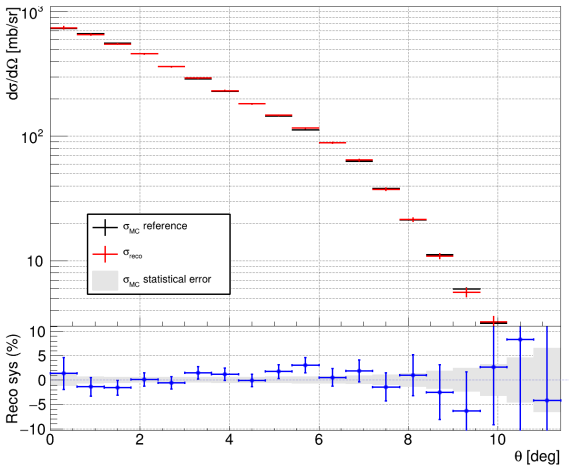

(c) $Z = 2$

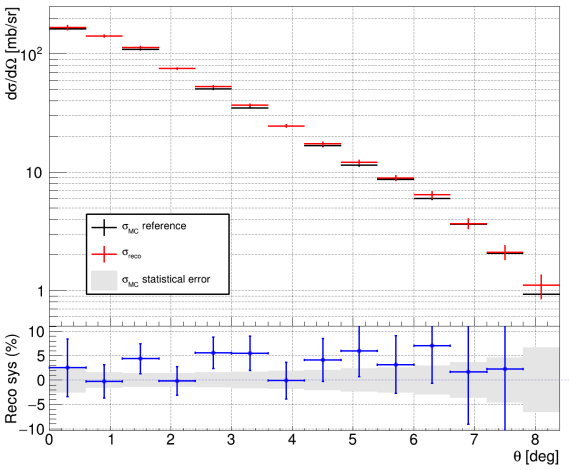

(d) $Z = 3$

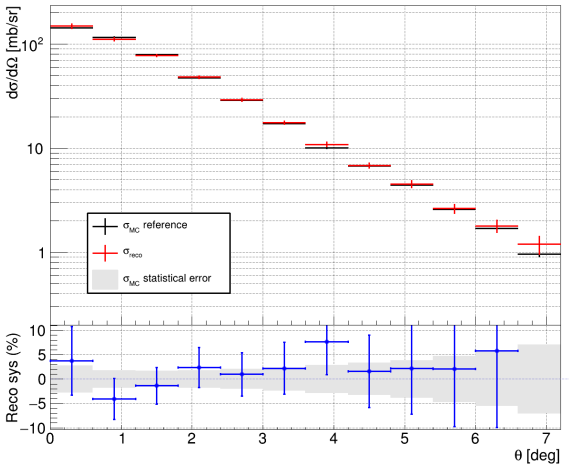

(e) $Z = 4$

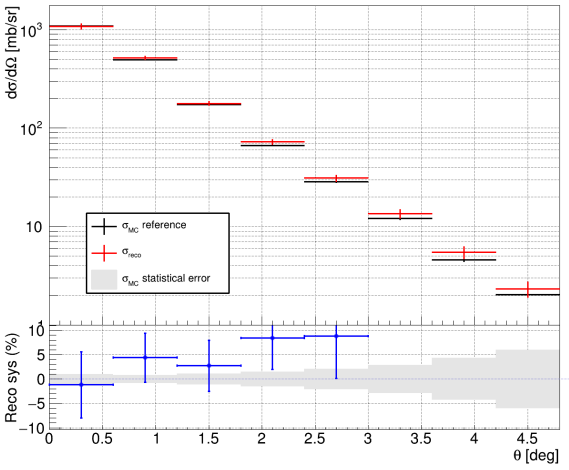

(f) $Z = 5$

Figure 5.3: Total and differential fragmentation cross section in the solid angle Ω for the ^{12}C + C reaction at 200 MeV/u of projectile energy (*Full* setup).

5.2 Future perspectives and developments

One of the key concepts to remember is that FOOT is an experiment that, at the time of writing, is still partially under development. The performance shown in the last two chapters have been obtained by limiting the amount of information used during event reconstruction to that available at the moment for the analysis of real data. This means that there is still significant room for improvement in terms of track reconstruction. The development of the tracking algorithms has been conceived with the idea to closely follow the addition of new information from the whole FOOT setup, keeping in mind that it should be applicable to both MC simulations and real data at all times.

Global tracking improvements

The FOOT Global Reconstruction has shown good performance at this stage but many aspects can still be developed to further improve both the track selection and background rejection.

In terms of track selection, two main aspects are currently under development other than the already cited optimization of extrapolation tolerances. On the one hand, new particle tracking algorithms will be developed with the aim of adding new approaches to the problem and provide useful tools for the study of systematical uncertainties. One of the possible choices would be the use of a VT-TW long range association for seed tracklets construction, with the subsequent extrapolations moving to the inner parts of the spectrometer. On the other hand, global tracks can be used to also retrieve the point of interaction inside the target. This possibility of vertex reconstruction through particle trajectories would also help in the rejection of cloning and mixing effects, e.g. by removing the tracks not reaching the interaction point.

For what concerns the background coming from out-of-target fragmentation, one of the possible improvements could be the implementation of an event classification algorithm based on cluster multiplicity along the FOOT tracker. As a matter of fact, an in-target fragmentation is characterized by a non-increasing number of clusters from VT to TW, since particles can only be "lost" along the tracker due to geometrical acceptance. Instead, if the fragmentation happens inside the magnetic spectrometer, the number of clusters found in consecutive planes is expected to increase. The application of an event classification has to be done very carefully since it has to take into account both physical (e.g. fragment emission angles) and experimental effects (e.g. detector efficiencies and acceptance, primary beam pile-up, etc.).

In addition to the direct improvements on particle tracking, the output of global reconstruction can also be further processed to perform isotopic identification. The atomic mass calculated from Equation 2.10 and shown in Figure 4.6 for the *Full* setup sample is a continuous value. The actual mass identification strategy needs an additional step to obtain a discrete value. Other than the χ^2 minimization and the Augmented Lagrangian Method already cited in Section 2.2, a possible approach when no information on kinetic energy is available could be a mass identification algorithm analogous to that employed for charge reconstruction. In this case the two physical quantities to correlate would be the measured TOF and reconstructed p, leading to a set of graphs like those shown in Figure 5.4.

In these plots, the different isotope populations are easily distinguishable and are indicated by the corresponding symbol. The mass identification could be applied by tuning the equation linking p and TOF on MC truth information for each different isotope. In

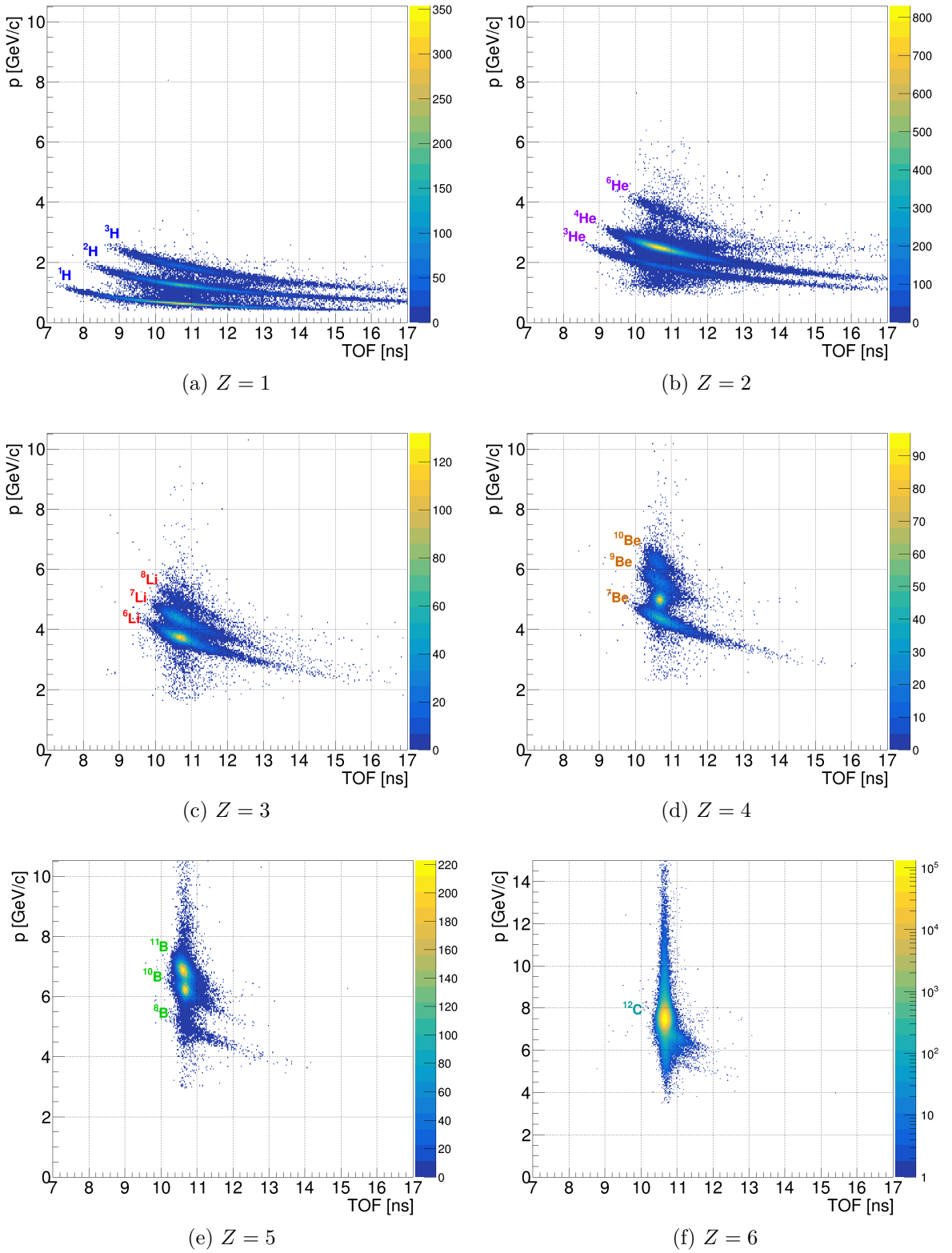

(a) $Z = 1$ (b) $Z = 2$

(c) $Z = 3$ (d) $Z = 4$

(e) $Z = 5$ (f) $Z = 6$

Figure 5.4: Reconstructed track momentum as a function of Time Of Flight for all the different ion species. The graphs were obtained using the *Standard* selection. The plot for $Z = 6$ is reported in logarithmic scale because of the much higher statistics given by non-fragmented primary ions.

this case, the equation to use would be

$$p = \frac{k_1/\mathrm{TOF}}{\sqrt{1 - k_2/\mathrm{TOF}^2}} \tag{5.5}$$

where the expected values for the two constants are $\overline{k_1} = m \cdot L$ and $\overline{k_2} = (L/c)^2$, with L indicating the flight path of the fragment, m its mass and c the speed of light. Once all the functions are tuned, the mass of each fragment can be assigned finding the curve at minimum distance from the p-TOF point in the 2D plane of the corresponding Z.

It is interesting to notice that the background generated by out-of-target fragmentations is very easily noticeable in Figure 5.4d, where a fake population of particles appears in between ^{7}Be and ^{9}Be. The much narrower TOF distribution of this fake tracks is compatible with events of the kind shown in Figure 4.7. In fact, most of the flight path along the track is covered by the primary, meaning that the β distribution of the secondary Be has a lower impact on the TOF with respect to that of an in-target fragment. In particular, the case of ^{8}Be is very important because, with the FOOT setup, it is virtually impossible to detect such isotope and any track identified as ^{8}Be necessarily comes from a mis-reconstruction (as also explained in Section 4.2). As a matter of fact, the TOF of nuclei in the FOOT apparatus is in the range of 5-20 ns, while the ^{8}Be nucleus has an half-life for the break-up in two α particles of $82 \cdot 10^{-18}$ s.

Detector improvements

One of the most useful information that is currently not used in Global Reconstruction is the kinetic energy measurement of the calorimeter. The association between TW points and CALO clusters could provide a solid starting point for the definition of track seed state before the Kalman Filter fit. As a matter of fact, with the addition of the CALO, it would be possible to also provide a reasonable guess for the particle mass (together with the information from the TW), removing the need to initially use the main isotope as hypothesis (see Section 3.3).

For what concerns the rejection of out-of-target fragmentation events, one of the most important and powerful tools could be the implementation of charge identification in other detectors of FOOT other than the TW. First of all, the MSD is, in principle, capable of measuring the energy loss in the different silicon layers, meaning that it can be used to perform Z identification. At the moment, this information is not available since the detector needs further studies to take into account the non-uniformity of charge collection between the *readout* and *floating* strips. The FOOT Collaboration is already working to provide this feature as soon as possible since a reliable Z measurement in the MSD can strongly help to identify mis-associations between MSD and TW points in particle tracking.

For what concerns the other trackers, the VT and IT are not able to perform accurate charge identification but they could help in separating between low and high Z fragments. As a matter of fact, the different energy deposition reflects in a change in the reconstructed cluster size, i.e. the number of pixels in a single cluster. Studies performed on M28 chips in other works [65] show this correlation, meaning that the VT and IT planes of FOOT could also be used in such way. This kind of information could provide an additional tool for track mixing minimization.

Conclusions

The aim of the FOOT experiment is the measurement of double differential cross sections with respect to kinetic energy and emission angle for nuclear fragmentation reactions of interest in Particle Therapy and Radiation protection in Space. The results obtained by FOOT will be used to further improve the accuracy of Treatment Planning Systems in Particle Therapy and in the development of novel shielding materials for future long-term space missions. The apparatus consists of two complementary experimental setups: an Emulsion Cloud Chamber with large angular acceptance and mainly focused on the detection of light fragments ($Z \leq 3$) and an Electronic Setup with narrower acceptance made of sub-detectors optimized for the detection of heavier nuclei ($3 \leq Z \leq 8$).

The Ph.D. project presented here shows the development and current performance of the Global track Reconstruction of the FOOT electronic setup. Several track finding algorithms have been implemented and tested on two Monte Carlo simulations replicating two different experimental setups and conditions. As of now, the *Standard* forward tracking algorithm proved to be the most reliable approach available, showing good track reconstruction efficiency ($> 60\%$ for the *Partial* setup and $> 50\%$ for the *Full* setup) with a negligible rate of track cloning ($< 10^{-4}$ for both samples). The event selection cuts applied to all particle tracks have also shown to be very efficient in improving the purity of the reconstructed sample, leading to values close to 100% for all ions in the corresponding angular range.

Furthermore, the study of the angular and momentum resolution shows that the current performance of the tracking system matches the experimental requirements of FOOT. In particular, the angular resolution obtained for the *Partial* setup simulation is of $0.5-0.6$ mrad for ions with $1 < Z \leq 8$ and of $0.7 - 0.8$ mrad for protons over the whole angular acceptance of the setup, i.e. up to 8°. For the *Full* setup simulation, the angular resolution for all reconstructed ions ($1 \leq Z \leq 6$) ranges from 0.8 to 1 mrad up to 8°, with a slight worsening up to 1.5 mrad at larger emission angles, i.e. at the boundaries of the geometrical acceptance. The momentum resolution extracted from this latter Monte Carlo sample is of 2.5% over the whole range covered by the reconstructed ions, i.e. from 0.5 to 8 GeV/c, which is also significantly better than the $4-5\%$ required by the design of the experiment. The obtained momentum resolution also allows for isotopic identification of the detected nuclear fragments with good accuracy, which will be further improved when the measurement of kinetic energy from the FOOT Calorimeter will be available.

The final closure test of cross section evaluation shows that the developed reconstruction and analysis chain is capable of obtaining results compatible with the simulations at the level of 5%. For what concerns Monte Carlo simulations without the magnetic field, the reconstructed cross sections are compatible with the true values within the statistical uncertainties for both the integral and differential cross sections. The results obtained from the simulation with the *Full* setup show that the same reconstruction chain can be applied when the magnetic field is present and obtain the same level of compatibility with

Monte Carlo, with a minor systematic effect on B fragments.

The compatibility between reconstructed and Monte Carlo cross sections also implies that the implemented event selection cuts are able to correctly remove the background generated by out-of-target fragmentation events, lowering its impact with respect to in-target reactions from about 25% to less than 0.1%. The most important implication of such result is that FOOT could potentially avoid performing runs specifically dedicated to background subtraction during experimental campaigns. This will allow for a larger time allocation to physics runs, making it possible to further reduce the statistical and systematical uncertainties on cross section measurements.

In conclusion, this work has shown that the FOOT Global Reconstruction is capable of reproducing the fragmentation cross sections expected from Monte Carlo simulations with very good accuracy. The performance obtained are compatible with the requirements of the experiment, granting cross section measurements with enough precision to bring an improvement in both Particle Therapy treatment planning and Space Radiation Protection risk assessment studies. Despite the many improvements that can still be implemented in the analysis chain, the developed tools constitute a solid workflow to perform the experimental cross section measurements foreseen by the FOOT physics program.

Appendix A

Neutron detectors characterization at n_TOF

As already described in detail, FOOT (FragmentatiOn Of Target) aims at performing high precision cross section measurements for fragmentation reactions of interest in hadrontherapy and radiation protection in space. Thus far, the main focus of the experiment has been dedicated to the detection and characterization of charged fragments. However, one of the most complex contribution to evaluate in radiation risk assessment studies is that given by neutrons. The lack of experimental cross section data for nuclear fragmentation in the energy range between 100 and 800 MeV/u is even more critical when it comes to neutron production, meaning that their impact is extremely hard to evaluate [92, 23].

To address this additional problem, in 2021, the FOOT collaboration started the development of dedicated neutron detectors that will be added to the current setup in order to retrieve the information on neutron production in the interactions between beam and target. Two detection systems have been proposed as potential upgrades of the FOOT setup: on the one hand, a system based on BC-501A liquid scintillators with neutron/γ discrimination capabilities, to add to the current FOOT setup; on the other hand, a system based on BGO crystals operated in phoswich mode, which could potentially represent a future upgrade of the existing FOOT calorimeter.

In 2022, a dedicated data acquisition campaign was carried out at the n_TOF facility at CERN to evaluate the capabilities of the two systems. First, the neutron/γ discrimination efficiency of the BC-501A system was studied using radioactive sources. Then, the two systems were placed in the n_TOF experimental area to study their neutron detection efficiency under a well characterized neutron beam. The n_TOF facility is particularly suitable for this measurement since it can provide a neutron beam with an energy spectrum that spans up to 1 GeV. In the following sections, the first results concerning the characterization of the two possible neutron detectors are reported.

A.1 The FOOT neutron detectors

Among the devices currently under study as possible upgrades of the FOOT setup dedicated to neutron detection, two systems are already available for their use in measurement campaigns.

The first system is made of a liquid scintillator (BC501-A), sensitive to neutral particles, combined with an EJ200 plastic scintillator in front, which acts as a veto for charged

particles. The active volume of the detector is a cylinder with 3 inches diameter and 3 inches height. The BC501-A has been chosen for its good time resolution and its capability of discriminating neutrons and γ-rays. The n-γ discrimination is a fundamental prerequisite since the main source of background after the removal of charged particles, through anti-coincidence with the veto in front, is the one induced by γ-rays. In the system studied for FOOT the BC501-A is readout through a PMT, while the plastic scintillator veto is coupled with a SiPM. A picture of the detectors is shown in Figure A.1a.

The second device consists of a Phoswich detector [93] based on BGO crystals coupled with fast EJ232 plastic scintillators in front. A prototype of the system is shown in Figure A.1b. The crystals have a truncated pyramid shape, with 2.4x2.4 cm^2 front area, 3.3x3.3 cm^2 rear area and 24 cm length, while the plastic scintillator is 3 mm thick. The BGO Phoswich is being developed as a possible upgrade of the current FOOT calorimeter, which is made of 333 BGO crystals [94]. The coupling with a fast plastic scintillator significantly improves the time response of the detection of charged particles, maintaining a slower rise time on neutron signals. This allows for particle discrimination without the need of an independently read-out veto detector.

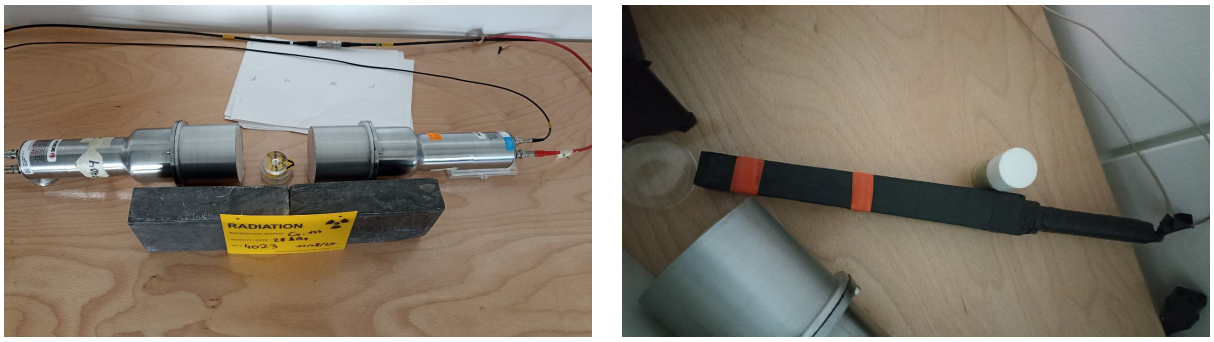

(a) (b)

Figure A.1: FOOT neutron detector prototypes during tests with radioactive sources. (a) BC501-A liquid scintillators and (b) BGO crystal in phoswich mode.

Both of these detectors, however, still require a careful evaluation of their neutron detection efficiency, which – in turn - is only possible through irradiation under well-characterized neutron beams. For what concerns the BC-501A systems, another important feature that has to be carefully verified and quantified is their n-γ discrimination capability in the energy region of interest. Very few facilities in the world are capable of providing a neutron beam in the energy range explored by the FOOT physics program, i.e. $1 - 1000$ MeV. To carry out the characterization campaign, the best option available was the n_TOF facility [95].

A.2 Detector characterization at the n_TOF facility

The neutron Time Of Flight (n_TOF) facility is a pulsed neutron source based at CERN. A sketch of the experimental complex is shown in Figure A.2. At n_TOF, the neutron beam is produced by spallation of the 20 GeV/c proton beam provided by the Proton Synchrotron (PS) impinging on a lead target. The neutrons generated in the target fly through the different beam lines of the facility, which lead to the three experimental areas:

- EAR1, placed at a distance of 185 m from the target. The neutron beam line is horizontal and tilted of 10° with respect to the direction of impinging protons.
- EAR2, placed at 20 m from the target, vertically at 90° with respect to the proton beam direction.
- NEAR, placed at only 3 m from the target, behind a shielding wall and a collimator.

The PS proton bunches have an intensity of $3 - 8 \times 10^{12}$ particles/bunch and the spallation reaction can yield up to 350 neutrons per incident proton, resulting in a very high instantaneous neutron flux in all the experimental areas [95].

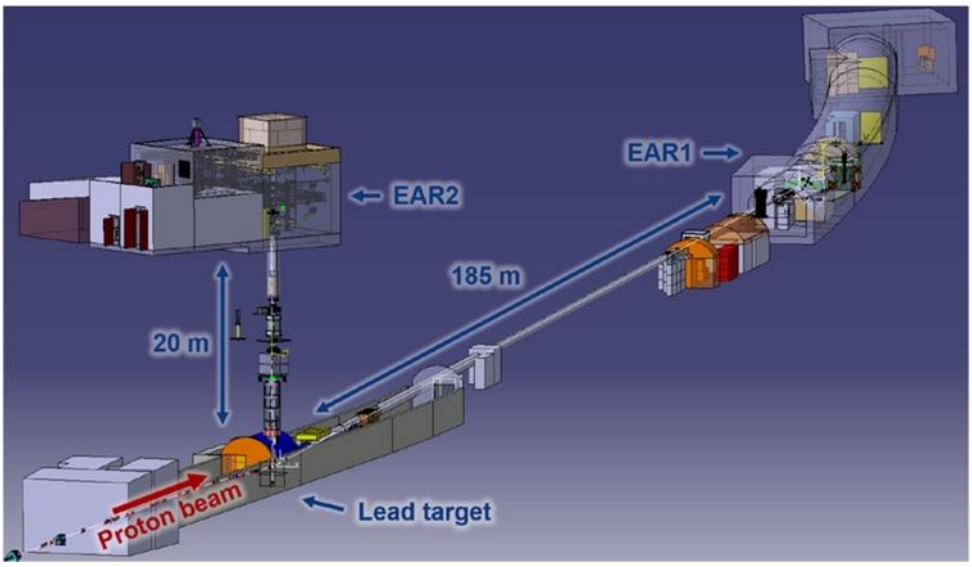

Figure A.2: Schematic view of the Experimental AReas (EAR) of n_TOF. The horizontal (EAR1) and vertical (EAR2) neutron beam lines are visible. An additional experimental area (NEAR) is located close to the target, at an approximate distance of 3 m.

The main characteristic of n_TOF is its capability of measuring the energy of the generated neutrons with an extremely good resolution, of the order of 10^{-3}-10^{-5}. This level of precision is achieved through the Time-Of-Flight technique, which links the information on the detection time in the experimental areas to the energy of the neutron that generated the signal. As a matter of fact, the spallation reaction, combined with borated-water moderation system, produces neutrons of energy ranging from thermal to GeV. These particles cover the flight paths to the experimental areas with very different TOF, which is directly related to the energy of the neutron at the time of production. Knowing the length of the flight path L, the kinetic energy E of the neutron can be calculated for TOF as

$$\begin{cases} E = mc^2(\gamma - 1) \\ \gamma = \sqrt{\left(1 - \frac{L^2}{c^2 TOF^2}\right)^{-1}} \end{cases} \qquad \frac{\Delta E}{E} \underset{\sim}{\propto} \frac{\Delta v}{v} = \sqrt{\left(\frac{\Delta TOF}{TOF}\right)^2 + \left(\frac{\Delta L}{L}\right)^2} \tag{A.1}$$

In particular, the very long flight path of n_TOF EAR1 makes it very suitable for the characterization of the FOOT neutron detectors [96]. In order to comply with the dense physics program of the facility, the FOOT setup was actually mounted in the Neutron Escape Line (NEL) of EAR1,with the aim of acquiring data downstream of the

experimental area in a parasitic way. The final setup is sketched in Figure A.3. The sample was placed at a distance of about 200 m from the lead spallation target, perpendicular to the direction of incoming neutrons. The mechanical structure of the setup was made of aluminum frames with the possibility to slide and adjust the distance and angle of the detectors with respect to the target.

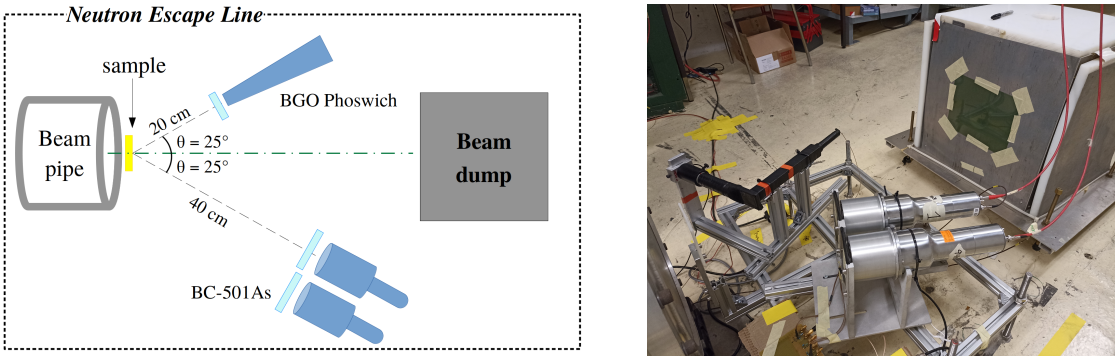

(a) (b)

Figure A.3: Setup used for the data acquisition campaign in the NEL of n_TOF EAR1. (a) Schematic view of the apparatus, showing the distances and angles of the detectors with respect to the sample and (b) picture of the mounted experimental setup.

In principle, knowing the neutron flux in the experimental area, one could compare it to the flux measured by the different devices on the beam line and thus extract their detection efficiency. However, this approach is really complicated to follow because of the so-called "γ-flash". This term indicates the first signal reaching the experimental area after a collision of the proton beam on the spallation target and it is generated by γ-rays and ultra-relativistic particles. The γ-flash is a very intense pulse which blinds the readout electronics of the detectors for a certain amount of time. This poses a limit on the minimum TOF, and thus maximum neutron energy, detectable in the experimental area.

In the case of the FOOT detectors, the basic idea to mitigate the effect of the γ-flash is to exploit the neutron-proton elastic scattering placing a H-rich sample directly in beam and the detectors at a fixed angle. Since the amount of protons and neutrons produced via n-p elastic scattering and hitting the detectors is the same and the detection efficiency can be considered 100% for charged particles, the ratio between the number of detected neutrons and protons gives a measurement of the neutron detection efficiency. An additional measurement of this efficiency can be obtained by comparing the number of detected neutrons with the expected one, calculated from the evaluated neutron flux in the experimental area and the n-p elastic scattering cross section. This is possible because the n-p elastic scattering cross-section is very well known and it is considered the main reference for the high-energy-neutrons-induced reactions [97].

The discrimination of signals generated in the detectors by charged and neutral particles can be obtained requesting the coincidence and anti-coincidence with the plastic scintillators in front of each device. The additional veto placed in front of the BGO crystal was used to verify the difference in the phoswich response between charged particles and neutrons. This information is crucial to assess the particle identification capabilities of the detector by itself, without the need for the veto.

The energy E_n of a neutron impinging on the detectors, after the elastic scattering in

the sample, has to be calculated as

$$E_n = E'_n cos^2(\theta) \tag{A.2}$$

where E'_n is the energy of the primary neutron undergoing the scattering, obtained from Equation A.1, and θ is the scattering angle, i.e. the one fixed by the placement of the detectors. From Equation A.2, it is clear that the energy resolution is mainly dictated by the uncertainty on the scattering angle θ, which in turn depends on the geometry of the setup. The final distance of the detectors from the sample was chosen in order to obtain a maximum uncertainty on the energy of detected neutrons of about 10-15%, limiting the impact of the γ-flash and acquiring the highest statistics achievable.

During this measurement, it was impossible to utilize a pure H target due to the need of keeping it at cryogenic temperatures. The solution was to perform the measurement with both polyethylene (PE, C_2H_4) and graphite samples of the same mass thickness, using the latter to evaluate and subtract the background generated by n + C reactions.

A.3 Preliminary results

For what concerns the BC-501A system, the first test carried out was an assessment of the n-γ discrimination capabilities. This was performed exposing the detector to different sources of either neutrons (^{252}Cf), γ rays (^{88}Y) or both (AmBe). Particle discrimination was achieved through Pulse Shape Analysis with the aim of decomposing the signal in a fast and a slow component. In this case, the fast component was defined as the portion of the signal acquired within 10 ns of its onset, while the slow component was the rest of the signal tail. An example of the separation between the two components is reported in Figure A.4.

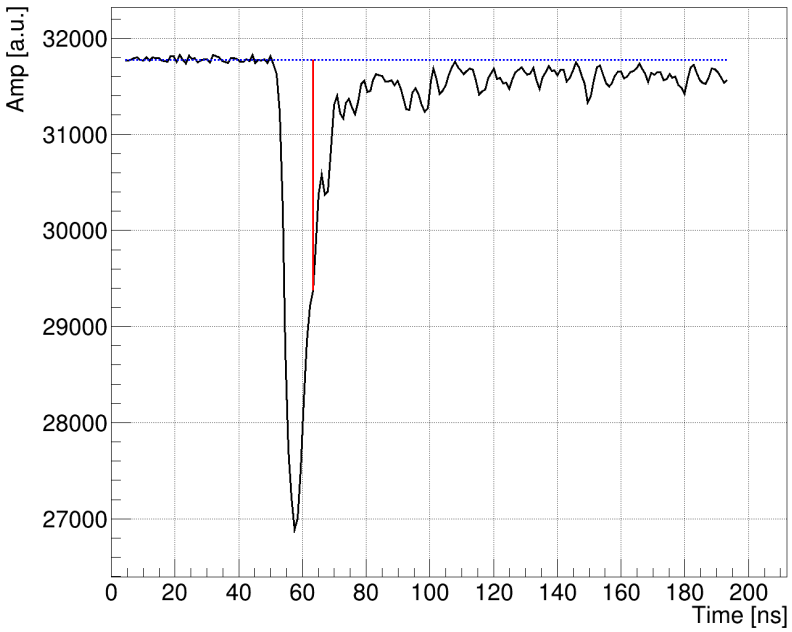

Figure A.4: Example of fast and slow component separation in a BC-501A signal obtained with an AmBe source. The blue dashed line represents the baseline of the waveform while the red solid line indicates where the fast component of the signal ends and the slow one starts.

The fast and slow portions of the pulse were integrated separately, yielding results as those shown in Figure A.5a, where data from an AmBe source are shown. The two visible populations are given by γ-rays and neutrons, with the latter recognizable in the lower portion of the graph where the slow component is dominant. Figure A.5b shows the amplitude spectra of the signal obtained with the AmBe source and its neutron and γ components obtained through a selection performed using a parabolic cut in Figure A.5a. As it can be seen, the Compton edge visible in the total spectrum is completely associated with the component given by γ-rays, indicating a good particle discrimination efficiency. A first study performed using the data acquired with the AmBe source has shown that it is possible to achieve an n-γ discrimination efficiency of around 90% with the current system. This result is quite promising but it is important to point out that it has been achieved using neutrons with energy up to 10 MeV. Further studies will be performed in the future to properly characterize the n-γ discrimination also at higher energies.

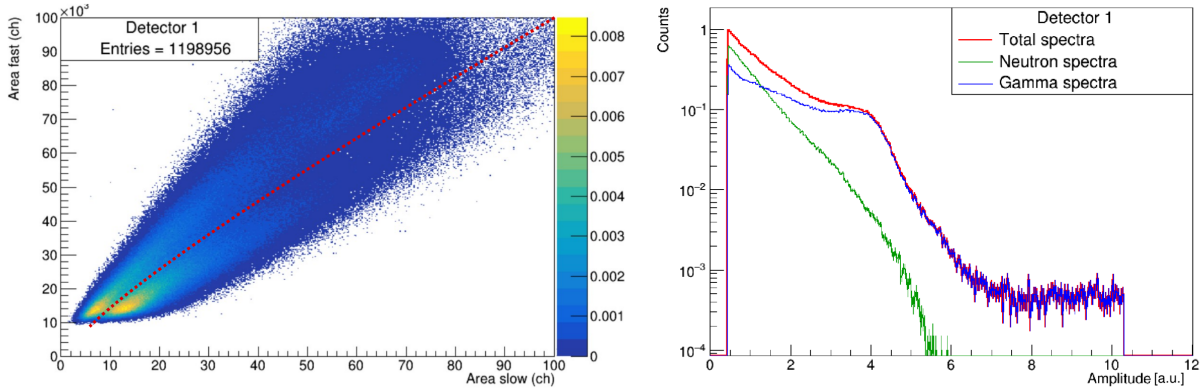

(a) (b)

Figure A.5: Neutron-γ discrimination capabilities of the BC-501A detector with an AmBe source. (a) shows the relation between the area (integral) of the fast and slow components of signals, highlighting two populations. The dashed red line indicates the parabolic cut applied to separate neutrons and γ-rays. (b) Contribution of each population to the spectrum of the source.

Figure A.6 shows the amplitude of registered signals as a function of TOF obtained for one of the BC-501A systems with the neutron beam impinging on a 5 mm PE sample. Here and in all the following plots, the TOF is reported taking the time of the γ-flash as reference, i.e. $TOF = t_{signal} - t_{\gamma-flash}$. The actual TOF-energy conversion needs to take into account this component, which for a 200 m long flight path is $t_{\gamma-flash} \simeq 667$ ns.

The time window chosen to define a coincidence event between a signal in the VETO and in the BC-501A was of $\pm$10 ns. It can be noticed that, except for a minor background given by random events, coincidence signals start only when the energy of the scattered particle is enough to punch through the plastic scintillator. The branch mainly visible in the events recorded in the VETO and defined in coincidence (Figure A.6a) is generated by charged particles coming from elastic n-p reactions, showing the typical decrease in signal amplitude at higher energies (lower TOF). The same structure can be observed also in Figure A.6c for anti-coincidences, with the addition of signals coming from lower energy particles which can not go through the VETO. The presence of signals above the punch-through energy threshold is due to the higher geometrical acceptance of the veto with respect to the detector.

Figure A.6b shows a typical response of charged particles, for which the BC-501A works as a calorimeter until the impinging nuclei have enough energy to punch through the detector itself. Figure A.6d shows the amplitude-TOF spectrum of the BC-501A for anti-coincidence events, i.e. neutral particles. The response of the detector is noticeably different in this case and much more complicated to understand. The final interpretation of the results obtained with anti-coincidence events is currently ongoing. An in-depth understanding of the response to the neutron beam depends on the full characterization of n-γ discrimination capabilities and on a careful evaluation of the contribution coming from spurious coincidences.

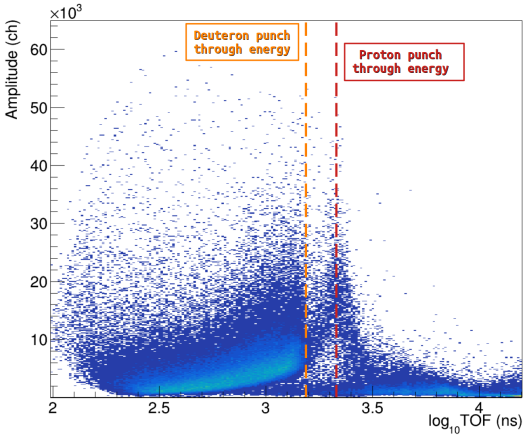

(a) VETO signals coincidence events

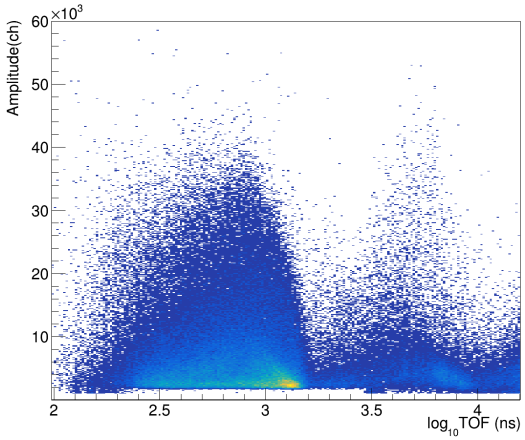

(b) BC-501A signals coincidence events

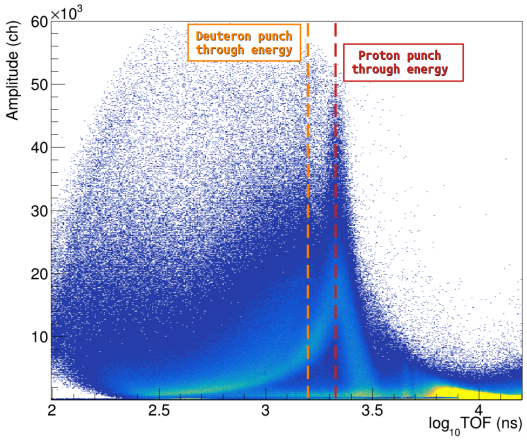

(c) VETO signals anti-coincidence events

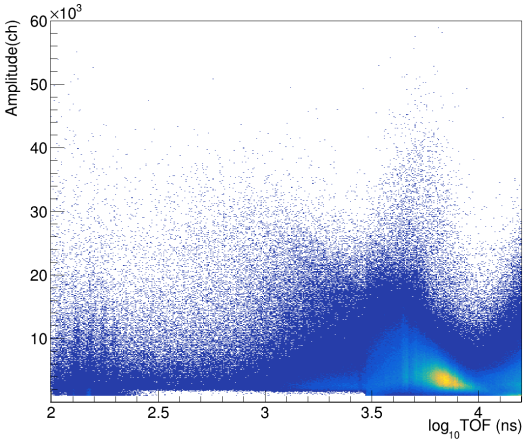

(d) BC501A signals anti-coincidence events

Figure A.6: Amplitude of the registered signals as a function of TOF for coincidence and anti-coincidence events for the BC501-A system. In (a) and (c) the punch-through energy for protons and deuterons in the VETO is highlighted.

Figure A.7 contains the same results addressed in Figure A.6 obtained for the VETO-phoswich BGO crystal combination. In this case, given the slightly lower time resolution of the phoswich system, the time coincidence window between veto and detector was fixed at ± 12 ns. The graphs shown in Figure A.7a and A.7c for the veto can be understood with the same considerations made for the other detection system. The main difference is the thickness of the plastic scintillator, which is much larger in this case. This increases the punch-through energy but yields a better energy resolution. As a matter of fact this veto detector, contrary to the one of the BC-501A system, is able to discriminate between

signals produced by different charged particles. In the case of Figure A.7a and A.7c, the two branches visible are generated by protons and deuterons created in beam-target interactions. As for the BC-501A system, the veto had a higher geometrical acceptance than the detector, which justifies the presence of anti-coincidence signals for charged particles above the punch-through energy.

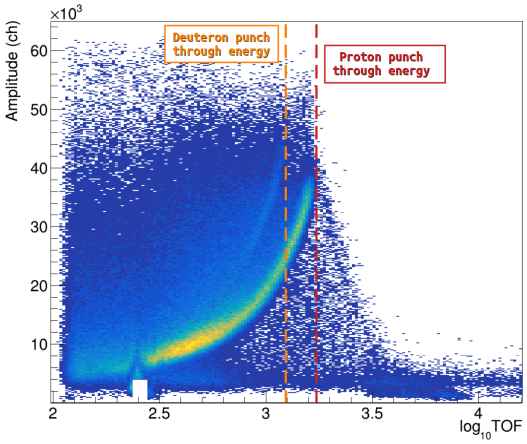

(a) VETO signals coincidence events

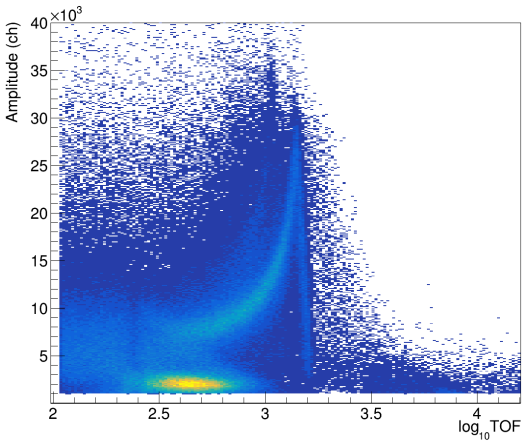

(b) BGO signals coincidence events

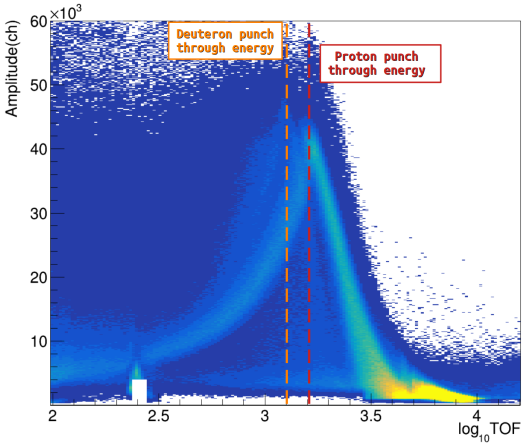

(c) VETO signals anti-coincidence events

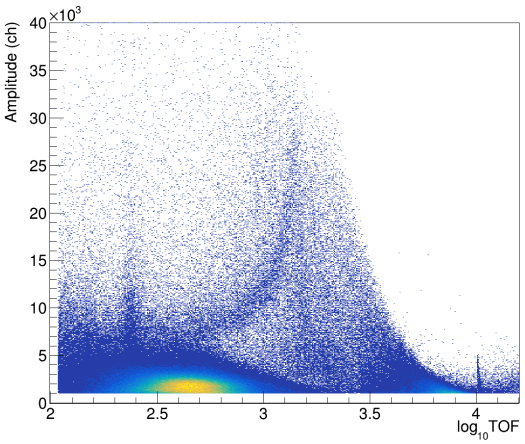

(d) BGO signals anti-coincidence events

Figure A.7: Amplitude of the registered signals as a function of TOF for coincidence and anti-coincidence events for the BGO phoswich system. In (a) and (c) the punch-through energy for protons and deuterons in the VETO is highlighted.

For the BGO detector, the request for coincidence signals yields the results shown in Figure A.7b. Here, the two branches visible in the veto are also distinguishable, meaning that the coincidence signals mostly come from the light generated in the plastic scintillator of the phoswich system. Thus, as expected, charged particle signals are dominated by the fast component of the BGO. At the contrary, the anti-coincidence signals (Figure A.7d) do not contain at all this component. Instead, the slower component coming from energy deposition in the BGO increases at higher energies of the impinging particle. From these plots, it can be stated that the phoswich system appears to work as intended.

To summarize, the preliminary results obtained thus far highlight that the first system has shown good particle discrimination capabilities, achieving an n-γ discrimination efficiency of about 90%. Moreover, the different light response of the BGO phoswich system shows that it can be effectively used to separate charged and neutral particles.

The results obtained with the neutron beam at the Neutron Escape Line of n_TOF experimental area 1 (EAR1) are currently being carefully studied. The coincidence analysis performed shows promising results for both detection systems, with the final evaluation of the neutron detection efficiency currently ongoing.

Bibliography and Sitography

[1] Glenn F. Knoll. *Radiation Detection and Measurement, 4^{th} ed.* John Wiley and Sons, Inc, 2010.

[2] Particle data group. *Passage of particles through matter*. 2021. URL: https://pdg.lbl.gov/2021/reviews/rpp2020-rev-passage-particles-matter.pdf.

[3] L. Landau. "On the energy loss of fast particles by ionization". In: *J. Phys.(USSR)* 8 (1944), pp. 201–205. DOI: 10.1016/B978-0-08-010586-4.50061-4.

[4] P. V. Vavilov. "Ionization losses of high-energy heavy particles". In: *Sov. Phys. JETP* 5 (1957), pp. 749–751.

[5] William R. Leo. *Techniques for Nuclear and Particle Physics Experiments, 2^{nd} ed.* Springer-Verlag Berlin Heidelberg, 1994.

[6] M. Durante and H. Paganetti. "Nuclear Physics in Particle Therapy: a review". In: *Reports on Progress in Physics* 79 (2016). Ed. by IOP Publishing. DOI: 10.1088/0034-4885/79/9/096702.

[7] Harald Paganetti. *Proton Therapy Physics*. Series in Medical Physics and Biomedical Engineering. CRC Press, 2011.

[8] H. A. Bethe. "Molière's Theory of Multiple Scattering". In: *Phys. Rev.* 89 (6 Mar. 1953), pp. 1256–1266. DOI: 10.1103/PhysRev.89.1256.

[9] Virgil L. Highland. "Some practical remarks on multiple scattering". In: *Nuclear Instruments and Methods* 129.2 (1975), pp. 497–499. ISSN: 0029-554X. DOI: 10.1016/0029-554X(75)90743-0.

[10] Dieter Schardt, Thilo Elsässer, and Daniela Schulz-Ertner. "Heavy-ion tumor therapy: Physical and radiobiological benefits". In: *Rev. Mod. Phys.* 82 (1 Feb. 2010), pp. 383–425. DOI: 10.1103/RevModPhys.82.383.

[11] A. C. Kraan. "Range Verification Methods in Particle Therapy: Underlying Physics and Monte Carlo Modeling". In: *Frontiers in Oncology* 150.5 (2015). DOI: 10.3389/fonc.2015.00150.

[12] R. Serber. "Nuclear Reactions at High Energies". In: *Phys. Rev.* 72 (11 Dec. 1947), pp. 1114–1115. DOI: 10.1103/PhysRev.72.1114.

[13] J. J. Griffin. "Statistical Model of Intermediate Structure". In: *Phys. Rev. Lett.* 17 (9 Aug. 1966), pp. 478–481. DOI: 10.1103/PhysRevLett.17.478.

[14] H. L. Bradt and B. Peters. "The Heavy Nuclei of the Primary Cosmic Radiation". In: *Phys. Rev.* 77 (1 Jan. 1950), pp. 54–70. DOI: 10.1103/PhysRev.77.54.

[15] R. J. Glauber. *Lecture on Theoretical Physics*. Interscience, 1959.

[16] S. Kox et al. "Trends of total reaction cross sections for heavy ion collisions in the intermediate energy range". In: *Phys. Rev. C* 35 (5 May 1987), pp. 1678–1691. DOI: 10.1103/PhysRevC.35.1678.

[17] M.Y.H. Farag. "Modified Glauber model for the total reaction cross-section of ^{12}C + ^{12}C collisions". In: *Eur. Phys. J. A* 12.4 (2001), pp. 405–411. DOI: 10.1007/s10050-001-8664-2.

[18] C.M. Werneth et al. "Validation of elastic cross section models for space radiation applications". In: *Nuclear Instruments and Methods in Physics Research Section B: Beam Interactions with Materials and Atoms* 392 (2017), pp. 74–93. ISSN: 0168-583X. DOI: 10.1016/j.nimb.2016.12.009.

[19] Alfredo Ferrari and Paola R. Sala. *The Physics of High Energy Reactions*. Geneva: CERN, 1997. URL: https://cds.cern.ch/record/682497.

[20] Badawy Abu-Ibrahim. "Nucleus-nucleus total reaction cross sections, and the nuclear interaction radius". In: *Phys. Rev. C* 83 (4 Apr. 2011), p. 044615. DOI: 10.1103/PhysRevC.83.044615.

[21] John W. Norbury et al. "Are Further Cross Section Measurements Necessary for Space Radiation Protection or Ion Therapy Applications? Helium Projectiles". In: *Frontiers in Physics* 8 (2020). ISSN: 2296-424X. DOI: 10.3389/fphy.2020.565954.

[22] L. Sihver et al. "A comparison of total reaction cross section models used in FLUKA, GEANT4 and PHITS". In: *2012 IEEE Aerospace Conference* (2012), pp. 1–10. DOI: 10.1109/AERO.2012.6187014.

[23] F Luoni et al. "Total nuclear reaction cross-section database for radiation protection in space and heavy-ion therapy applications". In: *New Journal of Physics* 23.10 (Oct. 2021), p. 101201. DOI: 10.1088/1367-2630/ac27e1.

[24] C. Divay et al. "Differential cross section measurements for hadron therapy: 50 MeV/nucleon ^{12}C reactions on H, C, O, Al, and ^{nat}Ti targets". In: *Phys. Rev. C* 95 (4 Apr. 2017), p. 044602. DOI: 10.1103/PhysRevC.95.044602.

[25] J. Dudouet, D. Juliani, et al. "Double-differential fragmentation cross-section measurements of 95 MeV/nucleon ^{12}C beams on thin targets for hadron therapy". In: *Phys. Rev. C* 88 (2 Aug. 2013). DOI: 10.1103/PhysRevC.88.024606.

[26] John W. Norbury et al. "Nuclear data for space radiation". In: *Radiation Measurements* 47.5 (2012), pp. 315–363. ISSN: 1350-4487. DOI: 10.1016/j.radmeas.2012.03.004.

[27] World Cancer Research Fund (WCRF). *Worldwide Cancer Data*. URL: https://www.wcrf.org/cancer-trends/worldwide-cancer-data/.

[28] Particle Therapy Co-Operative Group (PTCOG). *Patient Statistics per End of 2021*. 2022. URL: https://ptcog.site/.

[29] G. Battistoni, I. Mattei, and S. Muraro. "Nuclear physics and particle therapy". In: *Advances in Physics: X* 1.4 (2016), pp. 661–686. DOI: 10.1080/23746149.2016.1237310.

[30] Jennifer S. Chiang et al. "Proton beam radiotherapy for patients with early-stage and advanced lung cancer: a narrative review with contemporary clinical recommendations". In: *Journal of Thoracic Disease* 13.2 (2021). ISSN: 2077-6624. DOI: 10.21037/jtd-20-2501.

[31] R. F. Laitano. *Fondamenti di dosimetria delle radiazioni ionizzanti, 4ª ed.* ENEA, 2015. URL: https://www.enea.it/it/seguici/pubblicazioni/pdf-volumi/FondamentidosimetriaradiazioniionizzantiIV.pdf.

[32] GSI. *Particle Irradiation Data Ensemble (PIDE).* URL: https://www.gsi.de/bio-pide.

[33] Marco Durante et al. "Applied nuclear physics at the new high-energy particle accelerator facilities". In: *Physics Reports* 800 (2019), pp. 1–37. ISSN: 0370-1573. DOI: 10.1016/j.physrep.2019.01.004.

[34] Kenta Takada et al. "Evaluation of RBE-weighted doses for various radiotherapy beams based on a microdosimetric function implemented in PHITS". In: *Journal of Physics: Conference Series* 1662.1 (Oct. 2020), p. 012004. DOI: 10.1088/1742-6596/1662/1/012004.

[35] E Haettner et al. "Experimental study of nuclear fragmentation of 200 and 400 MeV/u ^{12}C ions in water for applications in particle therapy". In: *Physics in Medicine & Biology* 58.23 (Nov. 2013), p. 8265. DOI: 10.1088/0031-9155/58/23/8265.

[36] M. C. Frese et al. "Application of Constant vs. Variable Relative Biological Effectiveness in Treatment Planning of Intensity-Modulated Proton Therapy". In: *International Journal of Radiation Oncology, Biology, Physics* 79.1 (2011), pp. 80–88. ISSN: 0360-3016. DOI: 10.1016/j.ijrobp.2009.10.022.

[37] F. Tommasino and M. Durante. "Proton Radiobiology". In: *Cancers* 7 (2015), pp. 353–381. ISSN: 2072-6694. DOI: 10.1016/j.nima.2010.03.045.

[38] J. S. Loeffler and M. Durante. "Charged particle therapy–optimization, challenges and future directions". In: *Nat Rev Clin Oncol* 10 (7 May 2013), pp. 411–424. DOI: 10.1038/nrclinonc.2013.79.

[39] T Pfuhl et al. "Dose build-up effects induced by delta electrons and target fragments in proton Bragg curves—measurements and simulations". In: *Physics in Medicine & Biology* 63.17 (Aug. 2018). DOI: 10.1088/1361-6560/aad8fc.

[40] C K Ying et al. "Contributions of secondary fragmentation by carbon ion beams in water phantom: Monte Carlo simulation". In: *Journal of Physics: Conference Series* 851 (May 2017). DOI: 10.1088/1742-6596/851/1/012033.

[41] Brookhaven National Laboratory. *Bragg Curves and Peaks.* URL: https://www.bnl.gov/nsrl/userguide/bragg-curves-and-peaks.php.

[42] Francis A. Cucinotta, Myung-Hee Y. Kim, and Lei Ren. "Evaluating shielding effectiveness for reducing space radiation cancer risks". In: *Radiation Measurements* 41.9 (2006). Space Radiation Transport, Shielding, and Risk Assessment Models, pp. 1173–1185. ISSN: 1350-4487. DOI: 10.1016/j.radmeas.2006.03.011.

[43] Marco Durante and Francis A. Cucinotta. "Heavy ion carcinogenesis and human space exploration". In: *Nature Reviews Cancer* 8 (6 2008), pp. 465–472. DOI: 10.1038/nrc2391.

[44] Marco Durante and Francis A. Cucinotta. "Physical basis of radiation protection in space travel". In: *Rev. Mod. Phys.* 83 (4 Nov. 2011), pp. 1245–1281. DOI: 10.1103/RevModPhys.83.1245.

[45] G.D. Badhwar and P.M. O'Neill. "An improved model of galactic cosmic radiation for space exploration missions". In: *International Journal of Radiation Applications and Instrumentation. Part D. Nuclear Tracks and Radiation Measurements* 20.3 (1992). Special Section Galactic Cosmic Radiation: Constraints on Space Exploration, pp. 403–410. ISSN: 1359-0189. DOI: 10.1016/1359-0189(92)90024-P.

[46] M. Durante and C. Bruno. "Impact of rocket propulsion technology on the radiation risk in missions to Mars". In: *The European Physical Journal D* 60 (1 2010), pp. 215–218. DOI: 10.1140/epjd/e2010-00035-6.

[47] C. Zeitlin et al. "Shielding and fragmentation studies". In: *Radiation Protection Dosimetry* 116.1-4 (Dec. 2005), pp. 123–124. ISSN: 0144-8420. DOI: 10.1093/rpd/nci064.

[48] M. Pugliese et al. "SPADA: A project to study the effectiveness of shielding materials in space". In: *Il Nuovo Cimento C* (2008), pp. 91–97. DOI: 10.1393/ncc/i2008-10283-7.

[49] Francis A Cucinotta and Marco Durante. "Cancer risk from exposure to galactic cosmic rays: implications for space exploration by human beings". In: *The Lancet Oncology* 7.5 (2006), pp. 431–435. ISSN: 1470-2045. DOI: 10.1016/S1470-2045(06)70695-7.

[50] Giuseppe Battistoni, Marco Toppi, et al. "Measuring the Impact of Nuclear Interaction in Particle Therapy and in Radio Protection in Space: the FOOT Experiment". In: *Frontiers in Physics* 8 (2021). ISSN: 2296-424X. DOI: 10.3389/fphy.2020.568242. URL: https://www.frontiersin.org/articles/10.3389/fphy.2020.568242.

[51] T. T. Böhlen et al. "The FLUKA Code: Developments and Challenges for High Energy and Medical Applications". In: *Nuclear Data Sheets* 120 (2014), pp. 211–214. ISSN: 0090-3752. DOI: 10.1016/j.nds.2014.07.049.

[52] G. Battistoni et al. "The FLUKA Code: an Accurate Simulation Tool for Particle Therapy". In: *Frontiers in Oncology* 6.116 (2016).

[53] FOOT collaboration. *FOOT Conceptual Design Report*. 2017.

[54] W. S. Cho et al. "OPTIMASS: a package for the minimization of kinematic mass functions with constraints". In: *Journal of High Energy Physics* 26 (2016). DOI: 10.1007/JHEP01(2016)026.

[55] Hamamatsu. *MPPC S13360 series datasheet*. 2016. URL: https://www.hamamatsu.com/resources/pdf/ssd/s13360_series_kapd1052e.pdf.

[56] A.C. Kraan, R. Zarrella, et al. "Charge identification of nuclear fragments with the FOOT Time-Of-Flight system". In: *Nuclear Instruments and Methods in Physics Research Section A* 1001 (2021), p. 165206. ISSN: 0168-9002. DOI: 10.1016/j.nima.2021.165206.

[57] Ziad A. H. et al. "Performance of upstream interaction region detectors for the FIRST experiment at GSI". In: *Journal of Instrumentation* 7 (Feb. 2012). DOI: 10.1088/1748-0221/7/02/P02006.

[58] R. Pleskac et al. "The FIRST experiment at GSI". In: *Nuclear Instruments and Methods in Physics Research Section A* 678 (2012), pp. 130–138. ISSN: 0168-9002. DOI: 10.1016/j.nima.2012.02.020.

[59] F. Tommasino et al. "Proton beam characterization in the experimental room of the Trento Proton Therapy facility". In: *Nuclear Instruments and Methods in Physics Research Section A: Accelerators, Spectrometers, Detectors and Associated Equipment* 869 (2017), pp. 15–20. ISSN: 0168-9002. DOI: 10.1016/j.nima.2017.06.017.

[60] Dong Y. et al. "The Drift Chamber detector of the FOOT experiment: Performance analysis and external calibration". In: *Nuclear Instruments and Methods in Physics Research Section A* 986 (2021), p. 164756. ISSN: 0168-9002. DOI: 10.1016/j.nima.2020.164756.

[61] PICSEL (Physics with Integrated Cmos Sensors and ELectron machines) group. IPHC. 2019. URL: http://www.iphc.cnrs.fr/-PICSEL-.html.

[62] C.-A. Reidel et al. "Alignment procedure of silicon pixel detectors for ion-beam therapy applications". In: *Nuclear Instruments and Methods in Physics Research Section A: Accelerators, Spectrometers, Detectors and Associated Equipment* 931 (2019), pp. 142–150. ISSN: 0168-9002. DOI: 10.1016/j.nima.2019.03.042.

[63] I Valin et al. "A reticle size CMOS pixel sensor dedicated to the STAR HFT". In: *Journal of Instrumentation* 7.01 (Jan. 2012), p. C01102. DOI: 10.1088/1748-0221/7/01/C01102.

[64] PLUME (Pixel Ladders with Ultra-low Material Embedding) project website. IPHC. 2017. URL: http://www.iphc.cnrs.fr/PLUME.html.

[65] C.-A. Reidel et al. "Response of the Mimosa-28 pixel sensor to a wide range of ion species and energies". In: *Nuclear Instruments and Methods in Physics Research Section A: Accelerators, Spectrometers, Detectors and Associated Equipment* 1017 (2021), p. 165807. ISSN: 0168-9002. DOI: 10.1016/j.nima.2021.165807.

[66] G. Silvestre et al. "Characterization of 150 μm thick silicon microstrip prototype for the FOOT experiment". In: *Journal of Instrumentation* 17.12 (Dec. 2022), P12012. DOI: 10.1088/1748-0221/17/12/P12012.

[67] G. Silvestre. "Characterization of the Microstrip Silicon Detector for the FragmentatiOn Of Target experiment". In: *Nuclear Instruments and Methods in Physics Research Section A* 1047 (2023), p. 167717. ISSN: 0168-9002. DOI: 10.1016/j.nima.2022.167717.

[68] A.C. Kraan et al. "Calibration and performance assessment of the TOF-Wall detector of the FOOT experiment". In: *Nuclear Instruments and Methods in Physics Research Section A* 1045 (2023), p. 167615. ISSN: 0168-9002. DOI: 10.1016/j.nima.2022.167615.

[69] M. Morrocchi et al. "Development and characterization of a ΔE-TOF detector prototype for the FOOT experiment". In: *Nuclear Instruments & Methods in Physics Research* 916 (2019). Ed. by ELSEVIER, pp. 116–124. DOI: 10.1016/j.nima.2018.09.086.

[70] Lorenzo Scavarda. "Design and development of the Calorimeter for the FOOT experiment". PhD thesis. Università degli Studi di Torino, 2022.

[71] P. Jenni et al. *ATLAS high-level trigger, data-acquisition and controls : Technical Design Report*. Geneva: CERN, 2003. URL: https://cds.cern.ch/record/616089?ln=it.

[72] L. Galli et al. "WaveDAQ: An highly integrated trigger and data acquisition system". In: *Nuclear Instruments and Methods in Physics Research Section A* 936 (2019). Frontier Detectors for Frontier Physics: 14th Pisa Meeting on Advanced Detectors, pp. 399–400. ISSN: 0168-9002. DOI: 10.1016/j.nima.2018.07.067.

[73] Riccardo Ridolfi. "The FOOT experiment: Trigger and Data Acquisition (TDAQ) development and data analysis". PhD thesis. Università degli Studi di Bologna, 2022.

[74] L. Galli et al. "The fragmentation trigger of the FOOT experiment". In: *Nuclear Instruments and Methods in Physics Research Section A* 1046 (2023), p. 167757. ISSN: 0168-9002. DOI: 10.1016/j.nima.2022.167757.

[75] Alexandrov Andrey et al. "The Continuous Motion Technique for a New Generation of Scanning Systems". In: *Scientific Reports* 7 (1 2017). DOI: 10.1038/s41598-017-07869-3.

[76] Giuliana Galati et al. "Charge identification of fragments with the emulsion spectrometer of the FOOT experiment". In: *Open Physics* 19.1 (2021), pp. 383–394. DOI: 10.1515/phys-2021-0032. URL: https://doi.org/10.1515/phys-2021-0032.

[77] I. T. Jolliffe. *Principal Component Analysis*. Ed. by M. Lovric. Springer Series in Statistics. Springer Berlin Heidelberg, 2011. DOI: 10.1007/978-3-642-04898-2_455.

[78] FLUKA Team. *FLUKA website*. 2010. URL: http://www.fluka.org/fluka.php.

[79] The Geant4 Collaboration. *Geant4 website*. URL: https://www.geant4.org.

[80] *CNAF*. INFN. URL: https://www.cnaf.infn.it/.

[81] P. Žugec et al. "Pulse processing routines for neutron time-of-flight data". In: *Nuclear Instruments and Methods in Physics Research Section A* 812 (2016), pp. 134–144. ISSN: 0168-9002. DOI: 10.1016/j.nima.2015.12.054.

[82] P.S. Marrocchesi et al. "Beam test performance of a scintillator-based detector for the charge identification of relativistic ions". In: *Nuclear Instruments and Methods in Physics Research Section A* 659.1 (2011), pp. 477–483. DOI: 10.1016/j.nima.2011.08.034.

[83] Alexandre Sécher. "Algorithms and software tools for the reconstruction of nuclear data in hadrontherapy". PhD thesis. Université de Strasbourg, 2022.

[84] Johannes Rauch and Tobias Schlüter. "GENFIT - a Generic Track-Fitting Toolkit". In: *Journal of Physics: Conference Series* 608.1 (Apr. 2015), p. 012042. DOI: 10.1088/1742-6596/608/1/012042.

[85] Höppner C. *GENFIT - a Generic Track Reconstruction Toolkit*. URL: https://genfit.sourceforge.net/GENFIT_v1_2.pdf.

[86] Lars Bugge and Jan Myrheim. "Tracking and track fitting". In: *Nuclear Instruments and Methods* 179.2 (1981), pp. 365–381. ISSN: 0029-554X. DOI: 10.1016/0029-554X(81)90063-X.

[87] E. Lund et al. "Track parameter propagation through the application of a new adaptive Runge-Kutta-Nyström method in the ATLAS experiment". In: *Journal of Instrumentation* 4.04 (Apr. 2009), P04001. DOI: 10.1088/1748-0221/4/04/P04001.

[88] Tadeas Bilka et al. *Implementation of GENFIT2 as an experiment independent track-fitting framework*. 2019. DOI: h10.48550/arXiv.1902.04405. arXiv: 1902.04405 [physics.data-an].

[89] R. E. Kalman. "A New Approach to Linear Filtering and Prediction Problems". In: *Journal of Basic Engineering* 82.1 (Mar. 1960), pp. 35–45. ISSN: 0021-9223. DOI: 10.1115/1.3662552.

[90] C. Höppner et al. "A novel generic framework for track fitting in complex detector systems". In: *Nuclear Instruments and Methods in Physics Research Section A: Accelerators, Spectrometers, Detectors and Associated Equipment* 620.2 (2010), pp. 518–525. ISSN: 0168-9002. DOI: 10.1016/j.nima.2010.03.136.

[91] Keisuke Fujii. "Extended Kalman Filter". In: (Aug. 2023).

[92] Uwe Schneider and Roger Antoine Hälg. "The Impact of Neutrons in Clinical Proton Therapy". In: *Frontiers in Oncology* 5 (2015). DOI: 10.3389/fonc.2015.00235.

[93] D. H. Wilkinson. "The Phoswich - A Multiple Phosphor". In: *Review of Scientific Instruments* 23.8 (Aug. 1952), pp. 414–417. DOI: 10.1063/1.1746324.

[94] Scavarda L. "Design and performance of the Calorimeter for the FOOT experiment". In: *Il Nuovo Cimento C* 43.123 (2020). DOI: 10.1393/ncc/i2020-20123-3.

[95] n_TOF Collaboration. "The neutron Time-Of-Flight facility, n_TOF, at CERN (I): Technical Description". In: (2013). URL: http://cds.cern.ch/record/1514680.

[96] C. Guerrero, A. Tsinganis, E. Berthoumieux, et al. "Performance of the neutron time-of-flight facility n_TOF at CERN". In: *European Physics Journal A* 49.27 (2013). DOI: 10.1140/epja/i2013-13027-6.

[97] A.D. Carlson et al. "International Evaluation of Neutron Cross Section Standards". In: *Nuclear Data Sheets* 110.12 (2009). Special Issue on Nuclear Reaction Data, pp. 3215–3324. ISSN: 0090-3752. DOI: 10.1016/j.nds.2009.11.001.